COMPREHENSIVE STUDY OF COMPOSITION GRADIENT STRONTIUM DOPED LANTHANUM MANGANITE THIN FILMS DEPOSITED BY MAGNETRON CO-SPUTTERING

by

YISHU WANG

Presented to the Faculty of the Graduate School of

The University of Texas at Arlington in Partial Fulfillment

of the Requirements

for the Degree of

DOCTOR OF PHILOSOPHY

THE UNIVERSITY OF TEXAS AT ARLINGTON

August 2015

Acknowledgements

I would like to graciously thank Dr. Efstathios I. Meletis for advising this work during last five years. The presented results would not be finished without his patient guidance and generous support. I would also like to thank all my committee members, Dr. Hao, Dr. Liu, Dr. Tibbals and Dr. Yang for providing additional guidance and taking the time to involve themselves in my work. The special thanks would go to Dr. Jiang for assistance and training with several instruments in CCMB.

I would like to thank all my lab mates for their advice, assistance and training during my graduate study, .especially, Dr. Jie He and Minghui Zhang for assistance with TEM analysis in this work; Dr. Adam Smith for AFM training; Mr. Elad Har-Even for discussion and assistance on my work.

I am also grateful to MSE staff, Mrs. Jennifer Standlee, Mrs. Beth Robinson and Mr David Yan, who have been always more than helpful in many aspects for completing my Ph.D. program.

Finally and most importantly, I would like to thanks my parents for always bringing me confidence. All my accomplishment belongs to you. Also, the special thanks belong to my lovely girlfriend Miao Wang, who has always supported me and brought me strength. This work was supported by the National Science Foundation under Award NSF-NIRT-0709293

July 21, 2015

Abstract

COMPREHENSIVE STUDY OF COMPOSITION GRADIENT MICROSTRUCTURE OF STRONTIUM DOPED LANTHANUM MANGANITE THIN FILMS DEPOSITED BY MAGNETRON CO-SPUTTERING

Yishu Wang, PhD

The University of Texas at Arlington 2015

Supervising Professor: Efstathios I. Meletis

In this body of work, the examination of three different types of Strontium doped lanthanum manganite thin films synthesized by magnetron sputtering in the Surface and Nano Engineering Laboratory (SaNEL) allowed for the development of a detailed understanding between the processing conditions, the nano-scale structure and strain relaxation of the as-deposited thin films. Pure Lanthanum manganite and strontium doped lanthanum manganite thin films which were epitaxially grown on (001) single crystalline lanthanum alumina (LAO) and magnesium oxide (MgO) were fabricated by using single target deposition. The optimum deposition conditions were explored as preparation for synthesis epitaxial composition gradient strontium doped lanthanum manganite thin films by using co-sputtering deposition later. Surface morphology and microstructure of as-deposit thin films were characterized by atomic force microscopy (AFM), x-ray diffraction (XRD) and high resolution transmission electronic microscopy

(HRTEM). Pseudo-cubic structure was identified in epitaxial lanthanum manganite thin film on LAO and strontium doped lanthanum manganite on MgO substrate, while orthorhombic structure was obtained in epitaxial strontium lanthanum manganite on LAO and lanthanum manganite on MgO substrate. Deposition rates of each target on different substrate were calculated.

Epitaxial compositional graded (ECG) strontium doped lanthanum manganite thin films were prepared on the same substrates by using co-sputtering deposition with both targets deposited simultaneously. The as-deposit thin films using novel deposition procedure with different conditions were compared. The substrate temperature and power rate of each target are considered as the key factor for controlling the quality of the films. The surface morphology, microstructure and composition ratio of each element were characterized by AFM, XRD, HRTEM and XPS. A novel low angle XRD method was involved to examine the graded structure with the nano-scaled variation. It is found that polycrystalline structure with pseudo-cubic columnar domains was formed in the film on MgO substrate while epitaxial pseudo-cubic structure was obtained in the film on LAO substrate. The composition gradient of Sr doping was confirmed by Energy dispersive X-ray spectroscopy analysis along growth direction. The boundaries between each column were considered as a strain relaxation source in polycrystalline thin film. The ECG thin film, which is under the critical thickness, exhibits a novel strain relaxation which is

considered as composition grade structure effect. Thus, the ECG buffer layer was confirmed as an effective method in strain controlling.

To further complex the structure and develop for application, a triple-layer strontium doped lanthanum manganite thin films on LAO and MgO substrates were deposited by using co-sputtering deposition with lanthanum manganite (LMO) target and strontium manganite (SMO) target. The films were designed to have a LMO layer at bottom and SMO layer on surface with both La and Sr gradient layer in between. The microstructure of as-deposit films were identified as epitaxial structure. Two epitaxial layers were found in the film on LAO substrate where orthorhombic structure was obtained below about 20 nm and pseudo-cubic structure was formed on the top. Similar strain relaxation was also observed in the film. This may produce “new” materials with the properties that are not available in the individual component phases, which might also open up various new possibilities of designing new nanoscale structures with unusual cross coupled properties.

Table of Contents

List of Illustrations

List of Tables

Chapter 1

Introduction

1.1 Introduction and Motivation

Materials science and engineering have been considered as the frontier of technological advancement ever since the bronze and iron ages. Nowadays, the information age depends on the development of “smarter” and “smaller” magnetic materials for memory, data storage, processing and probing. One of the most attractive magnetic materials is the transition metal oxides (TMO_s)[1] with perovskite structure (ABO_3 type), which plays a vitally important rule not only in fundamental physics but also in industry, such as the ferroelectricity of titanates (doped $BaTiO_3$)[1, 2], high temperature superconductivity of cuprates ($La_{2-x}Ba_xCuO_4$)[3-5], colossal magnetoresistance (CMR) of manganites (doped $LaMnO_3$), unconventional p-wave superconductivity of ruthenates (Sr_2RuO_4)[6] and multiferroicity[7, 8].

Among these materials, the doped manganese oxides $R_{1-x}A_xMnO_3$, where R is trivalent rare earth ion and A is divalent alkali earth ion, have been attracted a lot of attention and study due to its potential application in magnetic device. The research and development for magnetic recording efforts is focusing on achieving higher areal density (the number of bits/units area on a disk surface) in order to have large capacity of hard drive. This can be realized by increasing the linear as well as track densities. However, the most challenging issue towards achieving high recording density media is to produce

magnetic thin films which have a large signal-to-noise ratio despite the smaller size of the bit or data being detected. Here comes a very sensitive magnetoresistive (MR) material called colossal magnetoresistance material which exhibits a resistance change when subjected to a magnetic field and may eventually evolve into magnetoresisitive heads to achieve the required areal densities.

To exploit such a magnetic device, epitaxial heterostructures are required for the thin films in order to enhance its electric and magnetic transportation properties. Thus, it is significant to clarify the effects induced by the substrates in the magnetic film. One of the most important issues both for physics and possible application is the strain dependence of material property especially in epitaxial thin films because of lattice mismatch with the substrate. The main problems concerning applications form three groups:

(1) Growing pseudomorphic epilayers and multilayer heterostructures without misfit dislocations. The stresses in such heterostructures modify the band structure of the semiconductor, which leads to new electrical and optical properties.

(2) The opposite problem, i.e., the growing of totally relaxed layers, known as artificial substrates, which is necessary in building various heterostructure devices based on materials whose lattice parameters differ from those of commercially available substrates.

(3) An extreme manifestation of the relaxation of strained layers is the formation of nanometer-scale islands, a problem that has lately gained great popularity (purely

scientific and also from the viewpoint of applications) in connection with the possibility of growing nanoisland ensembles with a density higher than 10^{10} cm^2 (ensembles of quantum dots).

Functionally graded materials (FGMs), with a continuous distribution or function which is originally used for elimination of thermal stress[9, 10], have widely expanded its application in designing electronic, biological and optical devices due to their unique properties such as insulators in thin film transistors[11], thermoelectric conversion[12], optical spacers or electron/hole blocking/transporting layer in photovoltaic systems[13, 14], biomaterial manufacturing[15], and aerospace technologies[16]. Out-of-plane composition gradient as well as coherent epitaxy films namely epitaxial compositional graded (ECG) films as a category of FGMs, have been studied recently, since physical properties of epitaxial thin films can be significantly modified by a lattice strain[17]. The previous research on strain-induced modification of the physical properties of thin films include enhancement of the electrons mobility in relaxed Si-Ge films[18], increment of superconducting critical temperature in $La_{1.85}Sr_{0.15}CuO_4$ on $LaSrAlO_4$ substrates[19], phase transformation temperature from ferromagnetic metal $La_{1-x}Sr_xMnO_3$ $(0.3 \leq x \leq 0.5)$ into an antiferromagnetic insulator[20]. Thus, it is expected that this ECG structure could induce new properties by modified the intrinsic strain.

1.2 Research Objectives

Among these research fields, strain effects on transition temperature of $La_{1-x}Sr_xMnO_3$ have attracted significant attention, since it is found that the epitaxial strain of $La_{1-x}Sr_xMnO_3$ would highly depress T_C compared to its bulk counterpart[21-23]. Ahn and Millis et al. concluded that a biaxial strain could strengthen the Jahn-Teller distortion, further increase the splitting of the eg electron band and thereby reinforce the tendency of the electrons to become localized[24]. Based on this model, the dependence of T_C on the biaxial strain can be expressed as

$$T_C(\varepsilon) = T_C(\varepsilon = 0)\left(1 - \alpha\varepsilon_B - \frac{1}{2}\beta\varepsilon_{bi}^2\right) \quad \text{Eq.1.1}$$

where ε_B is the bulk strain, ε_{bi} is the biaxial strain, $\alpha = (1/T_C)dT_o/d\varepsilon_B$ is related to the unit volume cell variations under strain and β accounts for the Jahn-Teller energy splitting. According to Eq. 1.1, as soon as the biaxial strain exists, it always leads to a reduction in T_C. Thus, a process to relax the strain in doped manganite thin films would be the key to increasing of T_C and ECG thin film is expected as a promising candidate in strain modification. This may produce “new” materials with the properties that are not available in the individual component phases, which might also open up various new possibilities of designing new nanoscale structures with unusual cross coupled properties[25-28]. However, the main challenges of ECG thin films are mainly concerning on massive production and characterization in nanoscale.

The overall objective of the present research is to achieve an optimum deposition parameter of ECG thin film, develop a fundamental understanding of the growth and strain relaxation mechanism. The current research work has focused on the following specific objectives:

1) To gain fundamental knowledge of Sr doped composition gradient, epitaxial LSMO thin films in terms of composition, morphology and microstructure.

2) To study the composition gradient effect on strain relaxation by investigating the epitaxial LSMO thin film with multiple different d spacing layers.

3) To explore the possible unique cross coupled properties which are not available in the individual component phase by the designing structure.

1.3 Dissertation Overview

This dissertation consists of seven chapters. The following is an outline and brief summary of each chapter included in this document.

Chapter 1, Introduction: This chapter introduces the motivation and objectives of this research work; as well as providing a brief introduction to the current knowledge in the state of functional graded materials.

Chapter 2, Literature review: This chapter gives the detailed information on perovskite-type structure materials. Moreover, the strain effect on the properties of perovskite materials is reviewed.

Chapter 3, Thin Films Synthesis and Characterization: The chapter describes the deposition process of PVD magnetron sputtering. In addition, details are provided regarding the characterization methods and processes used including X-Ray diffraction (XRD), atomic force microscopy (AFM), X-ray photoelectron spectroscopy (XPS) and High-resolution transmission electronic microscopy (HRTEM).

Chapter 4, Microstructure of epitaxial $LaMnO_3$ and $La_{0.67}Sr_{0.33}MnO_3$ thin films on $LaAlO_3$ and MgO substrates by regular RF sputtering: This chapter focuses on fabrication and characterization of pure epitaxial $LaMnO_3$ and $La_{0.67}Sr_{0.33}MnO_3$ thin films which is the preparation for fabrication of co-sputtered thin films.

Chapter 5, Microstructure of RF co-sputtered strontium doped lanthanum manganite thin films by using $LaMnO_3$ and $La_{0.67}Sr_{0.33}MnO_3$ targets: This chapter describes the deposition process of co-sputtered $La_{1-x}Sr_xMnO_3$ thin films. The microstructure of as-deposit thin films and strain relaxation mechanism due to the epitaxial composition graded structure are discussed.

Chapter 6, Microstructure of RF co-sputtered strontium doped lanthanum manganite thin films by using $LaMnO_3$ and $SrMnO_3$ targets: This chapter describes another type of epitaxial compositional graded co-sputtered $La_{1-x}Sr_xMnO_3$ thin films with different targets to further understand the growth and microstructure of co-sputtered thin films.

Chapter 7, Conclusion: Finding throughout the study regarding microstructures of different types of co-sputtered $La_{1-x}Sr_xMnO_3$ thin films and strain relaxation mechanism are summarized in this chapter.

Chapter 2

Literature Review

2.1 Perovskite-type Oxide Structures

"Perovskite", initially earned its name from the mineral perovskite $CaTiO_3$ shown in Figure 2.1, was generally described as the representation of the inorganic materials with the crystal structure of ABX_3, where X is often oxygen or even fluorine and chlorine sometimes. The ABX_3 perovskite structure stands out by a wide margin compared with other structures, since it can produce an incredibly wide array of phases with totally different functions.

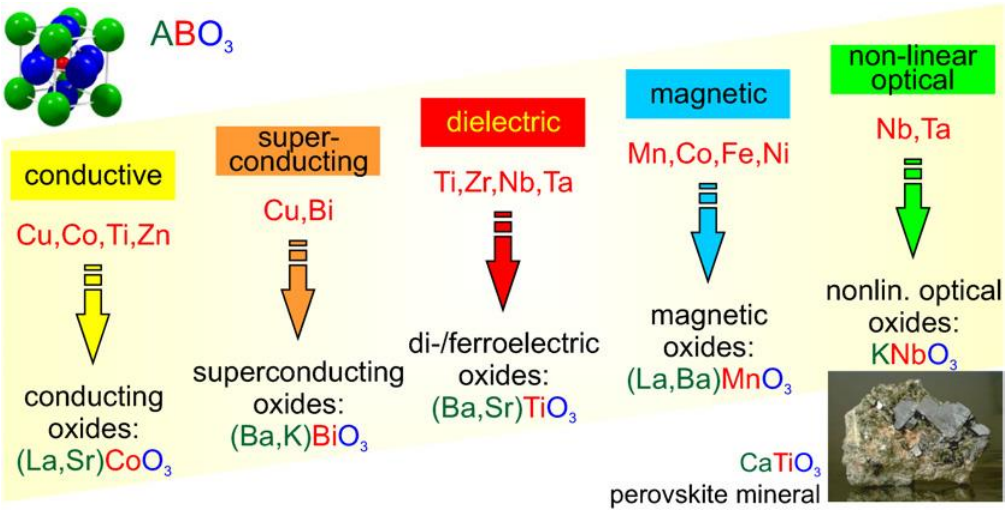

Figure 2.1 Functional perovskite oxides depending on the combination of A and B ions in the cubic structure of ABO_3, different physical properties and ground states are realized[29]

With the chemical formula of ABO_3, the perovskite group of oxides has drawn considerable attention in the last decades. It can be visualized as a simple cubic unit cell with the A site ion, such as La, occupying the vertices of the unit cell, the B site ions, such as Mn, located at the body center and oxygen atoms in the six face centers of the cube, as shown in Figure 2.2(a). Another way of presenting the perovskite structure can be described as a *Pm3m* symmetry with corner sharing BO_6 octahedral with the A cation occupying the 12-fold coordination sit formed in the middle of the cube of eight such octahedral shown in Figure 2.2(b)[30].

The first study on perovskites was conducted by Goldschmidt et al in the 1920s forming the basis for further exploration[31]. In the cubic ABO_3 perovskite structure, the A atoms are in Wyckoff position 1b, ½,½,½, the B atoms in 1a, 0,0,0; and the X atoms in 3d ½,0,0; 0,½,0; 0,0,½, all special positions. Although all the perovskite materials are considered with this structure, few of them have precisely cubic structure because the atoms are displaced from their ideal positions. The distorted BO_6 octahedral would induce possible transitions which may transfer to tetragonal, rhombohedral or orthorhombic structures.

Three main factors are considered as the reasons for the distortion in perovskite structure: size effects of atoms, deviations from ideal composition and the Jahn-Teller effect[32]. It is difficult to identify the specific effect from a distortion of a certain perovskite oxide since multiple factors usually act simultaneously.

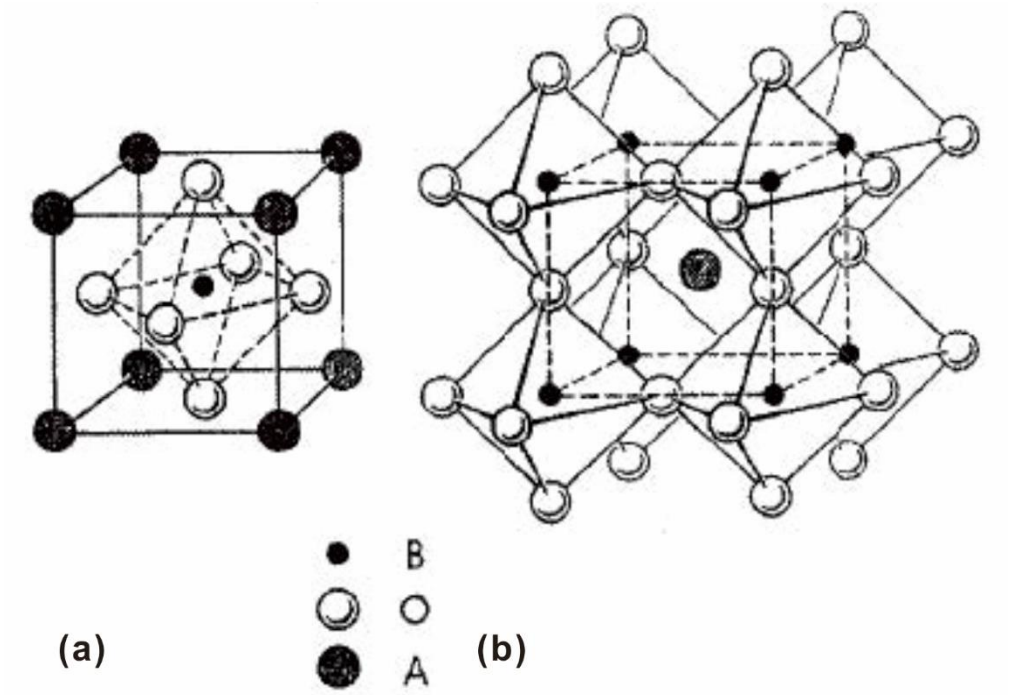

Figure 2.2 ABO_3 perovskite crystal structures[30]

(1) Size Effects

Considering the perovskite structure as a cubic close-packed array shown in figure 2.2, the ideal cation radii r_A and r_B can be deduced, where r_A must be the same as that of oxygen r_O while r_B is $(\sqrt{2}-1)r_O$. The ratio of r_A and r_B is used to estimate the degree of distortion in perovskite structure and named as the Goldschmidt's tolerance factor *t*, which is expressed as

$$t = \frac{d_{A-O}}{\sqrt{2}d_{B-O}} = \frac{r_A + r_O}{\sqrt{2}(r_B + r_O)} \qquad \text{Eq.2.1}$$

where d_{A-O} is the distance between the A site and the nearest oxygen ions, i.e. $r_A + r_O$, and d_{B-O} is the B-O shortest distance. The perovskite structure is stable for $0.89 < t < 1.02$, $t = 1$ corresponding to the perfect cubic closely packed

structure[33, 34]. One ideal example of perfect cubic perovskite structure is $SrTiO_3$, where $r_A = 1.44$ Å, $r_B = 0.605$ Å and $r_O = 1.40$ Å. The A-O bond has a larger thermal expansion coefficient and is normally more compressible than the B-O bond, thus the tolerance factor is dependent on both temperature and pressure[35].

Sometimes the A site ions are too smaller to fill the space in the cubic centers and the oxygen ions tend to move toward the center, which makes the Goldschmidt's tolerance factor *t* is smaller than one. As the tolerance factor decreased, the B-O-B angle becomes smaller than 180° and the BO_6 octahedra tilt cooperatively which causes an enlarged orthorhombic unit cell[36], such as orthorhombic $GdFeO_3$ with *t*= 0.81[37].

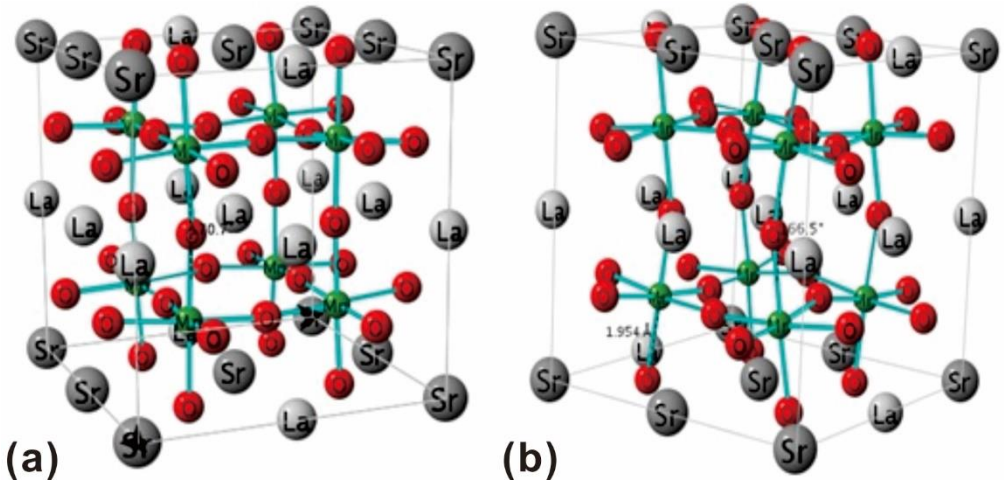

Figure 2.3 The structural distortion of (a) the idea structure and (b) the real structure by partial substituted La^{3+} to Sr^{2+}.

On the other hand, when the A site ions are larger or B site ions are smaller compared to the ideal values, *i.e.* $t > 1$, the structure of perovskites tends to be the

hexagonal structure, *e.g.* $BaNiO_3$ type structures with $t = 1.13$. In this case the closest packing layers are stacked in a hexagonal manner in contrast to the cubic one in $SrTiO_3$ structure which leads to face sharing of the BO_6 octahedra. However, since perovskites are not truly ionic compounds and t values vary with the ionic radii, the tolerance factor *t* can only show a rough estimation.

(2) Composition Effects

Perovskite lattice could accommodate a great variety of metallic ions if the size and valence are compatible. Substituting ions with different valences on the A site will result in different valences for the ion on the B site and thus cause a distortion of the crystal lattice and a rotation of the oxygen oxtahedra. The presence of interstitial ions is impossible for perovskites due to its packing density; however, substantial concentration of A-site vacancies can be tolerated. An example shown in figure 2.3 is that part of La^{3+} is replaced by Sr^{2+} which results in a mixture of Mn^{3+} and Mn^{4+}.

No obvious evidence shows the existence of any significant concentration of vacancies in B site of any perovskite. Compositions with stoichiometry would tend to yield a perovskite with B site vacancies crystallize rather than a mixture of perovskite and non-perovskite phases. For example, in the family of compounds $SrFeO_x$ $(2.5 \leq X \leq 3)$, the valance of the Fe ions is dependent on temperature, which results the oxygen content in the range of 2.5 to 3. For $SrFeO_{2.875}$, the valence of Fe ions is considered as a mixture of Fe^{3+} and Fe^{4+} and thus FeO_5 square pyramids are formed.

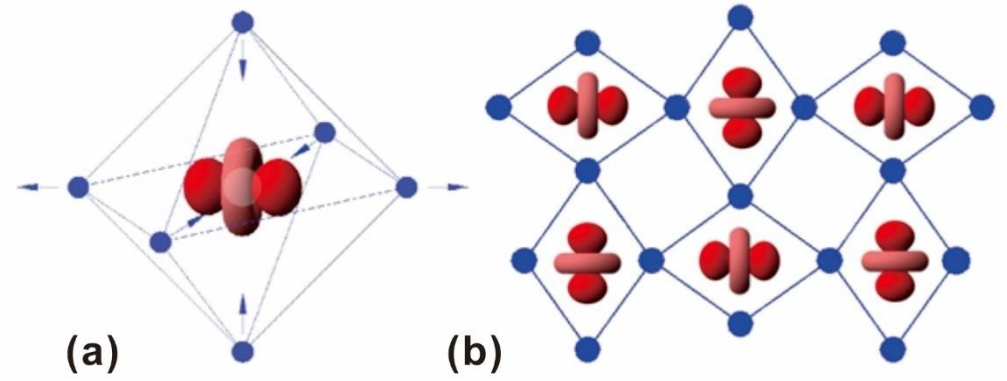

Figure 2.4 Schematic of (a) distortion direction of BO_6 octahedra by two different types of the Jahn-Teller effects and (b) the arrangement of distorted BO_6 in perovskites[38]

(3) Jahn-Teller Effects

The Jahn-Teller effects, named after Hermann Arthur Hahn and Edward Teller who proved that nonlinear spatially degenerate molecules cannot be stable, are commonly appearance in perovskites. It describes that some symmetry-breaking interaction with the removal of the electronic degeneracy will happened in the perovskites with multiplicity of electronic states interacting with lattice. This effect tends to occur spontaneously because the energy penalization of the lattice distortion rises as the square of the distortion while the energy splitting of the otherwise degenerate orbitals is linear. Thus it is energetically favorable to distort the lattice and thus removing the degeneracy. Two types of distortion are relevant for the Jahn-Teller effects shown in figure 2.4.

As a result, the perovskite structure has a wide range of substitution of the A site cations with neutral balance and appropriate doping ionic size. With the variation of

ionic sizes and composition, perovskites show a large variety of physical and chemical properties, which makes them interesting for basic research and technological application.

2.2 Strontium Doped Lanthanum Manganite Structure and Physical Property

Since CMR effect was discovered in distorted perovskite manganites of the type $La_{1-x}A_xMnO_3$, numerous studies in the microstructure of these materials relating to their magnetic and electrical properties have been performed in the last 20-30 years[39]. Among these materials, strontium substituted lanthanum manganite ($La_{1-x}A_xMnO_3$) have drawn significant interest for spintronic application because it combines high carrier spin polarization, the highest Curie temperature ($T_C = 370\,K$ for $x \approx 0.33$) associated with an insulator-to-metal temperature transition seen so far. Such high-temperature transition, and low carrier density (10^{21}~10^{22} cm^{-3})[40]. Moreover, it is also considered as the most investigated cathode material for solid oxide fuel cells.

2.2.1 Crystal Structure and Phase Transition

Strontium-substituted lanthanum manganite, which belongs to ABO_3 perovskite oxide family, is approximated by a face-centered-cubic (fcc) structure. The larger rare earth ions (e.g. La) occupy the 12 coordinated A-sites, the transition metal ions (e.g. Mn) are located at the body center and O occupies the six faces of the cube shown in figure 2.5(a). It is important to note that each Mn^{3+} ion is caged by the O^{2-} octahedron. Locally this forms MnO_6 complex with the Mn ion in the symmetric central position

surrounded by six light oxygen ions. This is the basic building blocks of the manganites. The Mn^{3+} ion contains five-fold orbital degeneracy which is split by the cubic crystal field into two terms, t_{2g} and e_g in figure 2.5(b). The t_{2g}-level contains three electrons that form the so-called "t-core". The last d-electron (e_{2g}-electron) is well separated in energy and forms a loosely bound state. This e_g electron plays a key role in conducting and other properties of manganites as well as in determining its magnetic order. The Hund's rule demands that the three d-electrons forming the "t-core" have the same spin-orientation; as a result, the localized "t-core" has the total spin S=3/2. The e_g electron is also affected by the same strong Hund's interaction. Therefore, its spin must be polarized along the same direction as for the t-core. Even though comparing to t_{2g} electrons, the e_g electron is more strongly hybridized with the O 2p state, it still becomes localized and leads to the Mott insulating states unless carrier-doping. As Sr^{2+} doping concentration, which induces itinerant holes, increases to 0.3~0.4, it leads to a roughly equal number of Mn^{3+} and Mn^{4+}. The conduction band of $La_{1-x}Sr_xMnO_3$ would be either more ($x < 0.5$) or less ($x > 0.5$) depending on the doping concentration. The fully occupied t_{2g} band and partially occupied e_g band in hole-doped $La_{1-x}Sr_xMnO_3$ (LSMO) are separated from the empty minority bands by a large Hund's energy of about 2.5 eV for $x < 0.5$. The oxygen 2p states are fulfilled for both spin orientations and the electronic structure near the Fermi level is dependent on the hybridization between the majority spin Mn-e_g states and the O-2p. The

minority spin states and the O-2p band are separated by an insulating band gap and therefore only majority carriers are present at the Fermi level, which makes $La_{1-x}Sr_xMnO_3$ half-metal for $x = 0.3 \sim 0.4$. The 100% spin polarization at the Fermi level of LSMO is much larger than ferromagnetic 3d transition metals with about 40% spin polarization[41-44].

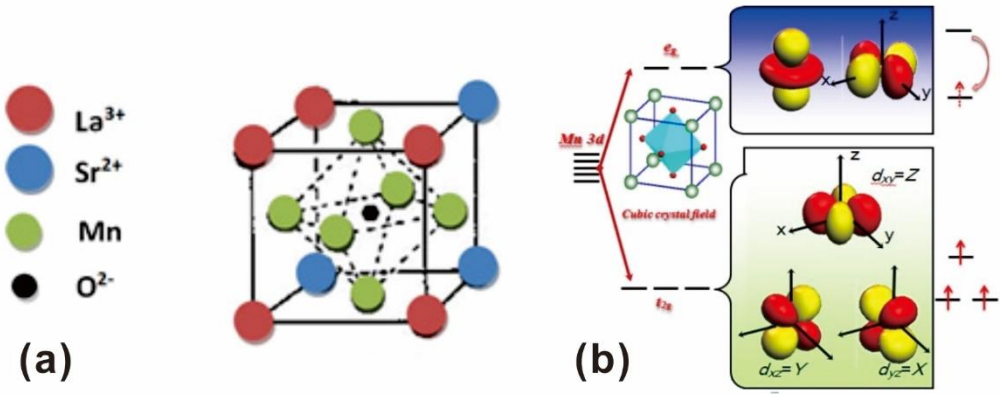

Figure 2.5 (a) Crystal structure of $La_{1-x}Sr_xMnO_3$; (b) the electronic structure of Mn^{3+} in oxygen octahedron

Numerous studies have been conducted to investigate the crystal structure with different doping level[45-51]. Hashimoto *et al.* reported that the structure of $La_{0.9}Sr_{0.1}MnO_3$ is orthorhombic ($P222_1$) with *a*=0.55464, *b*=0.55919 and *c*=0.77408 nm[45]. After increasing the Sr content increased to 0.2 ($La_{0.8}Sr_{0.2}MnO_3$), the structure transferred to a monoclinic symmetry with *a*=0.5484, *b*=0.55349, *c*=0.77916 nm and β=90.746° (*P* 2/*c*) and maintained with the Sr doping up to 0.4. The unit cell volume decreased as Sr doping increased. Hammouche *et al.* characterized $La_{1-x}Sr_xMnO_3$ ($0 < x < 0.5$) as hexagonal-rhombohedral distorted perovskites and found that

in-plane lattice parameters *a* decreased as increasing Sr content, which was due to the creation of Mn^{4+}, and out-of-plane parameters *c* were independent of doping content[46]. Millini *et al*. further calculated their unit cell volumes and summarized as $V = 355.99 - 21.188x$ (Å^3), where x represents the doping content[47]. Zhang and coworkers further observed three different perovskite-type phases at room temperature which are orthorhombic for $0 < x < 0.15$, hexagonal for $0.15 < x < 0.45$ and cubic for $x > 0.45$, respectively.

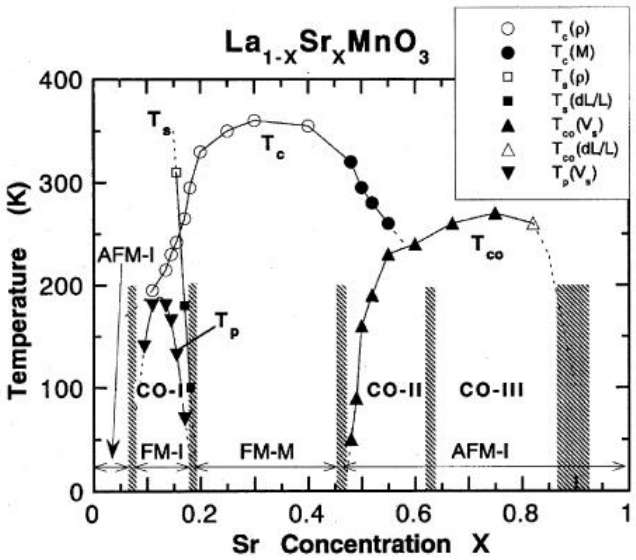

Figure 2.6 Phase diagrams showing transition temperature versus concentration, x, of single crystals of $La_{1-x}Sr_xMnO_3$, where AFM-I is antiferromagnetic insulating, FM-I is ferromagnetic insulating, FM-M is ferromagnetic metallic and CO is charge orbital[52, 53]

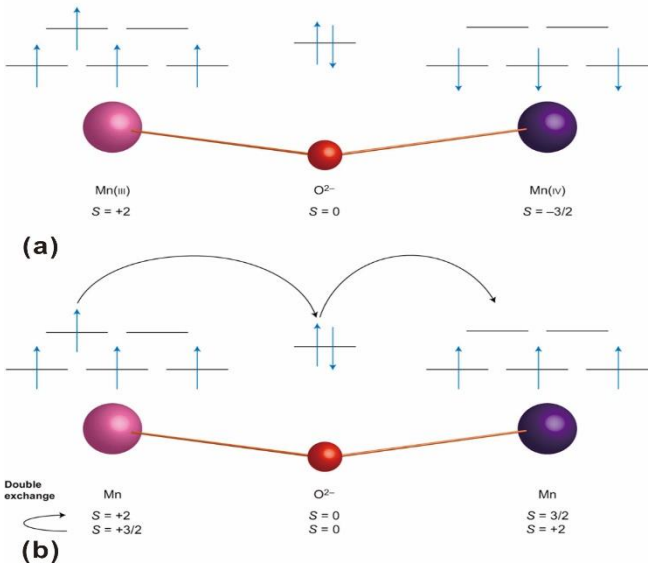

Figure 2.7 Schematic representation of the double exchange mechanism

The phase diagram of Sr doped perovskite manganite is rich with different resistive/magnetic as well as structural phases shown in figure 2.6. From the diagram, an antiferromagnetic insulating (AFM-I) phase of $La_{1-x}Sr_xMnO_3$ is firstly observed with low doping level ($x < 0.1$). As the doping concentration increased, it turns to be a ferromagnetic insulating (FM-I) for $x < 0.2$, and eventually a stabilized ferromagnetic metallic (FM-M) for $x = 0.2 \sim 0.4$. Transition temperature from metal to insular is observed at T_{MI} with $x = 0.3$, which is close to T_C. Both the metal-insulator and the paramagnetic-ferromagnetic phase transitions are dependent on the electronic distribution with spin-up and spin-down states and the width of the impurity band. The size of the A site cations related to the tolerance factor, the average Mn-O bond distance, and the Mn-O-Mn bond angle of the MnO_6 octahedra are essential factors concerning on the magnetic and transport properties in this correlated electron system.

The two transition temperatures T_{MI} and T_C can either coincide for single crystals or epitaxial thin films or vary substantially depending on the presence of structural defects and grain boundaries[52, 53].

The transition from antiferromagnetic insulator to ferromagnetic metal is generally explained by double exchange (DE)[54, 55] between localized 3d magnetic moments with strong on-site Hund's coupling. Base on DE model, both ferromagnetism and metallic transport are essentially governed by the hopping possibility of e_g electrons between adjacent Mn^{3+} and Mn^{4+} along the Mn-O-Mn chains shown in figure 2.7. This possibility is largest when the Mn spins are aligned parallel since electrons are forbidden to transfer with different spin orientation. Anderson and Hasegawa reported later that transfer integral varies as the cosine of the angle between adjacent spins[56]. Hence, charge carriers would achieve higher mobility in the ferromagnetic phase comparing to the paramagnetic phase, where the carriers are localized due to randomly aligned Mn spins. Mechanisms such as magnetic field or temperature, which could modify the spin alignment, can increase the carrier mobility and therefore, the electrical conductivity. As temperature decreased, ferromagnetic spin alignment would help to lower the combined itinerant and local moment system energy, which allows the itinerant electrons to gain kinetic energy[57]. Furthermore, Millis et al[58-60] calculated the resistivity within DE model and concluded that the DE interaction alone cannot explain CMR in manganites[53]. They further argued that the electron-phonon coupling

due to Jahn-Teller effects should be taken into account. Therefore, the DE model with the inclusion of Jahn-Teller distortions is used for explaining the CMR effect and the high-temperature paramagnetic phase in manganites.

2.2.2 Magnetoresistivity

Magnetoresistivity (MR) is the responsibility of materials which are under an external magnetic field. In an external magnetic field the spin arrangement changes and subsequently the mobility of the electrons. The magnitude of the effect is generally defined by the equation:

$$\mathrm{MR}\% = \frac{\rho_0 - \rho_H}{\rho_0} \times 100\% \qquad \text{Eq.2.2}$$

where ρ_H and ρ_0 are the resistivities at a given temperature on the application and without magnetic fields, respectively. The sensitivity of magnetoresistive effects is defined by:

$$S = \frac{\Delta R}{R} / H_S \qquad \text{Eq.2.3}$$

with the unit of S given in %/Oe and H_s being the minimum external field which leads to a saturation of the magnetoreisitive effect.

In $La_{1-x}Sr_xMnO_3$, MR mechanisms are activated by two different types, which are colossal magnetoresisitance (CMR) and low-field magnetoresistance (LFMR).

2.2.2.1 Colossal Magnetoresisitance

During last decades, heterogeneous ferromagnetic materials such as thin film multilayers and cluster-alloy compounds have drawn significant interest due to their

exhibition of a large MR ratio which is so-called giant magnetoresistance (GMR) in application of magnetic recording technology. More recently, it has become recognized that some materials, specifically 3d transition-metal oxides, possess extraordinary large magnetoresistance named CMR in the vicinity of the insulator-metal as well as paramagnetic-ferromagnetic transition. About half a century ago Jonker and Santen described the preparation of polycrystalline samples of (La, Ca)MnO_3, (La, Sr)MnO_3 and (La, Ba)MnO_3 manganites and reported ferromagnetism and anomalies in the conductivity at the Curie temperature with variation in lattice parameter as a function of hole doping[55, 61, 62]. A few years later Volger[63] (1954) observed a notable decrease of resistivity for $La_{0.8}Sr_{0.2}MnO_3$ in the ferromagnetic (FM) state in applied magnetic fields. After these pioneering experiments, Wollan and Koehler[64] carried out extensive neutron diffraction study to characterize and draw the first ever magnetic structures (phase diagram) of $La_{1-x}Ca_xMnO_3$ (LCMO) in the entire composition range. They found that in addition to FM phase many other interesting antiferromagnetic phases were also present in manganites. After that Jirak et al[65] and Pollert et al[66] studied the structure and magnetic properties by x-ray and neutron diffraction techniques. They have also observed charge-ordered phases which are totally different from the ferromagnetic phases of other manganites.

A burst of research activity on manganites started during 1990 because of the observation of large magnetoresistance. Kusters et al[67] reported a large MR effect on

bulk $Nd_{0.5}Pb_{0.5}MnO_3$ shown in figure 2.8. Von Helmholtz et al[39] further found a large MR effect on thin films of $La_{0.67}Ba_{0.33}MnO_3$ at room temperature. Later then, a similar conclusion was reported by Chahara et al[68] using $La_{0.75}Ca_{0.25}MnO_3$ thin films and by Ju et al[69] for $La_{1-x}Sr_xMnO_3$ thin films. They all observed MR values larger than those observed in artificially engineered multilayers (GMR). A defining moment for the field of manganites was the publication by Jin et al[70] of results with truly colossal magnetoresistance (CMR). They reported MR close to 1500% at 200 K and over 100,000% at 77 K for thin films of $La_{0.67}Ca_{0.33}MnO_3$. This enormous factor corresponds to a thousand-fold change in resistivity with and without the field. One year later, Xiong et al[71] reported an over 100,000% MR ratio in the presence of a magnetic field of 8 T at 60 K on $Nd_{0.7}Sr_{0.3}MnO_3$ thin films. These studies showed that manganites could be a potential alternative for giant MR systems.

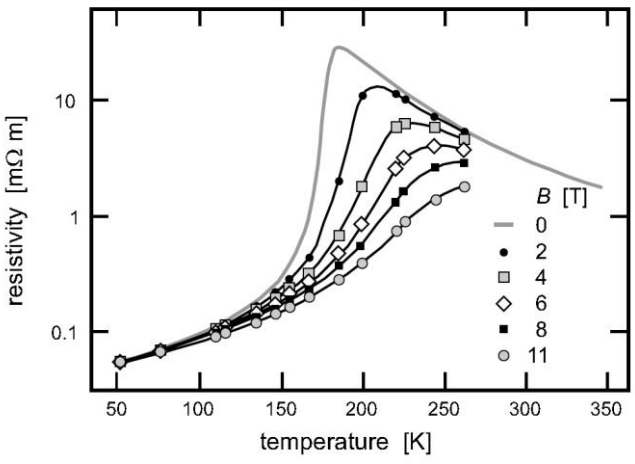

Figure 2.8 Resistivity of $Nd_{1-x}Pb_xMnO_3$ with x = 0.5 as a function of temperature and applied magnetic field[67]

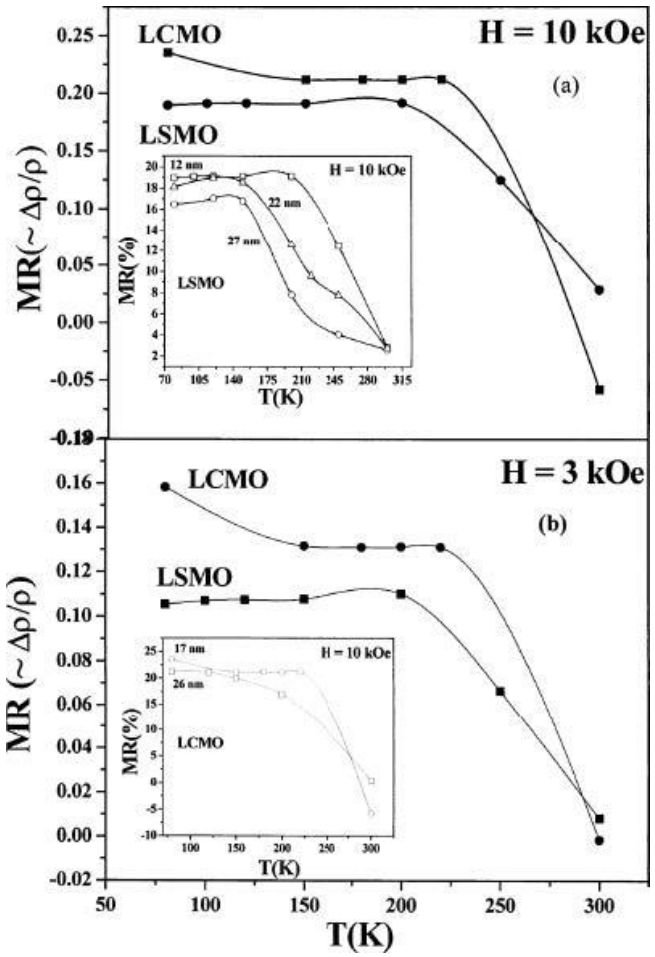

Figure 2.9 MR versus T in the temperature range of 80–300 K for LSMO and LCMO samples at (a) 10 and (b) 3 kOe, respectively. Insets of (a) and (b) show the MR–T curves at 10 kOe for varying particle sizes of LSMO and LCMO, respectively[72]

2.2.2.2 Low-Field Magnetoresistance

Instead of the suppression of spin fluctuations in a large applied magnetic field for CMR, LFMR is due to the suppression of spin-dependent scattering at grain boundaries or tunneling between grains, which only requires a small magnetic field[73]. When the temperature is below T_C under ferromagnetic phase, the conduction

electrons are almost fully polarized which makes electrons transfer easily through Mn-O-Mn chains. Thus, the resistance of manganites in single crystals or epitaxial thin films does not have extraordinary change applied by a small magnetic field. However, for polycrystalline bulk or thin film manganite, the randomly aligned magnetic domains and grain boundaries can act as insulating scattering centers for spin-polarized electrons, which therefore increases the zero-field resistivity. Two types of effects are related to LFMR, which are the transfer of electrons from one magnetic domain hopping to another through an intermediate insulating layer by a spin-dependent tunneling process (<500 mT) and suppression of spin fluctuations at grain boundaries at larger fields (>500 mT). The possibility of spin dependent tunneling highly depends on the spin state of adjacent grains. Since half of the domains switch their magnetic orientation under the coercive field, there would be a smallest tunneling probability of electrons and largest electrical resistance at H_C. After magnetization into parallel direction with the external magnetic field, the tunneling probability rebuilds up inducing electrical resistance dropped. Up to 20% LFMR in polycrystalline LSMO thin films on single-crystal (001) yttria-stabilized zirconia substrates has been reported[74]. The suppression of spin fluctuations at grain boundaries could also generate the negative MR effect applied by a certain magnetic field.

Several models have been used in order to describe the temperature dependence of electrical conductivity in bulk and thin films of LSMO. In the

low-temperature ferromagnetic phase, the resistivity of LSMO was summarized with the following equations[75]

$$\rho = \rho_0 + \rho_2 T^2 \quad \text{Eq.2.3}$$

$$\rho = \rho_0 + \rho_{2.5} T^{2.5} \quad \text{Eq.2.4}$$

$$\rho = \rho_0 + \rho_2 T^2 + \rho_{4.5} T^{4.5} \quad \text{Eq.2.5}$$

where ρ_0 is the resistivity due to temperature-independent scattering on impurities, defects, domain walls and grain boundaries. Generally, with applied a magnetic field, ρ_0 could decrease dramatically due to an improved spin alignment at grain boundaries and domain walls. A variety of scattering sources are considered as the reason of the temperature dependence of the resistivity. Urushibara et al[75] found the well fitted resistivity with Eq.2.3 in single crystal LSMO below 200 K and claimed that the T^2 term should be considered as electron-electron scattering. Furthermore, a $\rho \propto T^{4.5}$ term in Eq.2.5 is introduced to take into account additional electron-magnon scattering for DE systems[57]. Eq.2.4 provides a better fit to some experimental data. Thus, electron-phonon scattering does increase the resistivity of LSMO at high temperatures.

2.3 Effects of Strains on Perovskite Manganite

The magnetic and electrical transport properties of perovskite manganites are governed by lattice-charge-spin coupling, which is very sensitive to all types of perturbation such as phase and structural order, oxygen stoichiometry and lattice

distortions[22, 76, 77]. Especially, it has been found in bulk materials that the magnetotransport properties are highly controlled by the internal pressure caused by the variation of the average size of the A site cation or external pressure through hydrostatic pressure. The strain-modified mechanisms have two distinct origins: (1) through magnetoelastic coupling, strain can couple into the orbital degree of freedom and modify the magnetic anisotropy of the system; (2) by changing the oxygen-manganese bond angle and length, a change in the electron hopping rates and orbital occupation can be effected, such as the spin exchange interaction and charge transport[78-81]. Many studies have been focused on the strain-induced properties of perovskite manganites experimentally and theoretically. Thus, it is necessary to correctly understand the strain effects in order to obtain the desired properties. Two types of strain, which are in-plane (i.e. substrate-induced strains) and out-of-plane strain (i.e. thickness dependence) respectively, will be discussed in the following section

2.3.1 Substrate-induced Strains

The substrate-induced strain is undoubtedly the first important source of intrinsic strain especially in epitaxy thin film. The substrates most commonly used to grow manganites are MgO (cubic, *a*=4.205 Å), $SrTiO_3$ (STO, cubic, *a*=3.905 Å), $LaAlO_3$ (LAO, pseudocubic, *a*=3.788 Å), $NdGaO_3$ (NGO, orthorhombic, *a*=5.426 Å, *b*=5.502 Å

and *c*=7.706 Å) and Si (cubic, *a*=5.43 Å). The lattice mismatch *m* along the interface is defined by

$$m = (a_S - a_L)/a_S \qquad \text{Eq.2.6}$$

where a_L and a_S are the layer and substrate unit cell parameters, respectively. Positive values of mismatch correspond to in-plane tensile strains shown in figure 2.10(a), while negative values stand for compressive stresses which elongated the unit cell along the growth direction and compressed in the film's plane shown in figure 2.10(b). The influence of the substrate is primarily on the lattice parameter. Adamo et al have deposited (001) $La_{0.7}Sr_{0.3}MnO_3$ epitaxial thin films on various single crystalline substrates, varying the substrate-induced biaxial strain from -2.3% to +3.2%, by reactive molecular-beam epitaxy (MBE) method shown in figure 2.11[82].

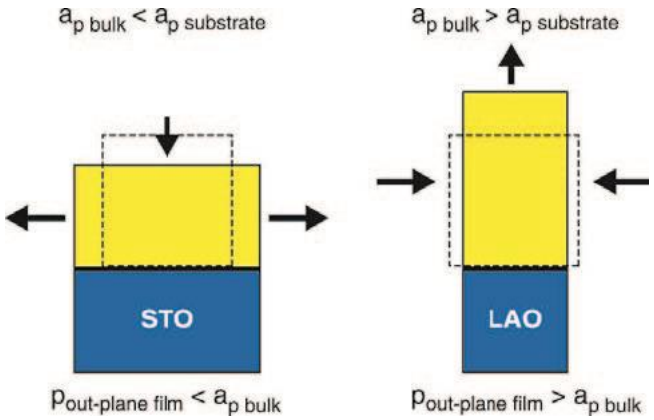

Figure 2.10 Schematic drafts of the lattice cell distortion in a strained epitaxial thin film (a) under tension or (b) compression[83]

2.3.2 Thickness Dependence

The thickness (*t*) effect on the perovskite manganites is primarily seen in both the in-plane and out-of-plane lattice parameters of the films. It is common sense that the volume of the unit cell is conserved in the thin film compared to the bulk value. However, the previous study on $La_{0.8}Ca_{0.2}MnO_3$ epitaxial thin films deposited on (001) STO and LAO proved that the unit cell volume is not conserved and varies with the substrate as well as the film thickness shown in figure 2.12[84, 85].

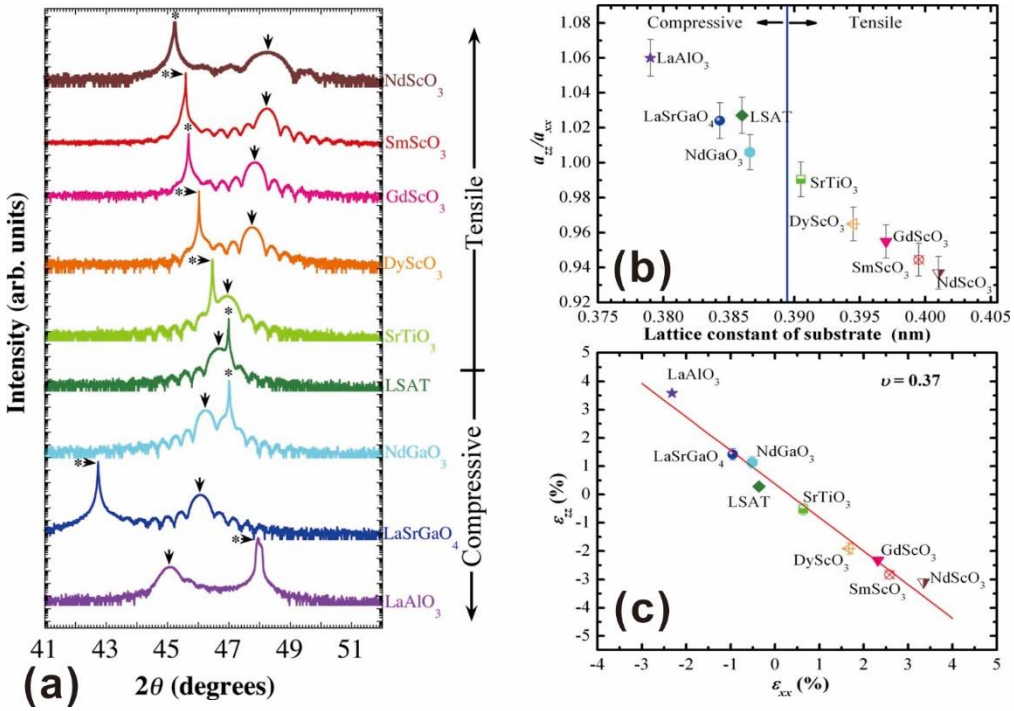

Figure 2.11 θ-2θ x-ray diffraction scans of 22 nm thick $La_{0.7}Sr_{0.3}MnO_3$ epitaxial thin films grown on different substrates; (b) ratio between in-plane and out-of-plane lattice spacing of $La_{0.7}Sr_{0.3}MnO_3$ thin films as a function of the substrate lattice parameter; (c) the out-of-plane lattice strain as a function of in-plane lattice strain[82]

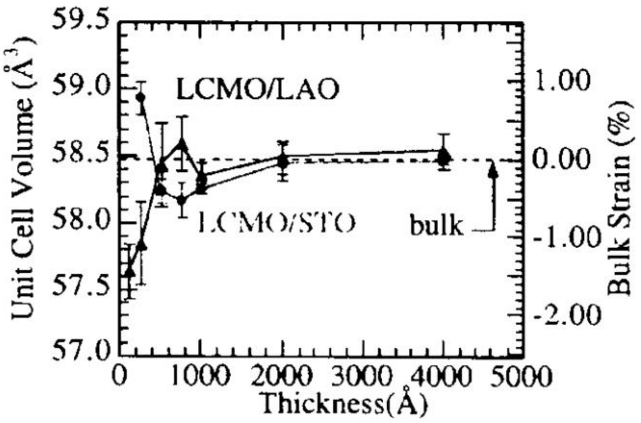

Figure 2.12 Thickness dependence of the perovskite unit-cell volume of epitaxial thin films on (001) LAO and (001) STO

Moreover, the thickness effect on the perovskite manganites is mainly concerning on gradually changing of the out-of-plane and in-plane lattice parameters, which is close to the bulk value, as a function of the film thickness. For example, the out-of-plane parameter increases from a value of 3.8 Å for a 200 Å thick film to 3.86 Å for a 1000 Å film in the case of $Nd_{0.67}Sr_{0.33}MnO_3$[86]. Angeloni et al[87] have reported similar results in $La_{0.7}Sr_{0.3}MnO_3$ epitaxial thin films on both LAO and STO substrates by pulsed laser deposition (PLD) and further distinguished three different regions, which are under fully, partially strain and fully relaxed respectively, in XRD pattern shown in figure 2.13. Maurice et al[88] and Ranno et al[89] reported on the thickness effects of $La_{0.67}Sr_{0.33}MnO_3$ on (001) $SrTiO_3$ by using x-ray diffraction (XRD). Two regimes were differentiated: below a critical thickness ($t = 100$nm), there was a standard strained tetragonal regime while a more complicated regime, which was

called “relaxed regime”, was observed with a thickness above 100 nm. Up to three different lattice parameters were detected in the latter regime. They attributed this relaxation mechanism to a two-layer system: a fully strained layer and a slowly relaxing layer with an increasing c parameter. Jiang et al[90, 91] also observed a similar critical thickness of $La_{0.8}Sr_{0.2}MnO_3$ on (001) $LaAlO_3$ with a columnar nanostructure evolving when the film thickness was above the critical thickness[92]. This is because that the strain energy building up in the layer is proportional to the layer thickness. When the layer's thickness exceeds a certain value, known as the critical thickness, this energy becomes so high that a misfit dislocation appears at the interface, which partially or completely relieves the stresses in the bulk of the layer.

2.3.3 Strain Effects on the Magnetic Anisotropy

The magnetic anisotropy of epitaxial manganite thin films is usually much larger than that of bulk materials, depending on the strength of the strain. A correlation between the unit cell distortion ($\delta = c/a - 1$) and the anisotropy coefficient was demonstrated for (001) LSMO single crystal. The general trend is that the stronger the distortion of the MnO_6 octahedron, the larger the anisotropy. For an elongated octahedron such as film under compression on $LaAlO_3$, the anisotropy is positive while it is negative for a compressed octahedron such as film under tension on $SrTiO_3$.

The uniaxial anisotropy energy $K_U\sin^2\theta$ has been determined to be $K_U = -0.9 \times 10^5\ erg\ cm^{-3}$ at 100 K[93] and $K_U = -0.18 \times 10^5\ erg\ cm^{-3}$ at 300 K[94] in the (100)

plane of pseudo-cubic LSMO single crystal. It is known that the anisotropy is expressed by both the magneto-crystalline term and the magnetostriction term in thin films[95]. Thus, at low temperatures, the film plane is considered as magnetization easy plane in tensile films deposited on STO while the out-of-plane growth direction is the easy direction of compressive films on LAO.

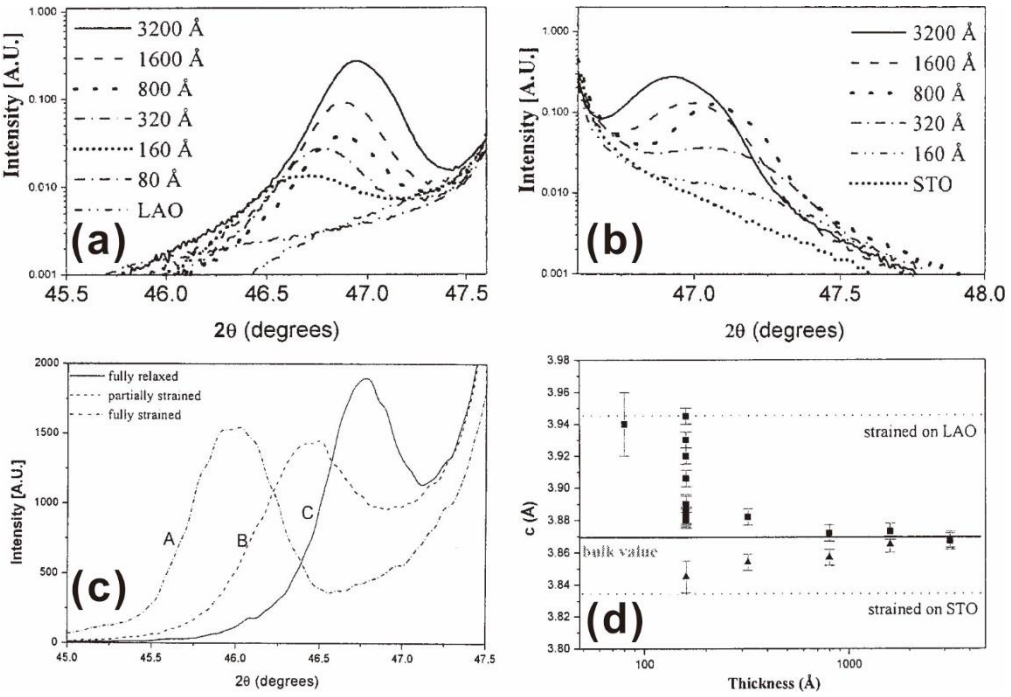

Figure 2.13 θ-2θ x-ray diffraction spectra for various LSMO films with different thickness values grown on (a) LAO substrates and (b); (c) three LSMO films deposited on LAO. A, B, and C refer to fully strained, partially strained, and completely relaxed films, respectively; (d) behavior of out-of-plane lattice parameter *c* as a function of the film thickness[87]

Tsui et al[96] have systematically studied the strain effects on the anisotropy of LSMO thin films deposited on (001) STO, LAO, NGO and $La_{0.3}Sr_{0.7}Al_{0.65}Ta_{0.35}O_9$ (LSAT) substrates. He claimed that an easy axis for magnetization along the <100> direction was found in LSMO grown on LAO at low temperature while this axis rotated towards the plane at higher temperature. Moreover, at low temperature, tensile LSMO thin films on STO exhibit the in-plane <110> anisotropy while both <100> and <110> directions are equivalent at high temperature[46, 94, 97, 98]. Furthermore, a "bubble" magnetic pattern or "maze-like" pattern was observed on LAO substrate and a different "feather-like" pattern was found in the films on STO at 300 K by magnetic force microscopy (MFM)[99]. The pattern can only be observed with a thickness between 50 nm and 170 nm[100]. The thickness dependent can be explained as that by increasing thickness, the strain between film and substrate will get relaxed which degrades the magnetic anisotropy. This confirms that the anisotropy is totally governed by the symmetry of the substrate and that lattice strains induce an additional anisotropy along the direction of the strain. A distorted biaxial anisotropy with easy axes between <100> and <110> planes grown on LSAT. This anisotropy can be considered as a superposition of a uniaxial anisotropy along <100> and a biaxial anisotropy along <110> directions. In the films on NGO, a weak biaxial anisotropy along <100> was also observed. It shows that the compressive stress is not sufficient

to induce an out-of-plane easy direction for magnetization for the films on both NGO and LSAT substrates.

2.3.4 Strain Effects on Dead Layers

The saturation magnetization also decreases with decreasing thickness. Many authors have attributed this loss of moment to strain effects at the substrate–film interface. Structural distortion and composition non-homogeneity near the interface. In highly tensile stressed LSMO films grown on MgO (δ = +7.9%), Borges et al have precisely determined both electrical and magnetic dead layers. Using a simple model based on two parallel resistors, a fit for the conductivity $\sigma \sim \sigma_B(t - t_D)/t$ gives $t_D = 4$ nm for the thickness of the electric dead layer (with $\sigma_B = 2.76 \times 10^{-3} \mu\Omega^{-1}cm^{-1}$). This value approaches the value measured in weakly strained LSMO grown on LAO and NGO, which suggests that the strain at interface is released in a thickness less than the dead layer. Thus, an electrically dead layer should also be present at the film surface. Also, two magnetically dead layers are present at both film/substrate interface and film surface, with a total thickness of around 25 nm whatever the thickness (20 nm < t < 60 nm). The magnetization falls off rapidly inside these interfaces due to a spin canting that induces a loss of polarization. This loss of polarization has been confirmed by spin-resolved photoemission spectroscopy (SPES) on thick 130 nm LSMO films tensile strained on STO.

2.3.5 Strain Effects on the Curie Temperature

It is commonly found that the epitaxial strain between the substrate and film would highly depress T_C compared to its bulk counterpart. Millis *et al* have developed a model to illustrate the dependence of a biaxial strain on T_C. The three dimensional strain induced by the substrate can be decomposed into a bulk strain (hydrostatic term) and a biaxial strain (Jahn-Teller distortion), which have opposite effect on T_C. A hydrostatic compression will tend to increase the hopping and thereby reduce the electron-lattice coupling, inducing an increase in both the conduction band width and T_C. On the other hand, a biaxial strain increases the energy differences between the e_g levels imposed by the Jahn-Teller distortion which reinforce the electrons tendency to become more localized decreasing T_C. The dependence of T_C on the biaxial strain can be expressed as

$$T_C(\varepsilon) = T_C(\varepsilon = 0)\left(1 - \alpha\varepsilon_B - \frac{1}{2}\beta\varepsilon_{bi}^2\right) \qquad \text{Eq.1.1}$$

where ε_B is the bulk strain, ε_{bi} is the biaxial strain, $\alpha = (1/T_C)\, dT_C/\, d\varepsilon_B$ is related to the unit volume cell variations under strain and β accounts for the Jahn-Teller energy splitting. It shows that about 1% lattice mismatch would increase T_C by 10% in compressive strained thin film, while tensile strain usually suppress T_C, which is described as a decrease in the electron transfer due to stretched Mn-O bonds. Many experimentally data using LCMO and LSMO thin films with different substrates have been confirmed Eq.2.7 shown in figure 2.14[100-102]. However, it could not conclude

easily despite of these agreements between experimental data and equation. T_C should be also governed by other factors such as magnetic disorder at interfaces, loss of oxygen at interface and oxygen vacancies. In conclusion, it appears that manganite films with large *c/a* values can exhibit a higher Curie temperature than the corresponding bulk materials, even if they are deposited under tensile strain.

Since the insulator-to-metal transition temperature T_p decreases strongly with increasing biaxial distortion ε_{bi} for both tensile and compressive thin films, it is important to realize the relaxation of strain in epitaxial LSMO thin films. Thickness effect on strain relaxation have been detailed introduced above, which would partially or completely relieves the stresses over critical thickness. However, high densities of threading dislocations have been observed in partially relaxed epitaxial thin films when the thickness is above the critical value, which would deteriorate the thin film properties such as electronic and magnetic transportation properties. Thus, realization of high transition temperature T_p of epitaxial LSMO thin films, which is essential for practical devices, as well as high quality with low dislocation density, becomes an interesting and difficult task.

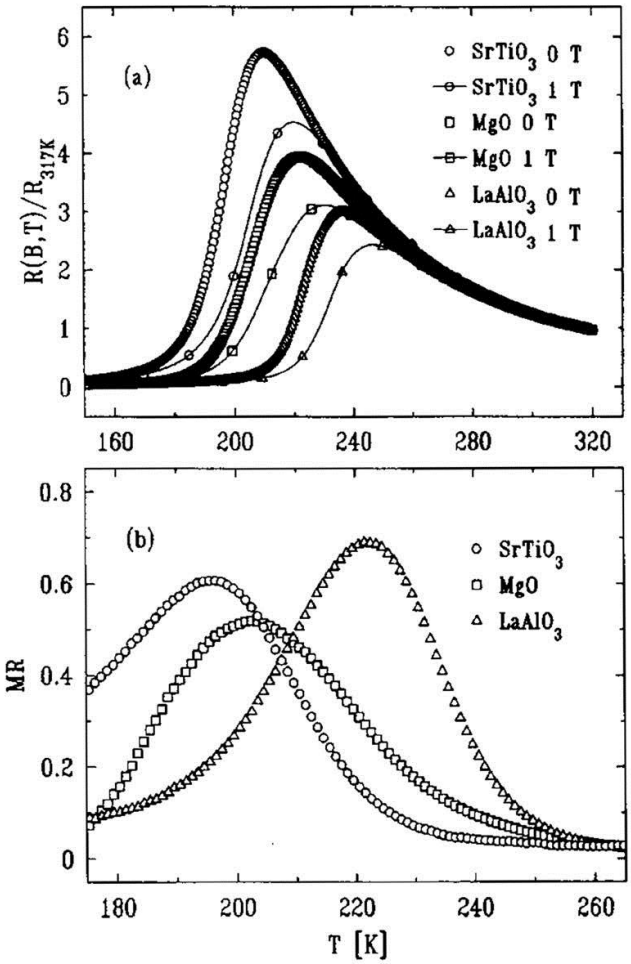

Figure 2.14 (a) $\rho(T)$ for LCMO on various substrates under 0 and 1 T magnetic field; (b) MR defined as $(\rho(0) - \rho(1\,T)/\rho(0))$ normalized to the value at T =317 K[102]

2.4 Strain Relaxation in Si-Ge Structures

For many years, a major problem in crystal heteroepitaxy was the avoidance of strain so as to produce strain-free long-lived devices. Numerous studies in the last decade have been performed on achieving high performance silcon-based devisces and circuits. One such development is the fabrication of epitaxial high-qualigty SiGe/Si heterostructures on Si substrates[103-105]. A fully relaxed compositional graded $Si_{1-x}Ge_x$

buffer layer epitaxially grown on Si (001) substrate was used as substrates for SiGe field effect transistors (FET). For relaxed $Si_{1-x}Ge_x$ buffer layer structures to be useful for FET, the density of misfit segments must be high enough to relieve most of the strain. However, the density of threading dislocations at the surface must be very low because these defects will pass through the active device layers. LeGoues *et al* explained relaxation mechanism and found that the dislocation density are drop from about 10^8~10^9/cm^2 to 10^4~10^6/cm^2 compared to the composition uniform one[106]. Also this graded structure could also prevent forming threading dislocation and thus provide a relaxed, dislocation-free layer on the surface.

2.5 Deposition Techniques of Epitaxial Perovskite-type Oxides

Several thin film techniques have been reported in fabrication of ECG thin films, such as physical vapor deposition (PVD) including pulsed laser deposition (PLD) and sputtering, chemical vapor deposition (CVD), atomic layer deposition (ALD), laser ablation and sol-gel coating[107-111]. Among these fabrication methods, PLD and sputtering with dual-beam have been proposed as useful techniques due to their capability of synthesis of high-quality thin films. Hussey et al[112] reported a dual-beam dual-target PLD method by using YBa_2O_δ and CuO targets simultaneously for obtaining superconducting $YBaCuO_{7-\delta}$ films. On the other hand, by using rf power co-sputtering deposition, Kawakubo et al[113] achieved ECG $Ba_xSr_{1-x}TiO_3$ thin film with

both $SrTiO_3$ and $BaTiO_3$ targets sputtered in various plasma power ratio. Thus, a brief introduction about PLD and sputtering techniques will be included in this section.

2.5.1 Pulsed Laser Deposition

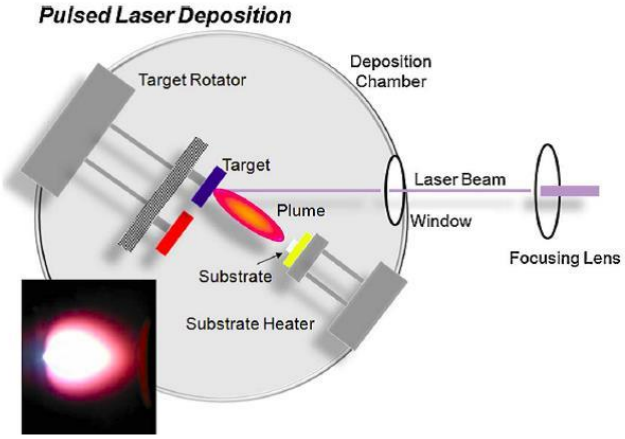

Figure 2.15 Schematic of a standard pulsed laser deposition system

The PLD technique has a very important rule in the creation of oxide materials such as high T_C superconductivity and colossal magnetoresistance materials. It's a very simple thin film growth process and the schematic is shown in figure 2.15. Normally, the system consists of a vacuum chamber with pumps, a target holder and rotator connected to a heater, and also equipped with many pressure gauges and mass flow controllers. The PLD systems are usually equipped with a set of apertures, attenuators, mirrors and lenses in order to focus and locate the laser beam in to the chamber with appropriate energy. One of the advantages of PLD technique is the deposited materials are vapored by the external laser energy source. Moreover, PLD process is quite far from equilibrium and thus is good at preserving complex

stoichiometry. It is also easy to deposit multiple materials and replace the targets. However, the laser equipment is costly and it may generate inhomogeneous films because of ejection of large particles from targets. Also it is not appropriate for large-scale production in industry.

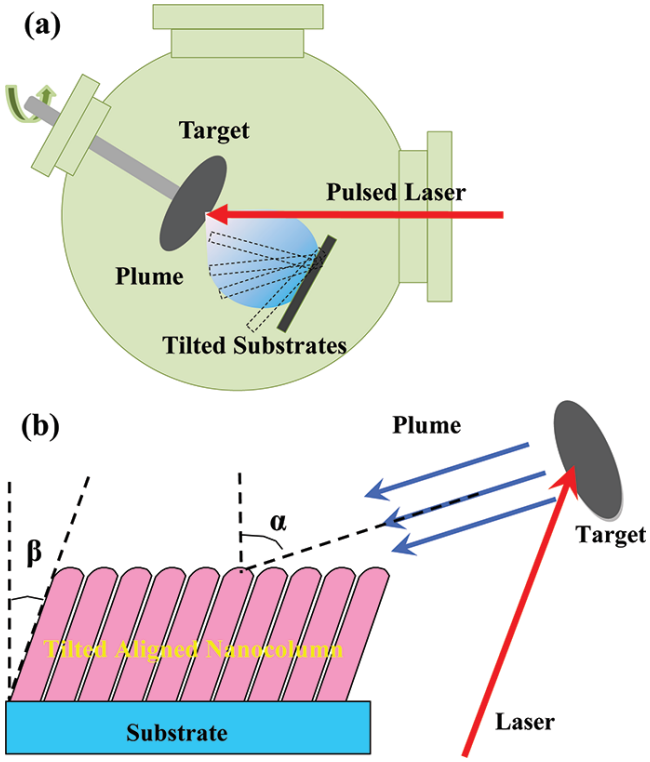

Figure 2.16 (a) Schematic of the pulsed laser oblique-angle deposition configuration; (b) the formation of tilted aligned nanocolumn films by PLOAD[115]

F. Pailloux *et al*[114] reported that they deposited LSMO thin film on (001) SrTiO3 substrates using a frequency tripled Nd: YAG laser with a pulse length of 5 ns at a repetition rate from 1 to 5 Hz. The laser beam was at 355 nm wavelength with a power density from 50 to 600 MW/cm^2. The deposition temperature was 720 ℃ under 0.35

Torr oxygen pressure. After deposition they raised oxygen pressure up to 300 Torr in order to cooling the specimen. XRD and HRTEM have been used to investigate the structure of the film respectively. From the result, a high quality epitaxial LSMO thin film was deposited on $SrTiO_3$ substrate with a rhombohedral structure. The lattice planes normal to the film/substrate interface keep vertical while (001) growth planes tend to get the rhombohedral tilt (0.26°) without changing the lattice parameter.

Another unique PLD technique for deposition of LSMO thin film was reported by Aiping Chen *et al* called pulsed laser oblique-angle deposition (PLOAD), which has been usually used to grow nanostructured porous carbon and $YBa_2Cu_3O_x$. After slightly adjust the deposition angles and temperatures, it is proved to control the nano-column tilting angle and grain boundary density. The illustration of the PLOAD configuration is shown in figure 2.16(a). In their experiments, the plasma plume was adjusted to the tilted substrates with an angle α which could be changed from 0 to 85°. The nanocolumn tilting angle β is the angle between the nanocolumn and the normal of substrate. They deposited LSMO on a single-crystal (001) SrTiO3 with a KrF excimer laser which has a 248 nm wavelength and a frequency of 10 Hz. The laser beam was incidence on the target with 45° angle and an energy density of 4.5 J/cm^2. Deposition temperature was 600 ℃ and oxygen pressure maintained at 100 mTorr during the whole deposition. After deposition, the films were cooled in a 200 Torr oxygen pressure. The as-deposited thin films were then annealed at 550-850 ℃ in air

for 30 min. A cross-sectional TEM was studied in order to understand the structure and morphology of the deposited thin films. The well-ordered and tilted aligned nanocolumn structures were obtained on STO substrate.

2.5.2 PVD Magnetron Sputtering Deposition

Sputtering is a vacuum deposition process, which uses energetic ions to knock atoms or molecules out from a target that acts as one electrode and subsequently deposit them on a substrate acting as another electrode. Compared to PLD, magnetron co-sputtering can provide a cost-effective, high-throughput and relatively low temperature process with large area scalability and co-sputtering capability and thus is more useful in industry application. Various sputtering techniques are used at present like DC sputtering, RF and pulse magnetron sputtering, reactive sputtering etc.; the fundamentals of the sputtering process are the same. Sputtering is driven by momentum exchange between the ions and atoms in the material, due to collisions. Target and substrate serve as electrodes and face each other in a chamber. The chamber is maintained under high vacuum. Then an inert gas, typically argon is introduced in the chamber with very low pressure that ranges from a few mTorr to 100 mTorr, as the medium to initiate and maintain the discharge. When an electric field of several kV is applied between cathode and anode, i.e., target and substrate, a glow discharge is initiated and maintained between electrodes. Free electrons will be accelerated due to the electric field and it ionizes the argon gas by gaining high

amount of energy. Argon ion Ar^+ will be attracted towards cathode and will hit the target, which will result in ejection of neutral atoms from target surface through momentum transfer. These atoms will pass through the discharge and will deposit on the substrate.

The target atoms will sputter; if only enough energy is transferred to overcome the forces bind them. The minimum energy which is named as threshold energy is needed to unbind them. The typical value of this energy is ranging from 5 eV to 40 eV depending on the nature of incident ion and atomic and mass number of target atoms. Also the energy that binds the atoms to the surface should be taken into account.

The RF sputtering system uses an RF power supply and a matching network. The power supply works at high frequency. The most common frequency is 13.56 MHz. RF sputtering essentially works because the target self-biases to negative potential. Once this happens, it behaves like a DC target which positive ion-bombardment sputters away atoms to subsequent deposition. For a small part of RF cycle, the cathode and anode are electrically reversible. This eliminates charge buildup on an insulating surface, by providing an equal number of ions, then electrons, then ions and then electrons. This allows insulators to be sputtered or metals to be sputtered in reactive environment. Another advantage of RF system is that the oscillation of the fields in the plasma results in additional electron motion within the plasma results in enhancement

in electron movement that the probability of an ionizing collision is increased for a given secondary electron, and this result in increase of the plasma density.

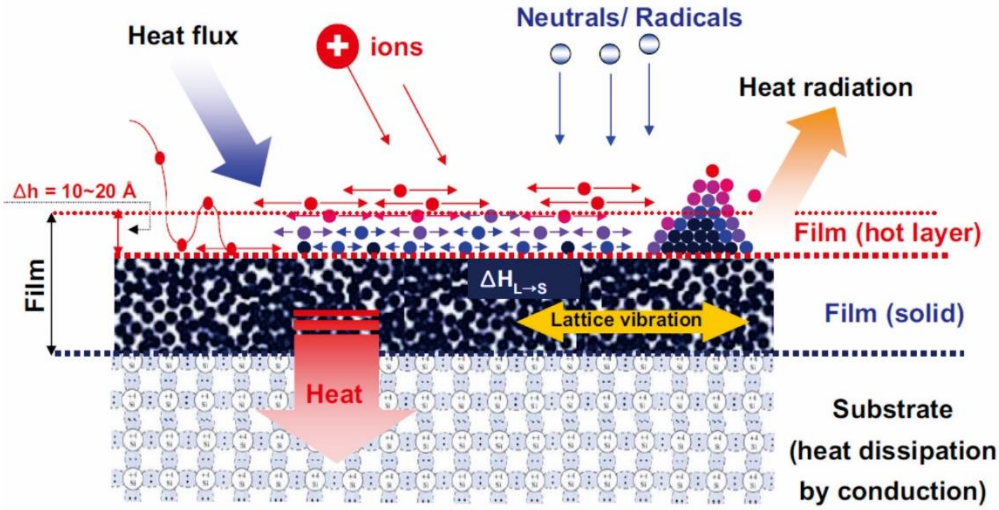

Figure 2.17 Schematic showing the atomistic of film formation on substrates

The sputtering technique has been utilized for deposition of a wide range of materials. The advantage of sputtering include low cost, high deposition growth rate, reproducibility, moderate processing temperature and compatibility with existing industrial semiconductor manufacturing processes. The simple process also can fabricate thin films with variety of shape, size and compositions. Furthermore, sputtering technique is also a contamination-free method compared to other chemically-driven deposition techniques and results in more reproducible characteristics of thin films.

2.5.3 Modes of Film Growth by Vapor Deposition

After the sputtered atoms arrive at substrate surface, the manner of atoms migrate, interact and nucleate is dependent on my deposition process parameters, such as substrate temperature, sputtering power, sputtering gas and background pressure. The film growth usually involves the following steps: (1) condensation and nucleation of the atoms; (2) nuclei growth; (3) interface formation; (4) film growth of nucleation and reaction with previous deposited material; (5) post-deposition modification shown in figure 2.17. There are three major thin film growth modes: (1) Volmer-Weber or island growth, (2) Frank-Van der Merwe or layer-by-layer growth, and (3) Stranski-Krastanov growth. As a simplistic explanation for these three growth behaviors, for island growth, we can consider that the atoms or molecules of the samples are more strongly bonded to each other rather than to the atoms or molecules of substrates. These situations are most likely observed on metal or semiconductor samples deposited on oxide substrates. For layer-by-layer growth the situation is opposite; the atoms or molecules from samples are more strongly bonded to the atoms or molecules from substrates. The nucleuses extend in two dimensions and form planar sheets layer after layer. However the strength of bond between each layer is progressively weakened and will stop when the bulk bonding strength is reached. The typical example is the epitaxial growth of semiconductor and oxide materials. The Stranski- Krastanov growth is actually the combination of the above two

growth. In this growth mode, one or more monolayers will be formed at first followed by Frank–Van der Merwe growth. After then, the Volmer–Weber growth turns into energetically favorable and the island begin to form. This growth is common and usually occurs in metal-metal and metal-semiconductor systems[116, 117].

Chapter 3

Thin Films Synthesis and Characterization

In this research, all thin films were deposited using an off-axis commercial three-gun magnetron sputtering vacuum system with both dc and rf power capability. Three two inch diameter targets, namely $LaMnO_3$ (LMO), $La_{0.67}Sr_{0.33}MnO_3$ and $SrMnO_3$ (SMO) fabricated by K.J. Lesker Co. were utilized for deposition on 10×10 mm (001) single crystal MgO and $LaAlO_3$ (LAO) substrates. The details of the deposition conditions for each film will be introduced in individual chapter below. The microstructures of the thin films were characterized by XRD, XPS, HRTEM and AFM which will be described in the following section.

3.1 Synthesis of Strontium Doped Lanthanum Manganite Thin Films

There are three different types of synthesis method for fabrication of different types of strontium doped lanthanum manganite thin films. First, individual pure LMO and LSMO thin films were deposited on (001) LAO and MgO single crystal substrate using RF magnetron sputtering. This could be considered as preparatory work for fabrication of ECG LSMO thin films. The fundamental epitaxial growth mechanism and optimum growth condition were obtained. Second, ECG LSMO thin films were synthesized on same substrates using co-sputtering deposition with different conditions. Finally, triple layers LMO/LSMO/SMO systems with sandwich structure were also fabricated based on previous investigations.

3.1.1 RF Magnetron Sputtering

Lab-built magnetron sputtering system in the Surface and Nano Engineering Laboratory (SaNEL) was used in this research. Due to its excellent flexibility in adjusting a large number of experimental parameters including pressure, gas mixture, power to the magnetron (both DC and RF), substrate bias, substrate temperature, target material, distance between the target and substrate, and substrate rotation, the system can be widely performed for variety of materials.

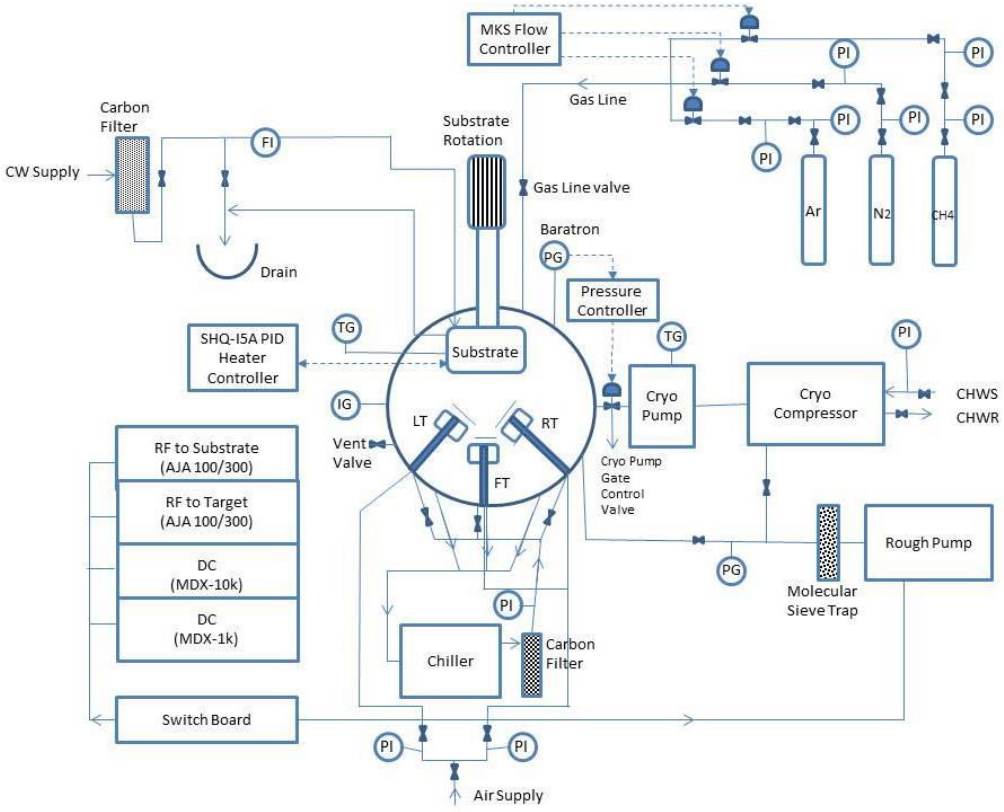

Figure 3.1 Schematic diagram of the PVD magnetron sputtering system

The lab-built PVD magnetron sputtering system with DC and RF capabilities is consist of chambers, substrate holder (with heating and rotation sections), power supplies, pumps,

valve, magnetron gun and cooling system shown in figure 3.1. The cylinder shaped stainless steel chamber, which is 47 cm diameter wide and 50 cm height, is installed three 2-inch diameter magnetron guns mounted at the bottom of the chamber. The front gun has a low magnetic source while the other two are equipped with high magnetic source. All magnetron guns can be installed with DC or RF power supplies. Each gun is designed to incline 30 degree and face to the center of the substrate holder with a target-substrate distance about 10 cm. Targets with thickness of 0.125, 0.185 and 0.25 inch are able to be loaded in the system. The maximum RF power can be applied on magnetron gun is 150 W by an AJA RF generator and manual matching network. Rotation and Heating of the substrate holder is capable by using an AJA SHQ-15 temperature controller. The maximum substrate bias applied can be either 50 W RF or 1000 V DC power. Argon gas with a purity of 99.99% is controlled by a unit instruments mass low controller to meet the pressure requirement in the deposition. Both mechanical pump and cryo pump are performing simultaneously which can keep the chamber vacuum down to 1×10^{-8} Torr during the deposition. An automatic gate valve with MKS 146C PID controller manages the pressure precisely. All the magnetron guns and substrate holder were cooled circularly with a water chiller system to avoid heating damage to both guns and substrate holder. A photograph of the lab-built sputtering system (figure 3.2) and the inside of the sputtering chamber (figure 3.3) are shown as follow.

Figure 3.2 Lab-Built PVD reactive magnetron sputtering system in Surface and Nano Engineering Laboratory

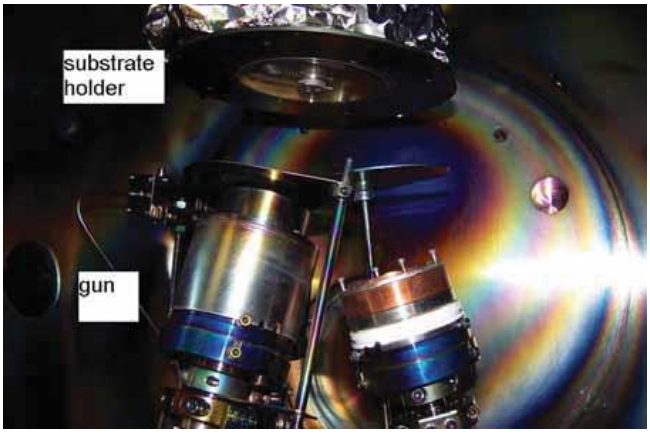

Figure 3.3 Inner view of the sputtering system showing two sputtering guns and the substrate holder

The basic operating procedure of the SaNEL sputtering system is described in the following. The sputtering system is firstly pumped down to below 20 mTorr with only mechanical pump running. This is preparation work before using cryo pump. After the pressure is ready, cryo pump begins to be used to achieve base vacuum in the range of

10^{-7} Torr. This pressure can be measured by an ion gauge and displayed on its digital readout. After an appropriate base pressure is reached, gas started to be flown into the chamber with controlled flow rate. The working pressure can be then measured and adjusted by a Baratron pressure gauge. With the selected power applied, system is all set up ready for plasma generation.

3.1.2 Sputtering Targets

99.9% purity 2 inch diameter LMO, $La_{0.67}Sr_{0.33}MnO_3$ and SMO targets with 0.25 thickness purchased from Kurt J. Lesker Co. were utilized for deposition on 10 mm x 10 mm (001) LAO and MgO single crystal substrates. All three ceramic targets were bonded with copper plate via indium bonding preventing from possible cracking. In order to fabricate ECG LSMO thin films, it is necessary to investigate epitaxial growth conditions of pure LMO and LSMO thin films firstly. Based on the optimum deposit conditions, the ECG LSMO thin films were also deposit successfully. Furthermore, achieving epitaxial triple layers LMO/LSMO/SMO systems with sandwich structure were attempted which could be designed for spintronic devices for application. Three different deposition conditions and procedures are included in this research which will be introduced in their individual section.

3.2 Thin Film Characterization Techniques

Complementary characterization techniques were performed to study the microstructures of as-deposit thin films. The crystalline and epitaxy of all as-deposited samples were characterized by XRD. HRTEM equipped with Energy-dispersive X-ray spectroscopy (EDS) provides detailed information regarding substructure, phases and composition present at higher resolution. Survey and High resolution XPS was performed to analyze surface composition and chemical states within the films. The surface morphology and thickness were probed by AFM.

3.2.1 X-ray Diffraction

The structure and crystalline orientation of the films were studied using Bruker D8 advance x-ray diffractometer with a Cu Kα radiation source and a wavelength of 1.54 Å. The acceleration voltage and filament current were set at 40 kV and 40 mA, respectively. Various scans, such as θ-2θ scan, detector scan with low angle and pole figure scan.

For symmetric θ-2θ scan, a small step size of 0.01° and a high dwell time of 1 second were utilized to obtain high resolution patterns. After running several times with auto-repeat option, the noise is highly minimized in the final data. Detector scan with low incident angle x-ray diffraction analysis with varies of incident angles were performed in order to further characterize the graded structure of the ECG LSMO thin film. Only the detector rotated from 20° to 24° in each scan while the incident beam was locked at a certain angle. The incident beam angle was then increased from 10.2° to 11.5° by 0.1°

shown in figure 3.4. The very small increment angle could help to find out the subtle changes of lattice parameter. Preferred orientation can be examined based on pole figure analysis, obtained at a fixed scattering angle and consisted of 360° in-plane rotation around the center of the film at different tilt angle (from 0° to 70°).

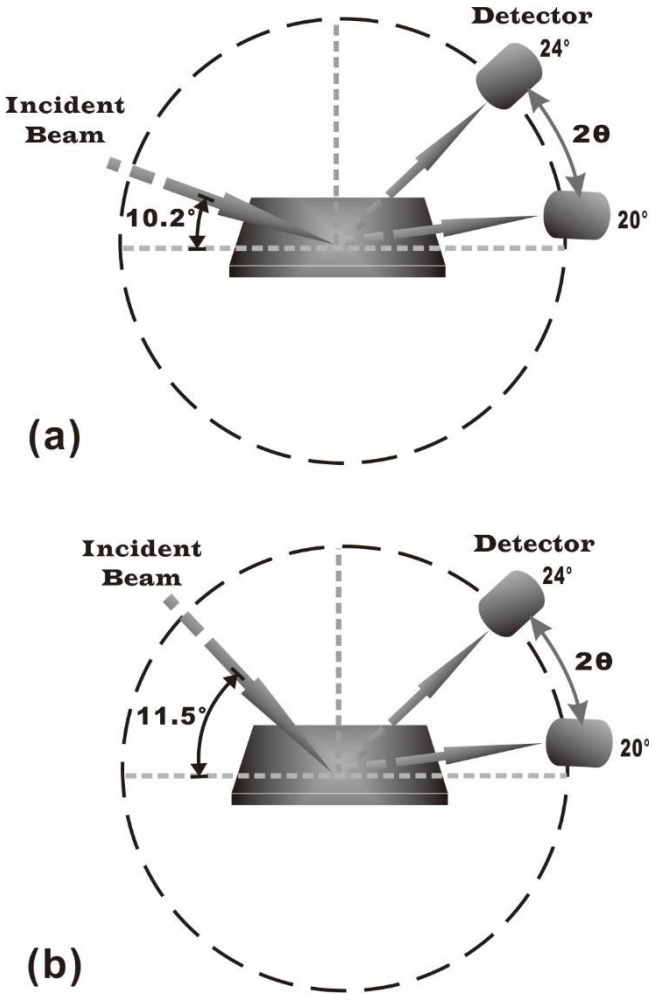

Figure 3.4 Schematic of detector scan low angle XRD with the incident angle from (a) 10.2° to (b) 11.5°

3.2.2 Atomic Force Microscopy

The surface roughness and morphology of the as-deposit thin films were probed by AFM using an Agilent Technologies 5500 in non-contact mode. An acoustic AC tip was installed to provide higher resolution images. The electrical properties of the pure LSMO epitaxial thin films were also studied in EFM mode.

EFM mode was performed to obtain the polarization domains of the films by applied an external electric field between the tip and the sample surface. This set of measurements was carried out in contact-EFM mode with NSC36/Ti-Pt conductive cantilever using a Park systems' XE 70 AFM. A 20nN initial set point was set up as the contact force between tip and surface by applying a 4 V AC signal at 17.5 kHz using SR830 DSP lock-in amplifier. A parallel electric field was applied in connection with both ends of the sample surface using silver paste. The information of local phases/domains polarization condition was obtained from EFM results under the external electric filed.

3.2.3 X-ray Photoelectron Spectroscopy

XPS surface analysis was performed with a Perkin-Elmer spectrometer using an Al Kα monochromatic X-ray source (1484.6 eV). The pressure was maintained below 10^{-9} Torr. High resolution spectra for each element were obtained at 50 eV pass energy taken in increments of 0.2 eV with dwell times of 100 ms for at least 200 scans. The binding energy of each XPS peak was calibrated with the C 1s peak of energy 284.6 eV. The Shirley background correction was applied in the survey analysis and peak deconvolution

of high resolution spectra was conducted utilizing the CASA XPS software. The intensity ratio among La, Sr and Mn was calculated as

$$R_{1,2} = \frac{I_1/A_1}{I_2/A_2} \quad \text{Eq.3.1}$$

where $R_{1,2}$ is the relative ratio between elements 1 and 2, I is the intensity of each element taken from the survey spectrum after background correction, and A is the relative sensitivity factor.

3.2.4 High Resolution Transmission Electron Microscopy

The microstructure and crystalline phases of the films were studied by HRTEM equipped with EDS recorded in a Hitachi H-9500 electron microscope. The system was operated at 300 kV with a point resolution of 0.18 nm. Cross-section TEM specimens were prepared by the procedure of mechanical grinding, polishing and dimpling followed by Ar-ion milling using a Gatan model 691 precise ion polishing system (PIPS). Low magnification images were obtained to overview the whole morphology through the thickness of the films. HRTEM images were used to understand the nanoscale structure of the films and the orientation from the lattice fringes. Electron diffraction patterns (EDP) were also involved to identify the crystal structure.

Chapter 4

Microstructure of Epitaxial $LaMnO_3$ and $La_{0.67}Sr_{0.33}MnO_3$ Thin Films on $LaAlO_3$ and MgO Substrates by RF Sputtering

4.1 Introduction

Manganite thin films, one of perovskite-type oxides, have attracted considerable attention since the discovery of CMR effect in these materials[67, 69, 75]. Among these materials, $LaMnO_3$, which is a Mott insulator, has been studied extensively due to exhibition of interesting physical properties after partially substituting La ions with divalent alkaline-earth metal ions such as Ca^{2+}, Sr^{2+}, or Ba^{2+}[57]. The Sr doped LMO was found to possess higher Curie temperature (370 K) than other types of doping groups, which enormously extends its application in design of spin-electronic devices. Thus, the perovskite-type LSMO thin film is considered as a great candidate in many new applications, such as data storage, low-cost magnetic sensors and other sensing devices[73].

Many techniques have been utilized in synthesis of LSMO thin films such as physical vapor deposition (PVD) including PLD and sputtering, chemical vapor deposition (CVD), atomic layer deposition (ALD), laser ablation and sol-gel coating. The PLD technique is conventionally used in fabrication of high quality LSMO thin films with c-axis preferred orientation and well controlled composition. However, the limitation of PLD is its inadequacy to synthesize thin films on a large area. Compared to PLD, magnetron

sputtering deposition would be more preferable from a practical point of view due to the compatible integration with other functional electric circuits or devices. In order to fabricate epitaxial composition gradient co-sputtered LSMO thin film, it is important and necessary to firstly fabricate composition uniform LMO and LSMO epitaxial thin films with individual target. In this chapter, the microstructures and surface morphologies of pure LMO and LSMO thin films on LAO and MgO substrates were characterized and discussed.

4.2 Fabrication of Epitaxial LMO and LSMO on LAO and MgO Substrates by Sputtering Deposition

Pure LMO and LSMO thin films were deposited on (001) LAO and MgO substrates using RF magnetron sputtering. Prior to film deposition the system was pumped down to a base vacuum of 5.0×10^{-8} Torr by a cryo pump. High purity Ar (99.999%) was flown into the chamber at a flow rate of 30 sccm and the chamber pressure was maintained at 10 mTorr during deposition. The substrates were cleaned in acetone for 10 minutes followed by alcohol to clean residual acetone and then dried up with compressed air. RF plasma was generated to clean the surface of the substrates using 30 W for twenty minutes. After substrate cleaning, LMO and LSMO thin films were synthesized by using RF power with heating the substrate. In order to obtain epitaxial structure, lower deposition rate and higher substrate temperature are recommended. Comparing with other experimental conditions, thin films with utilization of 30 W RF power and 750 ℃ substrate temperature exhibit the best quality. The specific deposition condition of each film was shown below.

Table 4-1 Deposition Conditions of LMO and LSMO Thin Films on LAO and MgO

Film	Substrate	Sputtering Pressure (mTorr)	Substrate Temperature ℃	RF Power (W)	Deposition time (hr)
LMO	MgO	10	750	30	2
LMO	LAO	10	750	30	3
LSMO	MgO	10	750	30	2
LSMO	LAO	10	750	30	4

4.3 Microstructure and Surface Morphology Study of Composition Uniformed LMO and LSMO Epitaxial Thin Films

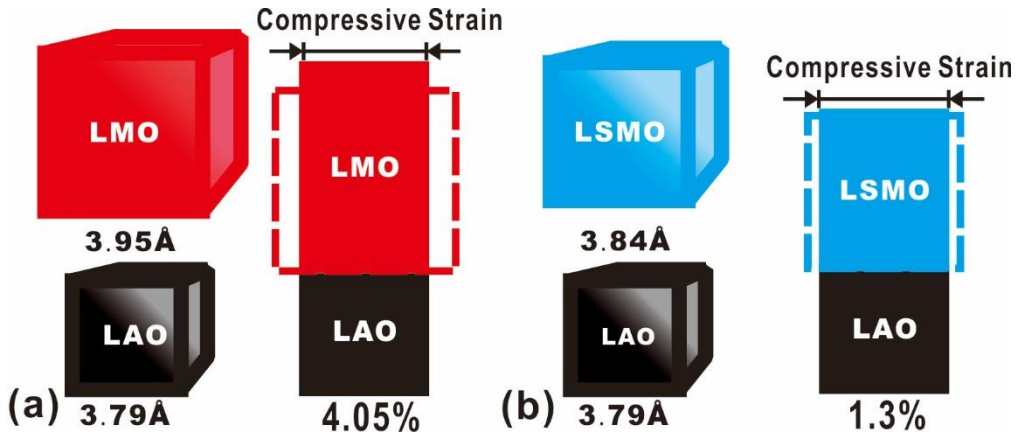

Figure 4.1 Schematic illustration of unit cell of (a) LMO and (b) LSMO on LAO substrate; the bulk value lattice parameters of each material and misfit between the films and substrate was also shown

In this section, the structure and phase purity of as-deposit films were characterized by symmetric θ-2θ scan using XRD. The surface roughness and morphology were characterized in non-contact mode by AFM. Cross-section and plan-view HRTEM images

and selected-area electron diffraction (SAED) patterns were also observed to further examine the nanostructure of the films.

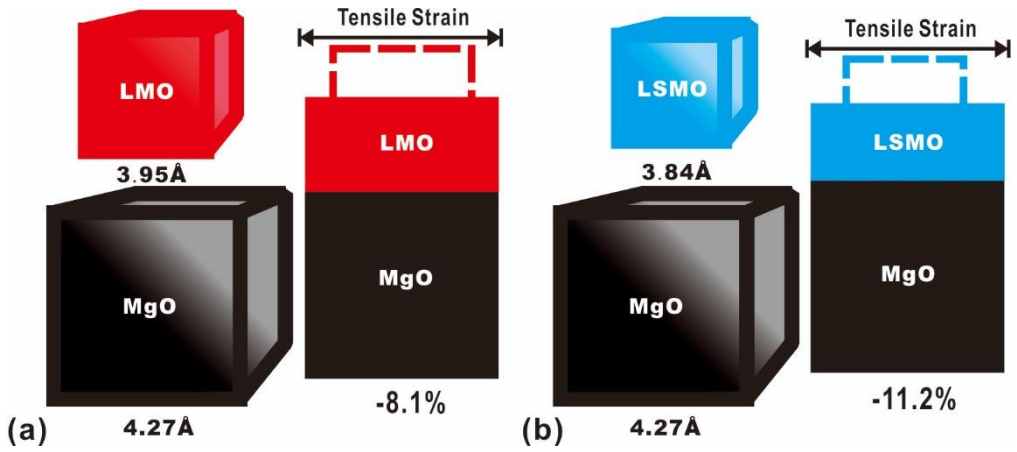

Figure 4.2 Schematic illustration of unit cell of (a) LMO and (b) LSMO on MgO substrate; the bulk value lattice parameters of each material and misfit between the films and substrate was also shown

The bulk LMO and LSMO normally can be considered as pseudo-cubic structure with $a = 3.95\ Å$ for LMO and $a = 3.84\ Å$ for $La_{0.67}Sr_{0.33}MO_3$ shown in figure 4.1. Thus, taken account for the bulk lattice constants of LAO and MgO substrates mentioned in table 4.1, the misfit *m* between films and substrates can be derived from by using equation

$$m = a_L - a_S/a_L \qquad \text{Eq.4.1}$$

where a_L and a_S are the layer and substrate unit cell parameters, respectively. It is found that the misfit is positive value for LAO substrate while a negative value for MgO substrate. This gives rise to the generation of in-plane compressive strain between films and LAO substrate and tensile strain for MgO substrate. Furthermore, based on eq.4.1, the misfit

value was calculated as 4.05% for LMO on LAO substrate, which is 1.3% for that of LSMO shown in figure 4.1. The misfit between LMO and MgO is -8.1% and -11.2% between LSMO and MgO shown in figure 4.2. Thus, it is expected that the microstructures and strain statuses of as-deposit thin films would be enormously difference due to generation of two different types of strains, which will help to investigate the strain-induced as well as the epitaxial growth mechanism in these manganite thin films.

4.3.1 Surface Morphologies and Microstructures study of Epitaxial LMO and LSMO Thin Films on LAO

The surface morphologies of as-deposit LMO and LSMO thin films on LAO substrates were characterized within a scan area of 0.5×0.5 μm^2 and shown in figure 4.1. Observed from 3D AFM images, both films exhibit a granular structure with a very fine size. The average roughness of LMO thin film shown in figure 4.3(a) is measured as about 0.99 nm while that of LSMO thin film in figure 4.3(b) is 0.68 nm, indicating very flat surfaces were obtained on both films. The lower roughness on LSMO thin film is mainly due to a lower deposition rate compared to that of LMO thin film.

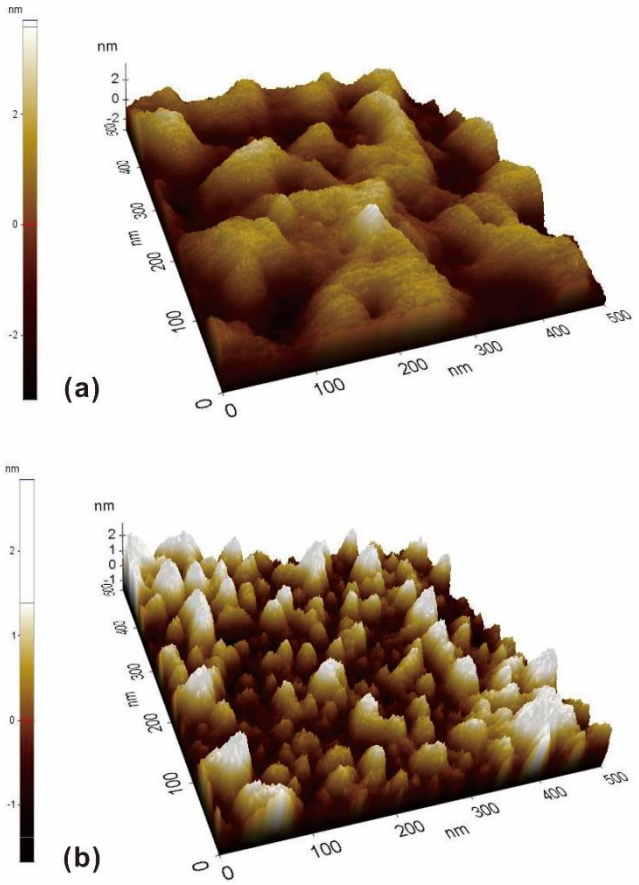

Figure 4.3 Non-contact AFM images of (a) LMO and (b) LSMO thin films deposited on LAO substrates

Furthermore, the microstructures of LMO and LSMO thin films on LAO substrates were performed and analyzed from XRD patterns shown in figure 4.4. Only (00l) peaks were observed indicating that cubic-on-cubic epitaxial structures were obtained in both thin films.

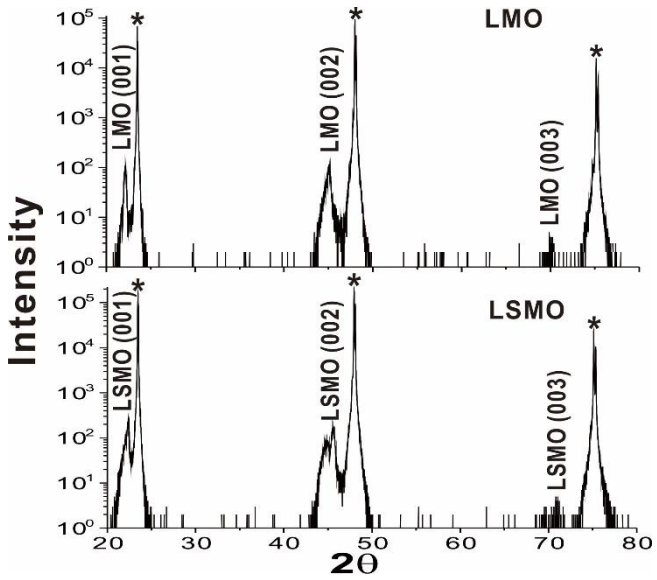

Figure 4.4 Comparison of θ-2θ XRD scans of LMO (up) and LSMO (down) thin films grown on (001) LAO substrates. The asterisks mark the substrate peaks

When zooming into the area of (001) LMO and LSMO reflections which the 2θ is between 21° to 25°, three different peaks were observed besides the substrate peaks shown in figure 4.5. There are two peaks around (001) position of LMO which located at 21.78° and 23.47°, respectively. The corresponding d-spacing of these two peaks were also calculated from Bragg equation, which are 4.07 Å and 4.01 Å. Assuming that the volume of unit cell is constant, the out-of-plane lattice parameter of fully strained epitaxial LMO thin film on LAO was calculated as 4.05 Å closed to the value of the first peak. Thus, this peak should be corresponded to a fully strained LMO layer. The peak with smaller d-spacing value should be assigned to a partially relaxed LMO layer. The formation of this layer may be attributed to generation of dislocations because the film thickness is above the critical thickness. Moreover, (001) LSMO reflection was found at 22.4° related to a

d-spacing of 3.97 Å. No secondary peak was observed in LSMO film indicating that the film is under fully strain. This value also coincides with the values reported in previous research.

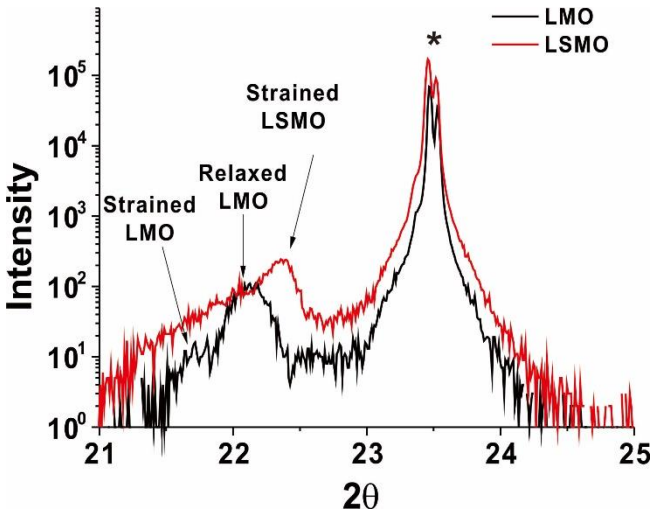

Figure 4.5 Zoom in of the (001) LMO and LSMO reflections in in figure 4.4. Arrows indicate the positions of the peaks corresponded to the (001) reflections of strained LMO, relaxed LMO and strained LSMO

4.3.2 X-ray Diffraction of Epitaxial LMO and LSMO Thin Films on MgO

The surface morphologies of as-deposit LMO and LSMO thin films on MgO substrates were characterized within a scan area of 1×1 μm^{2}shown in figure 4.6. Similar granular structures with the films on LAO substrates were also observed. The average roughness of LMO thin film (figure 4.6(a)) is about 0.865 nm while that of LSMO thin film is 0.595 nm shown in figure 4.6(b). The roughness difference between LMO and LSMO thin

films on MgO substrates are quite similar to the one on LAO substrates indicating the same reason in this case.

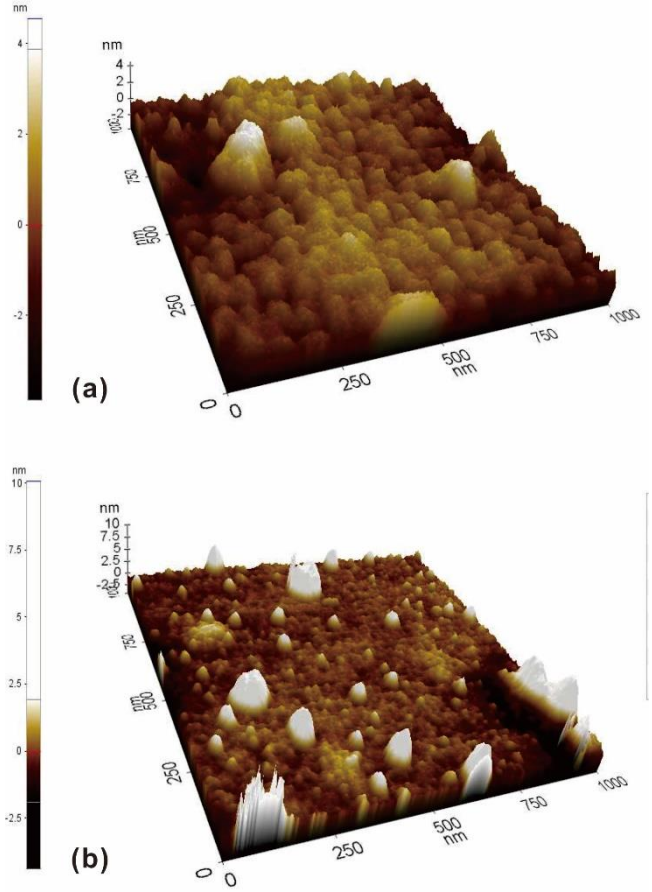

Figure 4.6 Non-contact AFM images of (a) LMO and (b) LSMO thin films deposited on MgO substrates

The microstructures of LMO and LSMO thin films on MgO substrates were also studied by θ-2θ XRD shown in figure 4.7. Only (00l) peaks observed in the patterns proves cubic-on-cubic epitaxial structures obtained in both films. If zooming into the area of (002) LMO and LSMO reflections in the range of 40° to 50°, two film peaks were identified and labeled as strained LMO and strained LSMO shown in figure 4.8. The LMO peak was

located at 45.61° with (002) d-spacing of 1.99 Å while the one calculated from LSMO pattern shows the peak position at 45.98° with (002) d-spacing value of 1.97 Å. No secondary peak observed indicates the absence of relaxation layer in both films. The smaller d-spacing value calculated from LSMO pattern should be contributed to Sr doping which causes the shrink of unit cell.

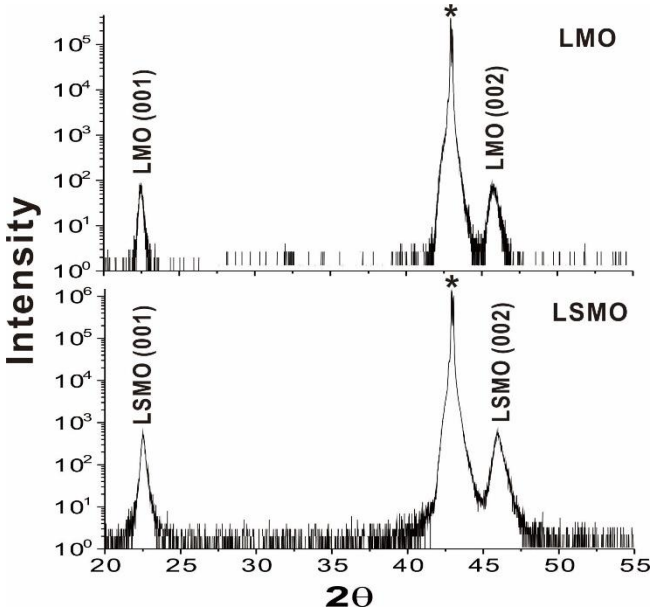

Figure 4.7 Comparison of θ-2θ XRD scans of LMO (up) and LSMO (down) thin films grown on (001) MgO substrates. The asterisks mark the (002) MgO substrate peaks

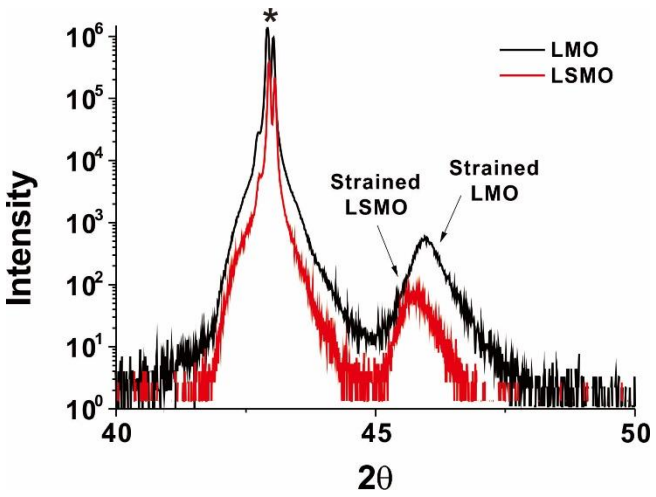

Figure 4.8 Zoom in of the (002) LMO and LSMO reflections in figure 4.7; Arrows indicate the position of the peaks corresponded to the (002) reflections of strained LMO and strained LSMO

4.3.3 HRTEM Study of LMO and LSMO Thin Films on LAO and MgO

To further study the nanostructure of as-deposit thin films, HRTEM analysis was involved and will be discussed in this section. Firstly, the low magnitude HRTEM images of LMO and LSMO thin films on LAO and MgO substrates were obtained and shown in figure 4.9. Thickness of each film was also measured from individual image. The deposition rates of LMO and LSMO targets under corresponding conditions on LAO and MgO substrates were then calculated and listed in table 4.2. It is found that the deposition rates of LMO and LSMO targets on MgO substrates are higher than those of on LAO substrates which is also coincidence with the previous published results. The thickness of LMO thin film on LAO is 72 nm which is much higher than the critical thickness (~30 nm). This further proves the previous explanation on the relaxed reflection peak in XRD pattern. All

the films exhibit sharp interfaces and smooth surfaces with respect to the substrates. However, wavy rough boundaries were formed at the interfaces in all films. It is possible that such rough interfaces were induced during the substrate surface clean process. As mentioned before, Ar ions plasma was used for cleaning the contamination on the substrate surface before deposition. This process could modify the substrate surface structure and introduce large number of steps, terraces and kinks on the surface which may be the derivation of nano-domains and boundaries in the films.

Table 4-2 Individual Thickness, Roughness and Deposition Rate of Each Film

Film	Substrate	Roughness(nm)	Thickness(nm)	Deposition Rate
LMO	MgO	0.865	62	0.5 nm/min
LMO	LAO	0.99	72	0.39 nm/min
LSMO	MgO	0.595	76	0.58 nm/min
LSMO	LAO	0.68	26	0.11 nm/min

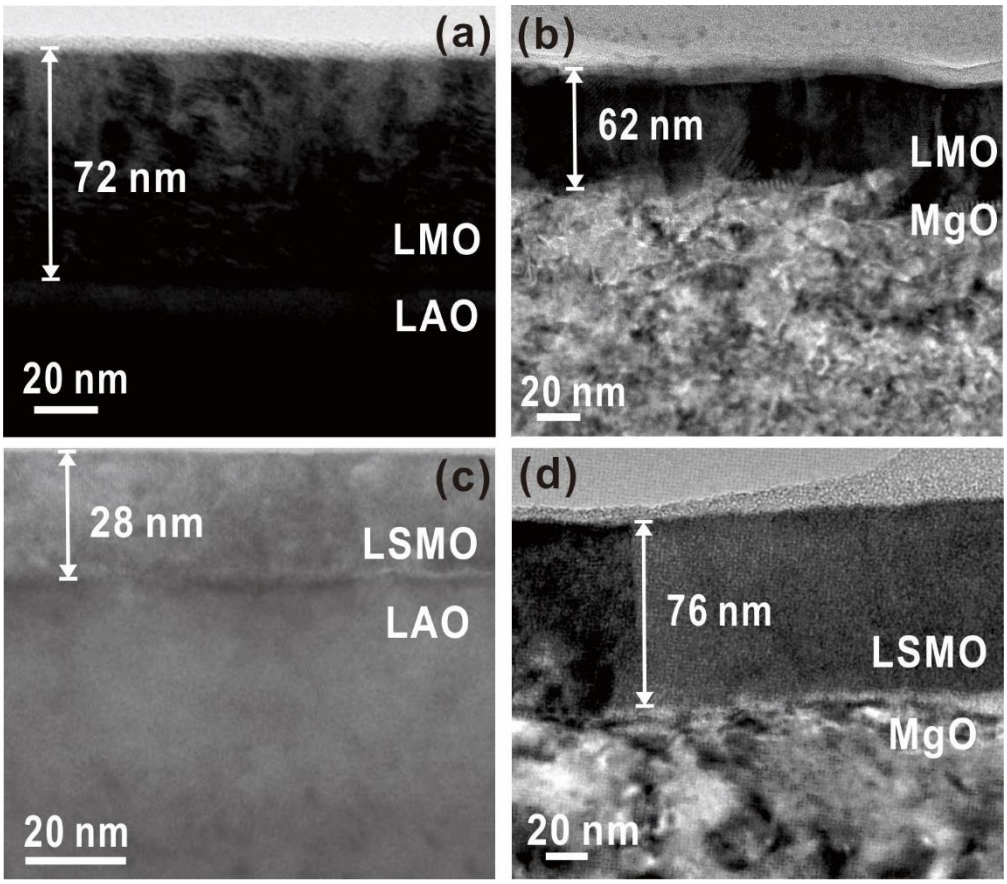

Figure 4.9 Low magnitude HRTEM images exhibiting the whole cross-section view of LMO thin films on (a) LAO and (b) MgO substrates, and LSMO thin films on (c) LAO and (d) MgO substrates. The thickness of individual film was also measured and shown in each image

The SAED patterns taken from the areas covering both thin films and substrates were shown in figure 4.10. It is found that all patterns display very clean single crystal diffraction patterns indicating good single crystal structures without forming any secondary phases or precipitates were obtained. The structure of LMO film on LAO was identified as pseudo-cubic from its SAED pattern (figure 4.10(a)). The in-plane and out-of-plane

mismatch between the film and substrate was also calculated from the pattern, which is about 1.48% and 3.95% respectively.

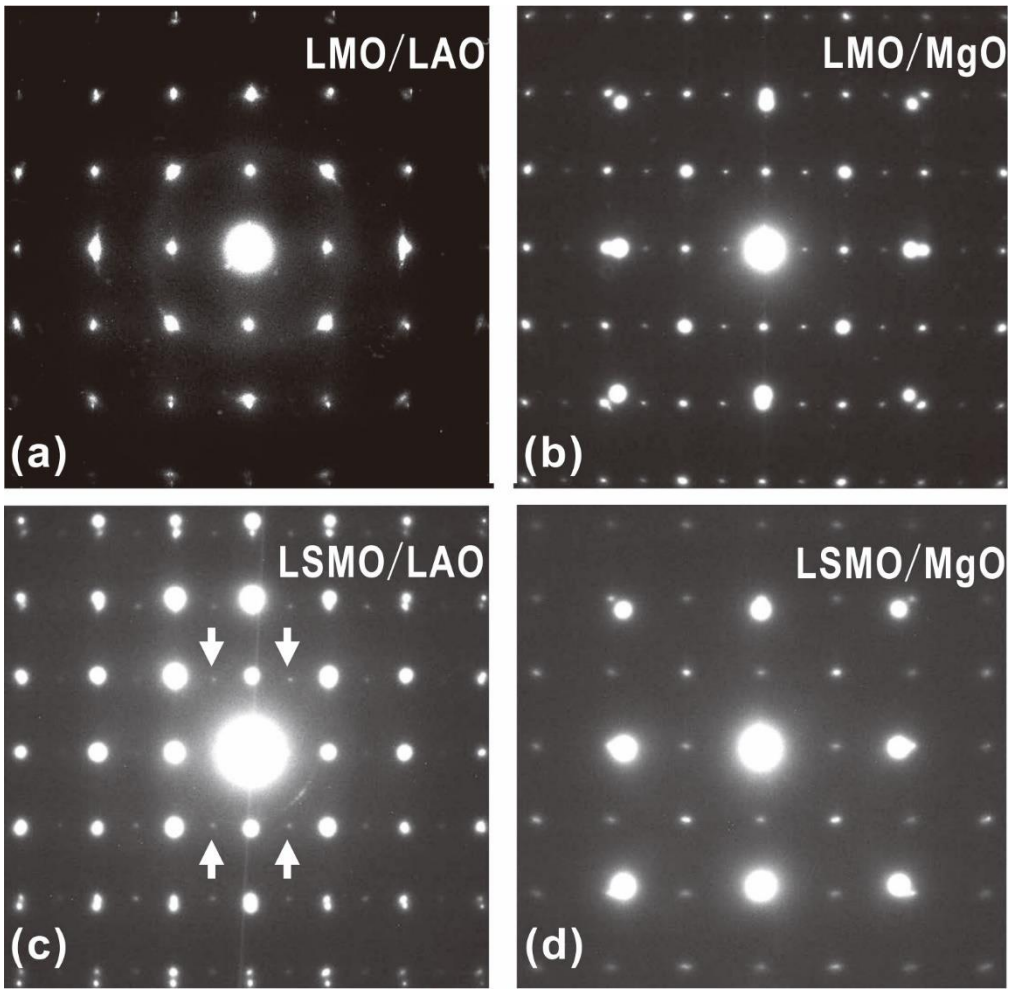

Figure 4.10 SAED patterns of cross-section LMO thin films on (a) LAO and (b) MgO substrates, LSMO thin films on (c) LAO and (b) MgO substrates taken from the interfaces between films and substrates. Diffraction spots marked by arrows in (c) are related to orthorhombic structure of LSMO thin film

The unequaled in-plane and out-of-plane misfit indicates formation of tetragonal unit cell. The observation of the weak reflections in the middle of adjacent diffraction spots as

the arrows marked in figure 4.10(c) indicates that an orthorhombic structure of epitaxial LSMO thin film on LAO substrate. The in-plane and out-of-plane mismatch are about 0.8% and 5.82% obtained in the pattern.

Figure 4.10(b) exhibits a SAED pattern of LMO epitaxial thin film on MgO substrate, which is taken along $[100]_{MgO}$. A similar structure with the one of LSMO on LAO, which is characterized as orthorhombic structure, was found with a 6.8% in-plane and -8.58% out-of-plane lattice mismatches. Moreover, a distorted cubic structure was identified for LSMO epitaxial thin film on MgO substrate in figure 4.10(d). The corresponding in-plane and out-of-plane lattice mismatch were calculated as -6.2% and -8.54% respectively.

High magnification cross-section HRTEM images of the interfaces of epitaxial LMO films on LAO and MgO substrates were obtained to further examine the microstructures shown in figure 4.11. The double-spaced lattice fringes with 8 Å lattice spacing shown in figure 4.11(a) further confirms the formation of the orthorhombic structure in LMO thin film on MgO substrate. Cross-section HRTEM image of LMO film on LAO substrate taken along the [100] direction of LAO was shown in figure 4.11 (b). The absence of double-spaced lattice fringes indicates that the orthorhombic structure was not induced. The lattice spacing measured from the vertical direction is about 2.4% larger than that of direction along the film plane. This is consistent with the results obtained from SAED patterns mentioned above.

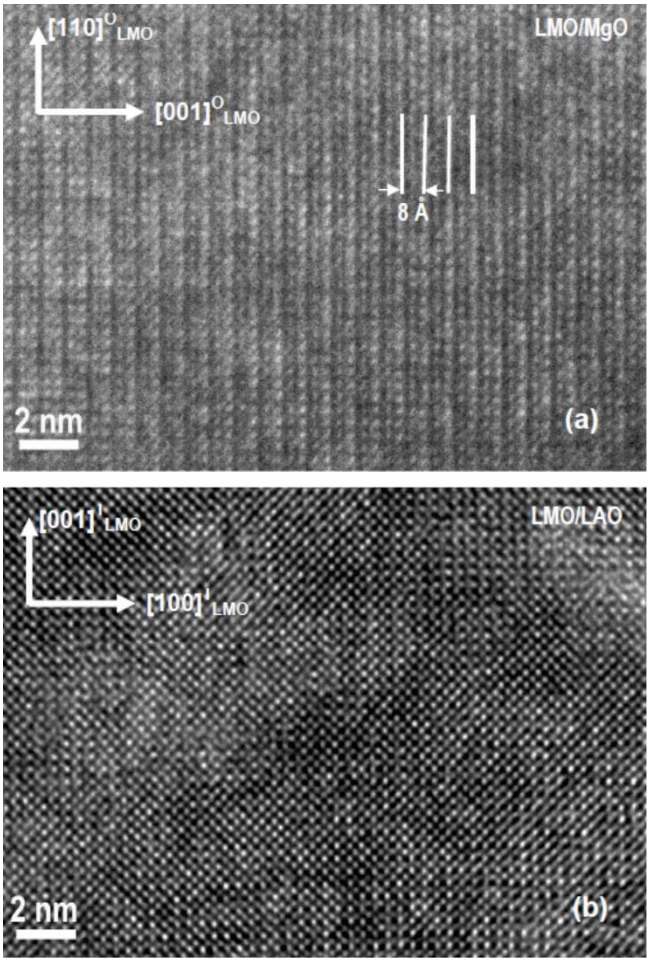

Figure 4.11 Cross-section HRTEM images of LMO thin films deposited on (a) MgO and (b) LAO substrates

Figure 4.12 shows the HRTEM image of the interfaces of LSMO films on (a) MgO and (b) LAO substrates. The dark regions shown figure 4.12(a) periodically distributed at the interface should be identified as the locations of the misfit dislocations. The average distance between dislocations is measured about 2.5 nm. The clean interface between LSMO film and LAO substrate shown in figure 4.12(b) indicates the absence of misfit dislocation at the interface. The lattice spacing of LSMO film along growth direction is

about 7.6% larger than that of along the lateral direction. This further confirms a highly distorted orthorhombic structure is formed in epitaxial LSMO thin film on LAO substrate.

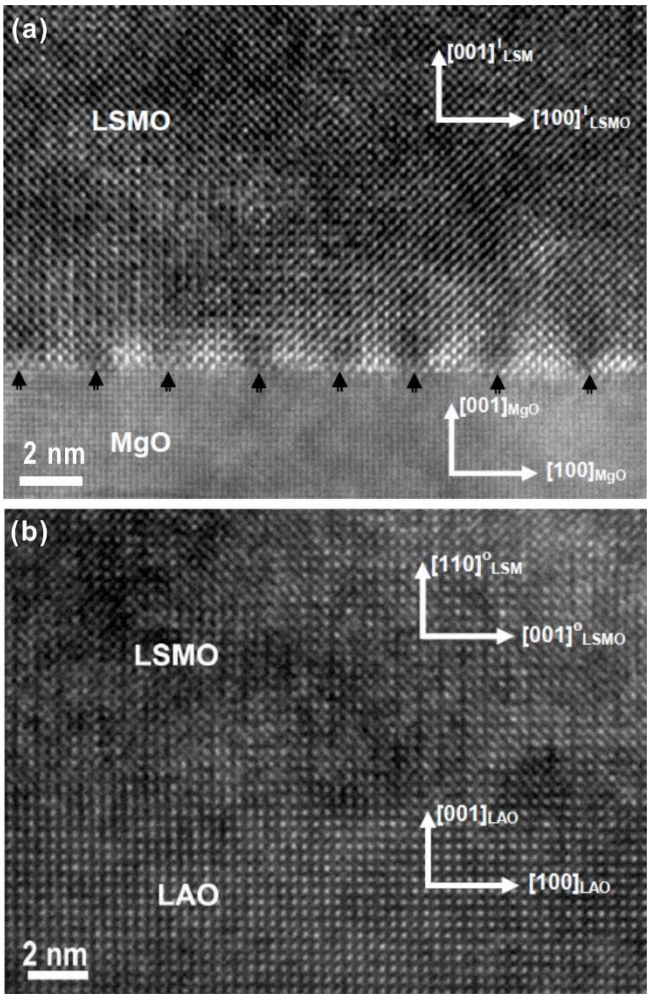

Figure 4.12 Cross-section HRTEM images of LSMO thin films deposited on (a) MgO and (b) LAO substrates

Chapter 5

Microstructure of RF Co-sputtered Strontium Doped Lanthanum Manganite Thin Films by Using $LaMnO_3$ and $La_{0.67}Sr_{0.33}MnO_3$ Targets

5.1 Introduction

Doped manganese oxides $R_{1-x}A_xMnO_3$, where R is a trivalent rare earth ion and A is a divalent alkali earth ion, have attracted significant attention due to their potential application in magnetic devices based on the observation of CMR. To exploit such magnetic devices, epitaxial heterostructures are required, where doped manganite electrodes grow on single crystal substrates. Thus, it is significant to clarify the effects induced by the substrates in the magnetic film. One of the most important effects is the dependence of the Curie temperature (T_c) on the strain in the film[118-120].

Among the doped manganites, $La_{0.67}Sr_{0.33}MnO_3$ has the highest T_C (370 K) even above room temperature, which makes it a great candidate for industrial applications. However, it is commonly found that the epitaxial strain between the substrate and film would highly depress T_C compared to its bulk counterpart[118-125]. Ahn and Millis *et al*. concluded that a biaxial strain could strengthen the Jahn-Teller distortion, further increase the splitting of the e_g electron band and thereby reinforce the tendency of the electrons to become localized[24] Thus, a process to relax the strain in doped manganite thin films would be the key to increasing of T_C.

Most of the previous studies concerned with the strain relaxation are focusing on the dependence of the strain on the film thickness. Maurice et al[125] and Ranno et al[126] reported on the thickness effects of $La_{0.67}Sr_{0.33}MnO_3$ on (001) $SrTiO_3$ by using x-ray diffraction (XRD). Two regimes were differentiated: below a critical thickness (t = 100 nm), there was a standard strained tetragonal regime while a more complicated regime, which was called "relaxed regime", was observed with a thickness above 100 nm. Up to three different lattice parameters were detected in the latter regime. They attributed this relaxation mechanism to a two-layer system: a fully strained layer and a slowly relaxing layer with an increasing c parameter. Jiang et al[25, 26] also observed a similar critical thickness of $La_{0.8}Sr_{0.2}MnO_3$ on (001) LAO with a columnar nanostructure evolving when the film thickness was above the critical thickness that exhibited unique electronic properties[27]. Malachias et al[127] investigated SiGe thin films and suggested that the strain could be further relaxed via compositional changes. Due to a rich phase diagram, thin films of LSMO may have various phases present with a c parameter variation. An insulator antiferromagnetic phase may be present at the interface with the substrate that gradually can turn into a metallic ferromagnetic phase on the surface with increasing Sr doping concentration. This may produce "new" materials with the properties that are not available in the individual component phases, which might also open up various new possibilities of designing new nanoscale structures with unusual cross coupled properties[27]. However, the most difficult challenges are mainly concerning on massive production and

characterization in nanoscale. Also, the relaxation mechanism needs to be further explored in manganite-based thin films.

In this chapter, there are three sections to systematically investigate the effect factors for fabrication of ECG LSMO thin films and the composition and microstructures of as-deposit thin films on MgO and LAO substrates. In the first section, characterizations of LSMO thin films on MgO substrates with different deposition conditions were involved. The next section is focusing on the characterization of ECG LSMO thin films on LAO substrates with different deposition conditions. In the last section, the ECG LSMO thin film was further analyzed and compared with the pure epitaxial LMO and LSMO thin films mentioned in previous chapter.

5.1.1 Fabrication of Co-sputtered LSMO Thin Films on MgO and LAO Substrates

Based on the deposition conditions above, co-sputtering was performed with both LMO and $La_{0.67}Sr_{0.33}MnO_3$ utilized on (001) LAO and MgO substrates. Both RF power supplies applied to the guns were controlled automatically and thus capable of providing a continuous variation of power and resulting deposition rate. This feature is very important in maintaining the epitaxy in composition gradient thin films. Abrupt power changes typically result in the nucleation of a new layer and thus damaging the epitaxial quality of the structure. The system was pumped down to a base vacuum of 5.0×10^{-8} Torr by a cryo pump.

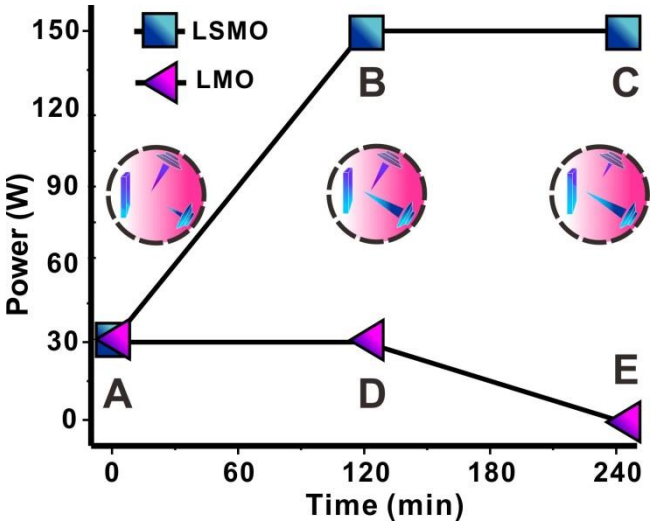

Figure 5.1 The schematic of the specific deposition procedure of ECG LSMO thin film. Step 1, 2 and 3 shows the variation of power ratio of LMO and LSMO targets during the deposition

A rather unique deposition approach was used for the fabrication of the compositionally gradient epitaxial films as shown in figure 5.1. High purity Ar (99.999%) was flown into the chamber at a flow rate of 30 sccm and the chamber pressure was maintained at 10 mTorr during deposition. Initially, the power applied to both targets was rapidly increased from 0 to 30 W in 10 seconds. The power to the LMO target was maintained at 30 W (line AD), while the power to the LSMO target kept constantly rising up to 150 W (line AB). Following that stage, the power to the LMO target was gradually lowered down to 0 (line DE) while keeping the power to the LSMO target at 150 W (line BC). The purpose of this experimental design is to obtain an epitaxial thin film with a gradual increase in the Sr doping along the film growth direction. At the same time, the

procedure insures that the surface composition of the film is similar to that of the LSMO target. The power-voltage dependence recorded during the first deposition stage. The near linear increasing voltage as the power raised demonstrated that the LSMO target was under an almost a linear increase in power during this stage. Three different deposition conditions were carried out at the following processing parameters: the first one was conducted at a substrate temperature of 750 ℃ for 1 hr in each step (AB, AD, BC and DE) for a total deposition time of 2 hr. The second set of experiment was conducted at 850 ℃ using the same deposition time as the first set. The last deposition was also carried out at 850 ℃ but doubling the deposition period in each step (2 hr in each step). Following deposition, all films were cooled down to room temperature at a rate of 20℃/min and oxygen was admitted in the chamber. Post deposition annealing was not performed to avoid any internal diffusion leading to possible alterations in the compositional uniformity.

Since the bulk value of the lattice parameter of LSMO and LMO are 3.84 Å and 3.95 Å respectively, which is larger than that of LAO pseudo cubic unit cell (3.79 Å), this gives rise to the generation of in-plane compressive strain and out-of-plane tensile strain in the film. The deposition rates of individual LMO and LSMO on LAO under 30W RF power calculated from the previous study are 0.39 nm/min and 0.11 nm/min, respectively. Thus, it is expected that a LMO-rich part with a very large strain at the bottom of the ECG LSMO film and a LSMO-rich part with a partially released strain on the surface area, which is due

to the lattice parameter reduced as the Sr doping gradually increased in the growth direction.

5.2 Microstructure Study of Co-sputtered LSMO Polycrystalline Thin Films on MgO

Three co-sputtered LSMO thin films were synthesized by different depositions which already detailed described in chapter 3. S1, S2 and S3 were defined as the samples deposited on 750 ℃, 850℃ and 850 ℃ with longer deposition time respectively in this section. X-ray Microstructure and orientation of as-deposit thin films were characterized by symmetric θ-2θ XRD scan, low angle XRD scan and pole figures. HRTEM images and EDPs were also involved on S3 to further investigate the nanostructure and phase.

5.2.1 Composition and Chemical States of Co-sputtered LSMO Thin Films by X-ray Photoelectron Spectroscopy

Figure 5.2 Shows a XPS survey spectrum of the as-deposited LSMO thin film on MgO which exhibits mainly La, Mn, Sr, O and C peaks. The binding energy of this spectrum was calibrated by C 1*s* peak with 284.6 eV. The binding energies of La $3d_{5/2}$ and $3d_{3/2}$ are located at 839.1 eV and 834.6 eV, while that of Mn $2p_{1/2}$ and Mn $2p_{3/2}$ are at 653 eV and 641.8 eV, respectively. The doping Sr was also split into Sr $3d_{5/2}$ and Sr $3d_{3/2}$, which are at 132.8 eV and 134.6 eV. The binding energy of O *1s* is 530.4 eV. The quantitative analysis shows that the as-deposit LSMO film has the atomic ratio La: Sr: Mn in the film with about1.04: 0.23: 1. The oxygen is a little higher than the stoichiometric LSMO bulk due to the surface contaminants from the environment. The lower Sr composition compared to

stoichiometric LSMO target should be contributed to sputtering preference which is normally happened in sputtering deposition.

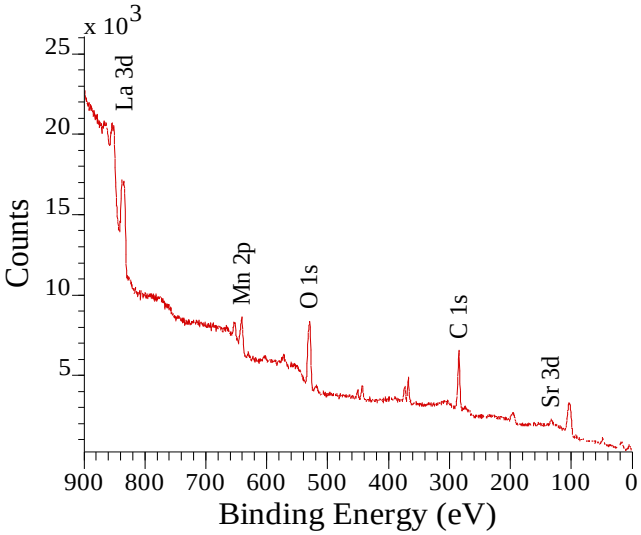

Figure 5.2 XPS survey spectrum of LSMO thin film deposited on MgO substrate

The O *1s* core level high resolution XPS spectrum of S3 is shown in Figure 5.3(a). The spectrum is deconvoluted by two peaks at binding energies of 529.8 eV and 532.6 eV. The main peak which is around 529.8 is attributed to O^{2-} ion of the metal oxide[128]. The second peak around 532.6 eV is hard to identify. A peak for O at this position has been observed previously. Most of the past reports treat this peak as highly thermo stable OH_{bulk} group or chemical or physical absorption of H_2O on the sample surface[129, 130]. Liang and Weng have attributed this peak to surface oxygen associated with La, which will be further confirmed by Mn *2p* and La *3d* high resolution emission[131, 132]. Therefore, it is reasonable to assume that this peak is a combination of contamination, OH^- and the La oxide.

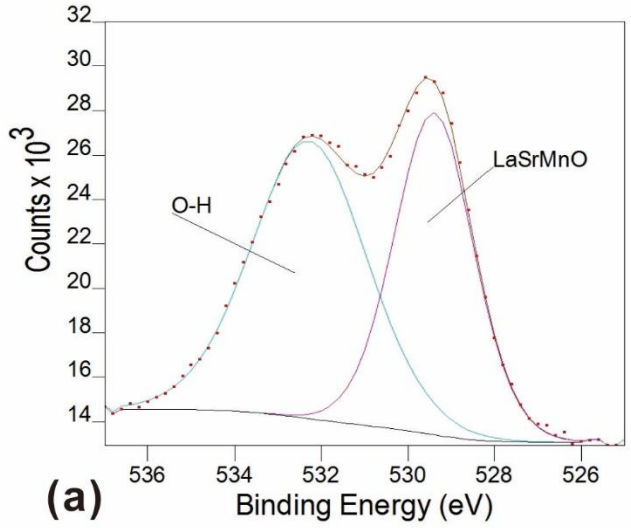

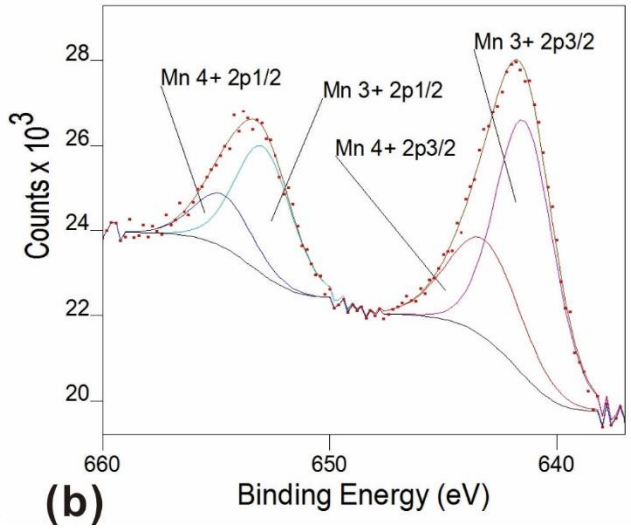

O

Figure 5.3 High resolution spectrums for (a) O *1s*, (b) Mn *2p* core level of S3

The Mn*2p* core level high resolution XPS spectrum of S3 mainly consists of two peaks which correspond to the $2p_{1/2}$ and $2p_{3/2}$ spin orbital doublet peaks located at 653 eV and 641.8 eV, respectively. The two contributions are separated by 11.2 eV which is in agreement with previous reports[132]. The peaks are well fitted by two components assigned to Mn^{3+} and Mn^{4+} shown in Figure 5.3(b)[132-134]. As Sr is doped into LMO, Mn^{3+} turns to be

Mn^{4+} in order to keep the charge neutrality. The Mn^{3+}: Mn^{4+} intensity ratio was calculated from the spectra which is about 67.85%:32.15% close to the LSMO target ratio of 0.67: 0.33. This actually demonstrates that the surface stoichiometry is similar with that of the LSMO bulk target. The cation ratio among La, Sr and Mn was 1.04/0.23/1 which was also obtained from La *3d*, Sr *3d* and Mn *2p* after background correction in the survey spectra according to Eq. (2). This result supports the previous argument that the surface is La rich due to the formation of La oxide.

The La *3d* core level high resolution spectrum shows two contributions $3d_{5/2}$ and $3d_{3/2}$ due to the spin-orbit interaction, Fig. 6(a). The splitting energy is 16.8 eV which agrees with that of La_2O_3. This suggests that the surface La ions and other La ions in the manganite are all in the trivalent state[135-137]. Each peak is further split into two components due to an electron hopping from oxygen ligand to the La4f which is empty initially[138]. The two components correspond to the main line ascribed as $3d^9 4f^0$ with binding energy at 834.6 eV and a satellite line ascribed to a charge transfer $3d^9 4f^1 L$ with binding energy at 839.1 eV, where L represents the hole in ligand site[135]. A third component was also found and was well fitted and should be attributed to a surface La rich oxide. This also agrees well with the results from O *1s*, Mn *2p* and survey spectrum, and further confirms the existence of La oxide on the surface. The Sr *3d* core level high resolution XPS spectrum, Figure 6(b), is deconvoluted as a doublet with binding energy at 132.8 eV and 134.6 eV corresponding to Sr $3d_{5/2}$ and Sr $3d_{3/2}$, respectively. The present results are in agreement

with the previous reports of similar compounds, which considered Sr ion in the divalent state[132].

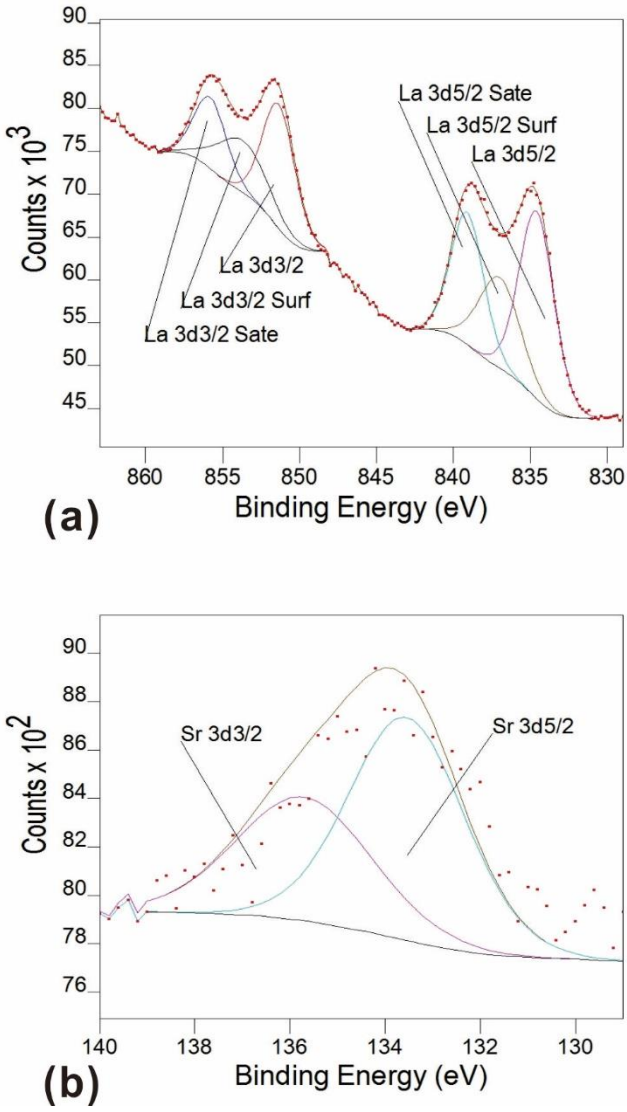

Figure 5.4 High resolution spectrums for (a) La *3d*, (b) Sr *3d* core level of S3

5.2.2 X-ray Diffraction Study of Polycrystalline LSMO Thin Film on MgO Substrate

Microstructures of as-deposited LSMO thin films on MgO were characterized by θ-2θ X-ray diffraction shown in figure 5.5. The main peaks labeled were corresponded to (002)

reflections from MgO. The peaks labeled by an asterisk result from CuK_{β} and the one labeled by square derived from parasite tungsten line (WL) (From Structural properties of epitaxial $La_{0.67}Sr_{0.33}MnO_3$ films with increased temperature of metal–insulator transition grown on MgO substrates). Besides the substrate peaks, (104) (002) and (003) reflections were found in all three films, indicating formation of polycrystalline structures. The absence of (001) and (110) reflections in S1 and (001) reflection in S2 were observed compared to the diffraction pattern of S3. The different diffraction results may be contributed to the difference among their deposition parameters. As the substrate temperature increased from 750 ℃ to 850 ℃, (110) reflection appeared as well as a reduction of (104) reflection. Moreover, with the deceasing of the power rate from 2 W/min to 1 W/min, a (001) reflection and a further lower intensity of (104) reflection were identified in S3. In order to check the preferred orientation of the crystalline, the results of (001) pole figure analysis of each film was obtained in figure 5.6. Randomly distributed patterns were observed indicating that there is other orientation besides [001] direction existed in the films.

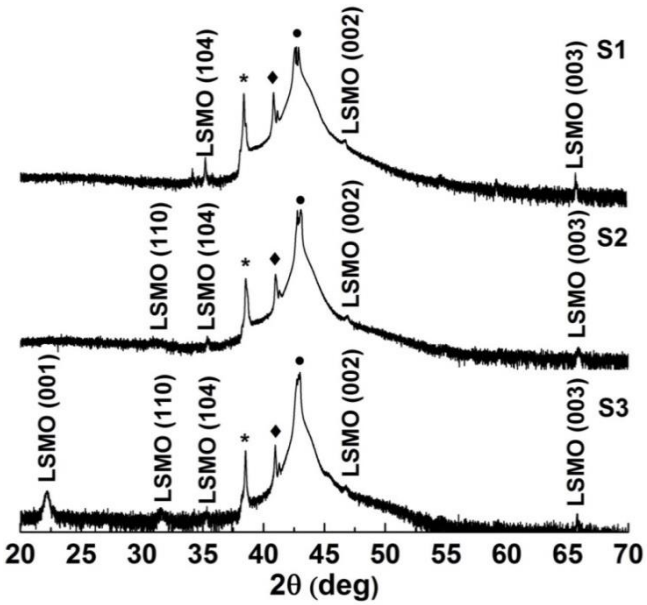

Figure 5.5 Comparison of θ-2θ XRD scans of the three composition gradient LSMO thin films grown on (001) MgO substrates. ●-MgO (002), ⁎-CuK_β (MgO (002)), ♦-WL (MgO (002))

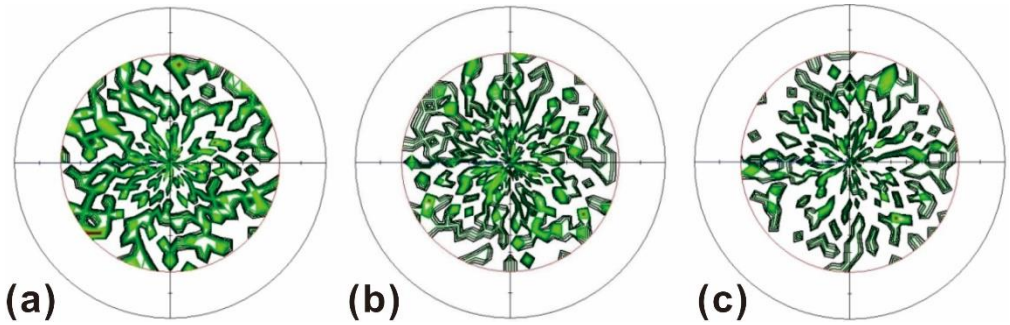

Figure 5.6 (001) LSMO pole figure reflections of films (a) S1, (b) S2 and (c) S3 deposited on MgO

To further understanding the peak information of films, low angle x-ray diffraction patterns of S3 on MgO were obtained shown in figure 5.7. The glancing angles were much larger (from 5° to 12°) compared to the traditional ones (usually below 3°). Weak

diffraction peak of the substrate demonstrates that most of the incident beam irradiated on the film. No substrate peak was observed until the incident angle above 10°, indicating that the film has a large x-ray absorption coefficient factor. The main peaks obtained were identified as (001) and (110) of orthorhombic LSMO structure. The out-of-plane lattice parameter was measured from (001) reflection in the pattern which equals to 3.97 Å. Meanwhile, the only thing varied as the incident angles increased in the pattern was the peak intensity, indicating that no vertical lattice parameter changed due to a different Sr doping concentration.

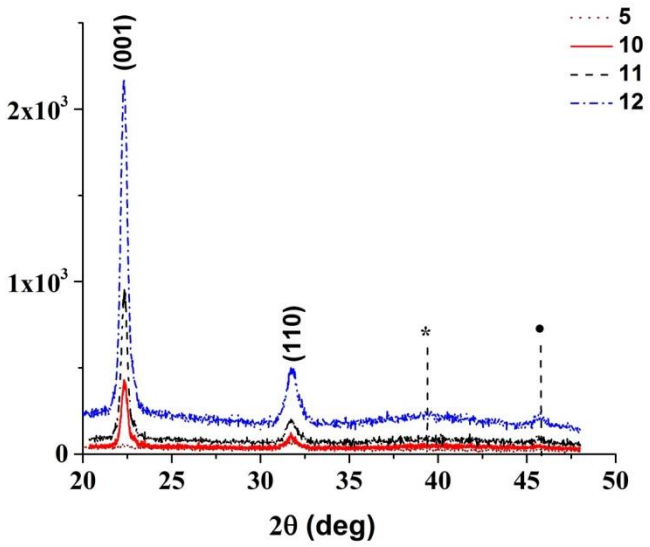

Figure 5.7 Low angle diffraction patterns of S3 on MgO with different incident angles; ●-MgO (002), ⋆-CuK_{β} (MgO (002))

5.2.3 High-resolution TEM Study of Polycrystalline LSMO Thin Film on MgO Substrate

HRTEM was used to analyze the films at the nanoscale and obtain further understanding of the nanocrystalline morphology and structure of the S3 on MgO

substrate shown in figure 5.8. The as-deposit film exhibits a very flat surface and a sharp interface with respect to MgO substrate. Compared to the interfaces of pure LMO and LSMO thin films mentioned in chapter 3, the interface is much smoother indicating that the rough interfaces in uniformed LMO and LSMO thin films are caused by plasma assisted substrate surface cleaning process. The thickness of the film was measured as 23.6 nm from HRTEM images.

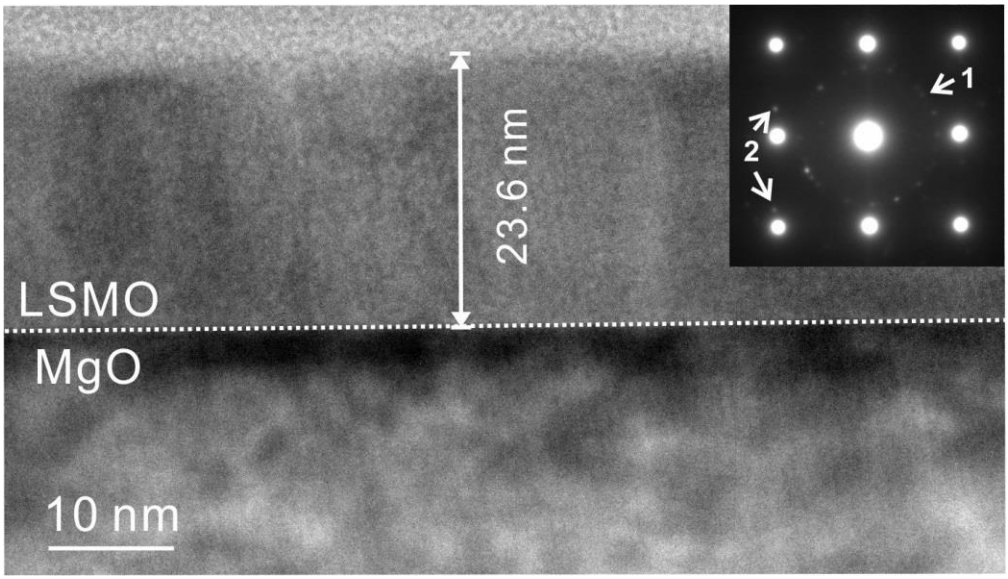

Figure 5.8 HRTEM image under low magnification of S3 on MgO substrate; inset is SAED taken along $[100]_{MgO}$ covering both film and substrate. The ring pattern labeled as 1 corresponds to (110) in orthorhombic structure; Diffraction dots labeled as 2 related to epitaxial pseudo-cubic structure

Selected area electronic diffraction taken along $[100]_{MgO}$ covering both film and substrate was obtained. A complex diffraction pattern was observed, which includes a ring pattern labeled as 1 and diffraction spots adjacent to the diffraction spots from MgO

substrate labeled as 2. The ring pattern was identified as (110) from pseudo-cubic structure while the diffraction spots are corresponded to epitaxial pseudo-cubic structure.

The column structures were observed in the image with about 17 nm diameter in each column shown in figure 5.9. Similar structures were also observed in other places of the film. It suggested that the spontaneous formation of such self-organized column nanostructures can be considered as following a type of Volmer-Weber growth mode. The reason of this growth mode may be contributed to a relative low substrate temperature so that the energy gained by the attaching atoms was not sufficient to hop into equilibrium position and thus islands were tended to be formed on the interface.

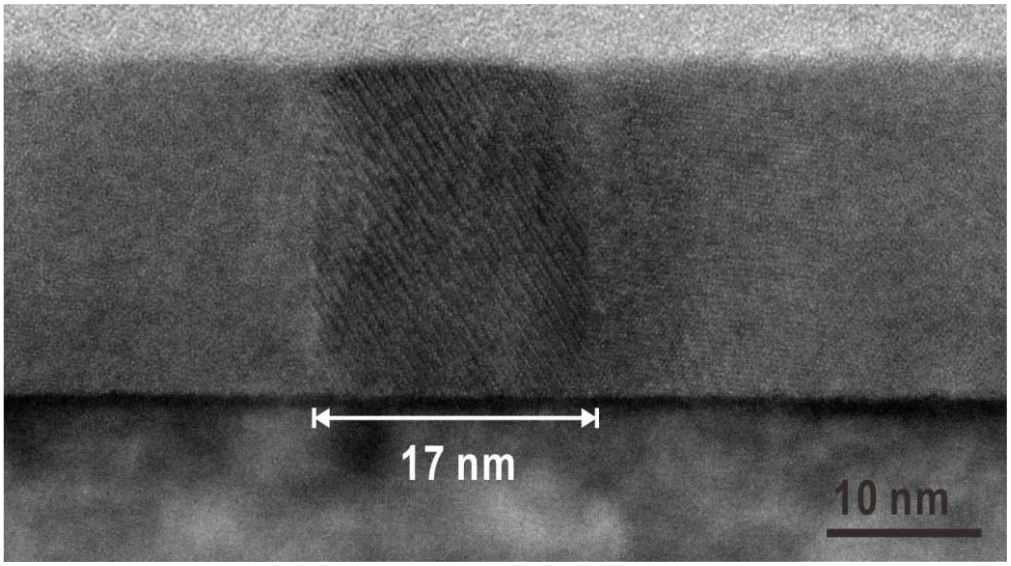

Figure 5.9 Column structure with about 17 nm diameter domain in S3

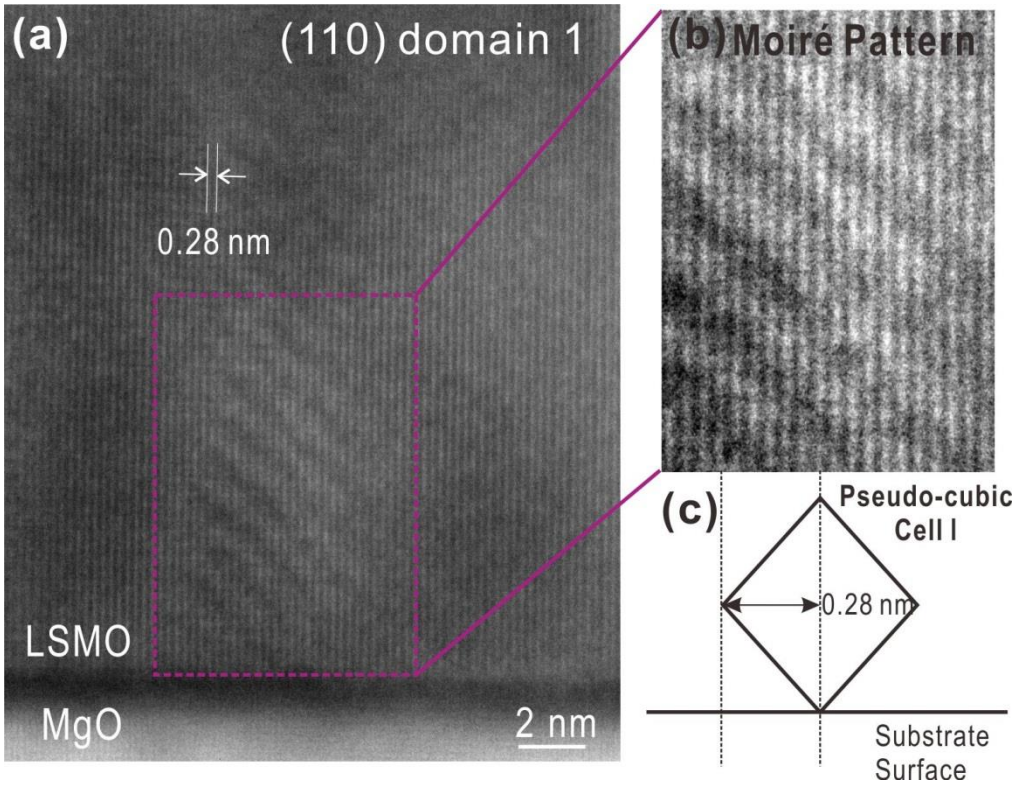

Figure 5.10 HRTEN cross-section images under high magnification of S3 on MgO showing (a) (110) domain with orthorhombic structure; (b) details of the squared area in (a) showing the (110) lattice fringes with clear Moiré pattern; (c) schematic picture showing pseudo-cubic unit cells in the column

To further investigate the nanostructure of columns with different orientations, high magnification HRTEM images were obtained. It is found that two different types of (110) domains with different structures shown in figure 5.10 and 5.11. The (110) domain with orthorhombic structure was shown in figure 5.10(a). The lattice fringe was measured with 0.28 nm which corresponds to (110) plane. It is observed that single phase exists in this column except a Moiré pattern appeared in part of the column shown in figure 5.10(b). The

Moiré pattern was attributed to multiple overlapped lattice fringes with different orientations. Schematic illustration of the distorted orthorhombic unit cell rotated about 45° with <110> of LSMO thin film perpendicular to the substrate surface shown in figure 5.10(c). The reason for the formation of this orthorhombic structure may be attributed to small amount of Sr doping into the film. It is reported when $0 < x < 0.2$ in $La_{1-x}Sr_xMnO_3$ thin film, the orthorhombic structure is preferred.

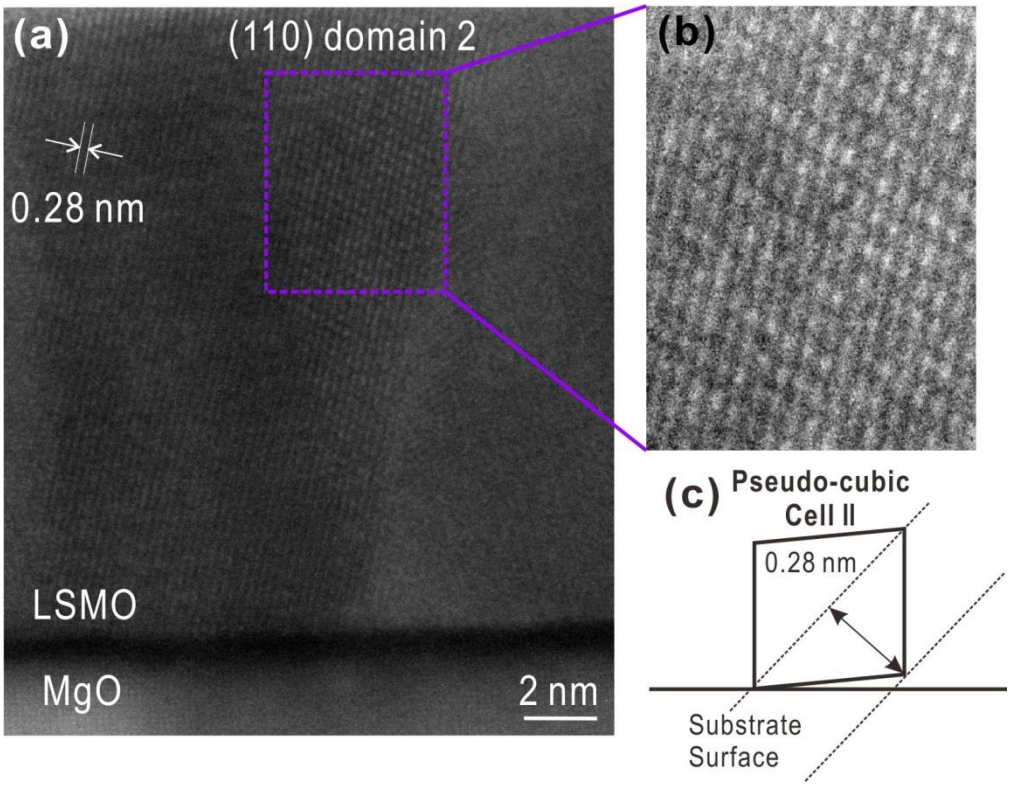

Figure 5.11 HRTEN cross-section images under high magnification of S3 on MgO showing (a) (110) domain with pseudo-cubic structure; (b) details of the squared area in (a) showing the (110) lattice fringes; (c) schematic picture showing pseudo-cubic unit cells

However, another type of column domain (110) orientation was also observed in the film shown in figure 5.11(a). The d-spacing of this (110) domain measured from lattice fringe was 0.28 nm, which equals to that of orthorhombic structure mentioned above. Schematic illustration of an alternative domain structure showing in figure 5.11(c) describes the tilted pseudo-cubic unit cell.

Figure 5.12 exhibits cross-section HRTEM image of two adjacent columnar domains with different orientations. It is found that a (001) domain (figure 5.12(b)) on the left shows a clear tilted pseudo-cubic structure epitaxially grown on the substrate. The lattice spacing was measured as 0.397 nm which is consistent with the XRD result. The enlarged area marked in (110) domain with a 0.28 nm lattice spacing was shown in figure 5.12(d). A clear boundary between two domains were observed and shown in figure 5.12(c).

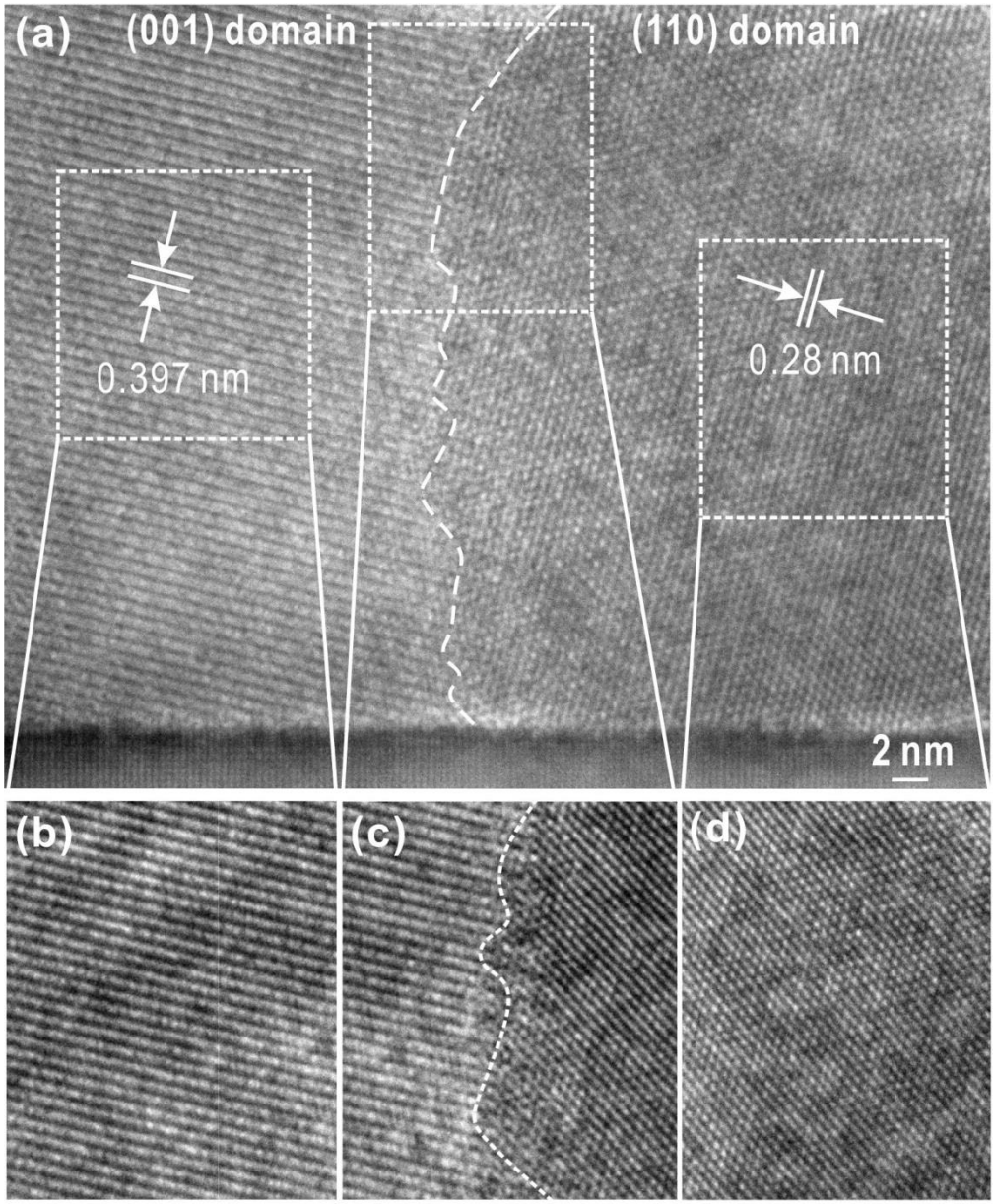

Figure 5.12 HRTEM image from a cross-section LSMO film showing two adjacent columnar domains with different orientations; (b), (c) and (d) enlarged images of the marked areas in (a)

5.3 Microstructure and Composition Characterization of Co-sputtered LSMO Thin Films on LAO with Different Conditions

In this section, a novel method to fabricate Sr-doped composition gradient epitaxial LSMO thin films was reported by RF magnetron sputtering. Biaxially strained epitaxial LSMO thin films were grown on (001) LAO substrates by following a co-sputtering procedure from LMO and $La_{0.67}Sr_{0.33}MnO_3$ targets. Three depositions were conducted by varying the substrate temperature (750℃ and 850℃) and controlling the relative deposition rate from the two targets by varying their power rate during sputtering. The thickness of the thin films was about 15 nm and 23 nm for the short and long duration deposition, respectively. The films were characterized by symmetric θ-2θ x-ray diffraction, pole figure analysis, atomic force microscopy and x-ray photoelectron spectroscopy.

5.3.1 Atomic Force Microscopy Study of Co-sputtered LSMO Thin Films

The surface morphology of the three films in a 5 μm ×5 μm scan area is shown in Figure 5.13. All films exhibited very smooth surfaces suggesting the absence of anisotropy of roughness in any particular direction. It is observed that the roughness of the surface topography decreased from about 0.696 nm (S1) to 0.138 nm (S3) indicating a lower roughness as the substrate temperature increased and the power rate decreased. The film thickness was found to be about 15 nm for S1, and S2 and 23 nm for S3.

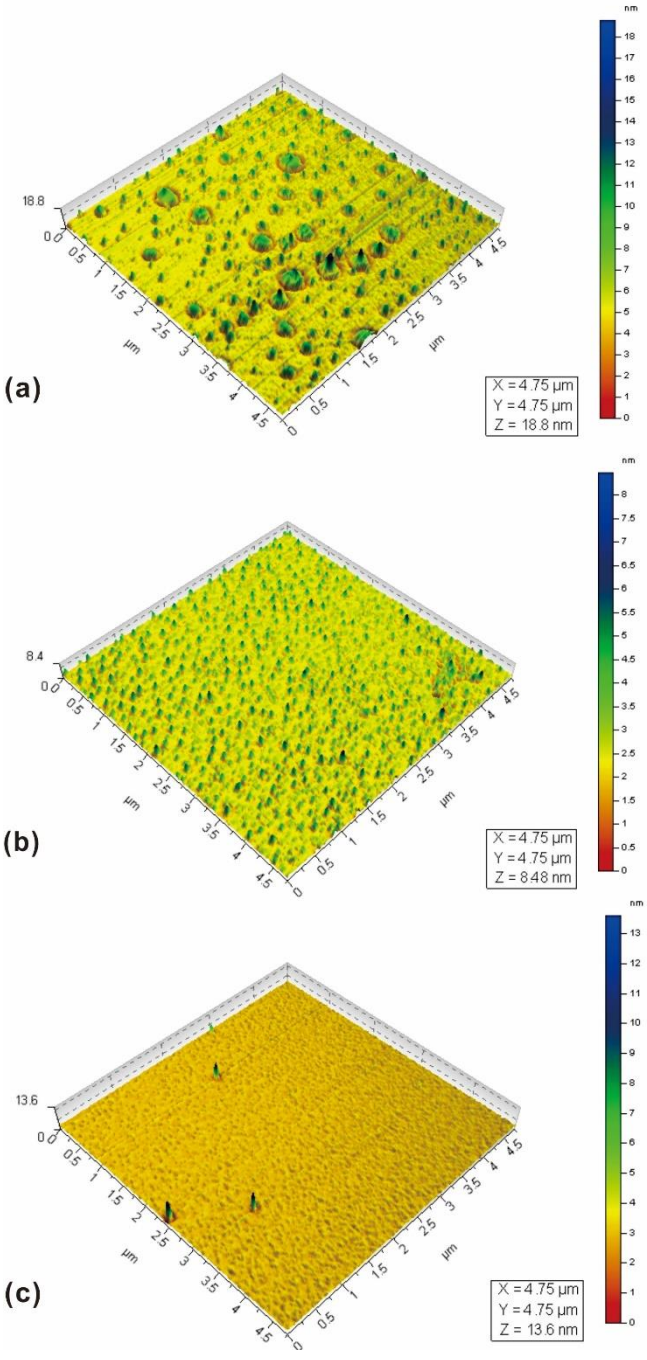

Figure 5.13 AFM results showing surface morphology of films (a) S1, (b) S2 and (c)

5.3.2 X-ray Diffraction Study on Co-sputtered LSMO Thin Films on LAO with Different Conditions

Figure 5.14(a) presents the θ-2θ XRD patterns of all three films. Only (00l) peaks were observed indicating that epitaxial LSMO thin films successfully grew on the (001) LAO substrates. The full width half maximum (FWHM) of the films peaks decreased (from S1 to S3), suggesting an improvement in the film quality. The (001) LSMO peaks for all three films are superimposed in Figure 5.14(b). Some novel features are observed. The intensity of the diffraction peaks increases significantly from S1 to S3. This indicates an improved crystallization due to higher substrate temperature and a lower power rate resulting in an extended residence time of atoms at the surface. It is interesting to note in the XRD pattern that the diffraction from film S3 is composed of a series of narrowly spaced peaks marked as P1, P2, P3 and P4. Actually each peak could be interpreted as a thin layer with different Sr content producing a changing in the lattice parameter.

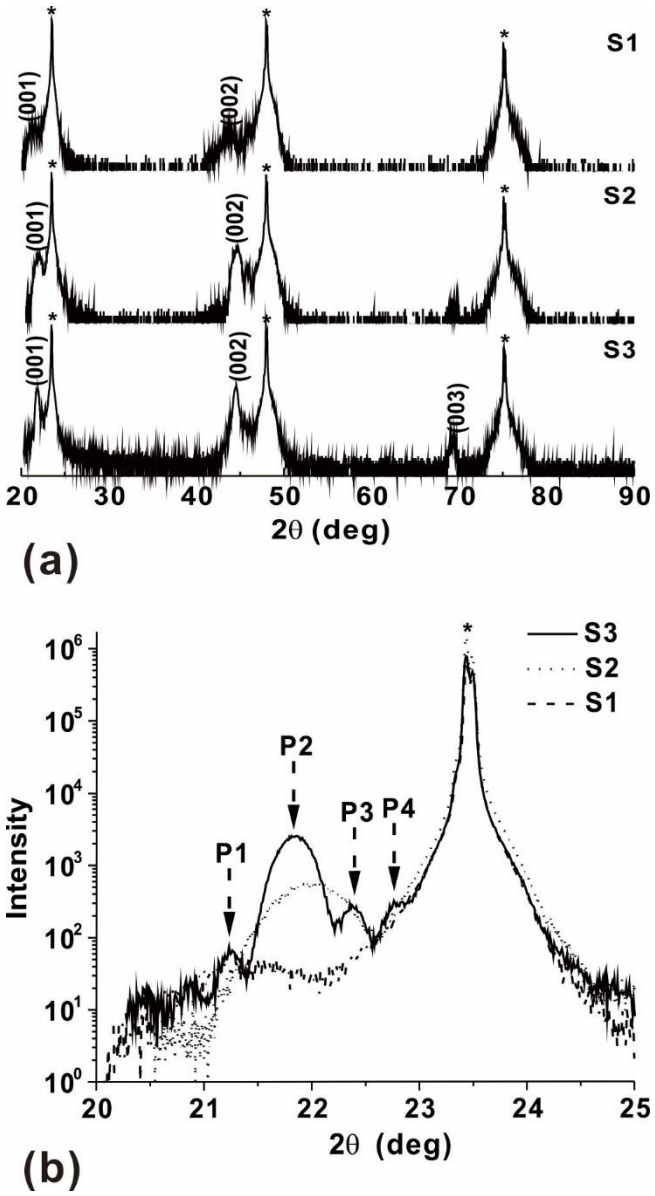

Figure 5.14 (a) Comparison of θ-2θ XRD scans of the three composition gradient LSMO thin films grown on (001) LAO substrates. The asterisks mark the substrate peaks. (b) Zoom in of the (001) LSMO peaks for all three films. Arrows indicate the positions of the peaks assigned to the (001) reflection of S3

The results of the (001) pole figure analysis from the three films are shown in Figure 5.15. Some dispersed diffractions are evident around the center (001) reflection of film S1 in Figure 5.15(a). The pole figure shows a weakly textured film indicative of dispersion in the out-of-plane orientation. Film S2 reveals a concentration of diffraction spots around the center indicating a (001) texture, Figure 5.15(b). However, a quite large spot area of the (001) reflection implies that even though the layer presents a (001) preferred orientation, some misorientation is present in some parts of the film due to strain in agreement with the θ-2θ XRD results. Figure 5.15(c) shows a very narrow rod-like region of the (001) reflection indicating a highly consistent orientation in film S3. The rod shape may derive from (001) plane distortion so that the reciprocal diffraction is elongated due to difference in the *c* parameter value. This particular feature is proved to be an evidence of that each layer in film S3 still maintains consistent orientation and excellent epitaxial quality in spite of the presence of different layers in the film.

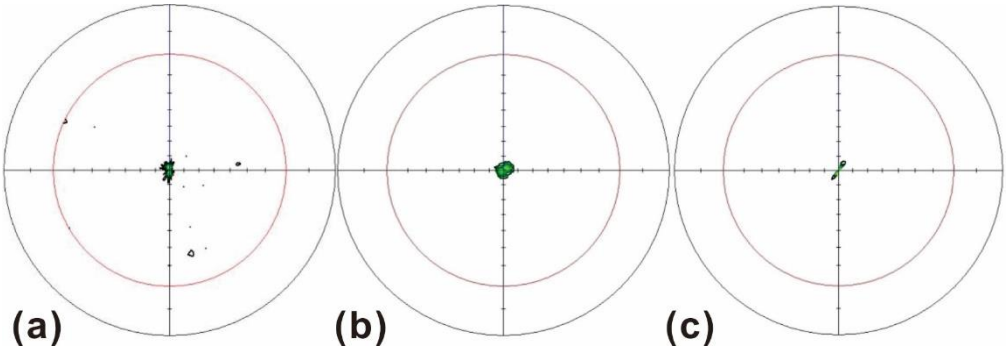

Figure 5.15 (001) LSMO pole figure reflections of films (a) S1, (b) S2 and (c) S3 deposited on LAO

5.3.3 Discussion

Comparing the results of all thin films, it is clear that the quality of the films was improved by adjusting the deposition parameters. This is attributed to the fact that after raising the substrate temperature from750℃ to 850℃, atoms arriving on the substrate acquired more energy and thus had a higher probability to jump into equilibrium positions. It is a very important factor for improving surface roughness and thin film quality. On the other hand, slowing down the power rate of each step could be considered as reducing the arrival rate of atoms at the surface[139, 140]. The power rate in stage AB of S1 and S2, for instance, is 2 W/min in Figure 5.1, which turns to be 1 W/min for S3. The XRD results in Figure 5.14(b) and pole figure results in Figure 5.15 of S2 and S3 are further investigated. A broad S2 (001) diffraction peak covers almost all four peaks present in S3. This indicates that rather than being separated into four different layers in S3, S2 tends to form a continuous layer with a different compositional distribution. However, based on the pole figure results, a degraded crystallinity was observed in the continuous layer compared to a highly consistent orientation in film S3. It is understandable that a better crystallinity may be produced due to a slower changing rate of deposition rate that gives atoms sufficient time to diffuse into the equilibrium sites. It is quite abnormal that a lower power rate actually separates the film into different layers, instead of producing a continuous one. This may be attributed to the fact that since S3 is thicker than S2, this continuous layer cannot be maintained above a certain thickness. Obviously, power rate and deposition

time are also important factors in controlling quality and structure of epitaxial composition gradient thin films. Each layer in S3 could be considered as being undergone an additional annealing in long sputtering time. This additional annealing would induce a further diffusion in the film which caused the separation of different layers.

The out-of-plane parameter and misfit of each peak of S3 in Figure 5.14(b) were calculated and plotted in Figure 5.16. It is known that the lattice parameter of LSMO and LMO are 3.84 Å and 3.95 Å, respectively. Thus, the lattice parameter of LAO pseudo cubic unit cell, which is 3.79 Å, is smaller than that of LSMO and LMO. The value of the misfit m ($m = (a_L - a_S)/a_S$, where a_L and a_S are the layer and substrate unit cell parameters, respectively) between the layer and substrate is positive. This gives rise to the generation of in-plane compressive strain and out-of-plane tensile strain in the film. Thus, the as-calculated out-of-plane parameters in Figure 5.16 are larger than the bulk value. A previous study in our laboratory[141] compared the deposition rate of LMO and LSMO under the same conditions. It was found that LMO has a much larger deposition rate than LSMO. It is expected then that a LMO-rich layer is formed at the beginning of the deposition which can be assigned to P1 and P2. P2 has the largest intensity compared to the other three peaks indicating that most of the film is composed of P2. After the LSMO target power increased and the LMO target power decreased, more and more LSMO was involved into the film and thus a continuous decrease in the out-of-plane parameter was observed in the diffraction pattern by transitioning from P1, P2, and P3 to P4.

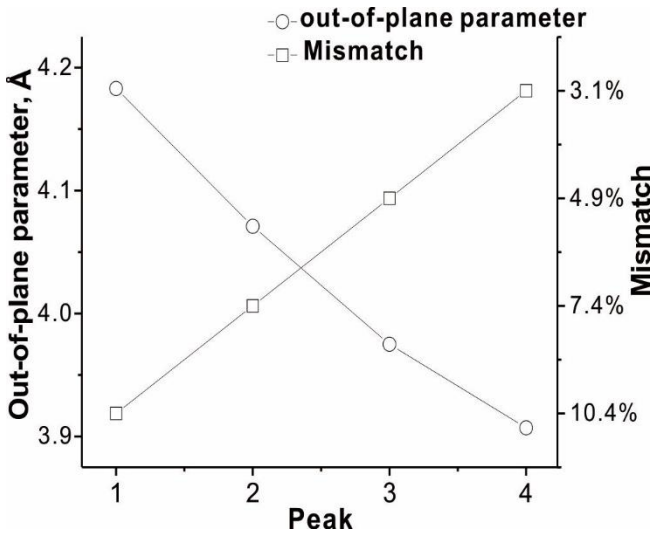

Figure 5.16 Variation of lattice parameter c and misfit strain among the different peaks of S3 in figure 3(b)

It is noticed that the misfit between each layer and the substrate is reduced as the film grows indicating a possible novel strain relaxation mechanism. A similar XRD feature has been reported previously by Maurice et al[125] and Ranno et al[126] as noted earlier. However, since the thickness of the present films is well below the critical thickness, the relaxation mechanism in the present case would be attributed to a different reason. The present results suggest that the relaxation source is due to variation of Sr doping level which is producing a decrease in the lattice parameter along the *c* axis. Another interesting feature is a very large misfit (10.4%) generated at the interface. Normally, this large misfit could not be maintained because it tends to induce dislocations or crystal boundaries to relax the inside strain energy of the film. The reason that the large misfit could be maintained can be attributed to the graded structure in the film. LeGoues et al[106] has compared the

dislocation density between composition uniform and gradient SiGe thin film on Si. They found that the dislocation density decreased significantly (from about 10^8~10^9/cm^2 to 10^4~10^6/cm^2) via composition gradient growth. Similarly, as the Sr doping concentration increasing, the lattice parameter of the layer is getting smaller which actually provides an approach to gradually relax the strain energy in-situ and eventually avoid generation of additional dislocations. Thus, it is expected that composition gradient growth could significantly contribute to the strain relaxation in epitaxial thin films and further improve their performance. Finally, a significant advantage in synthesizing composition gradient film is that we can have cross-coupled properties resulting in new materials.

ECG LSMO thin films were successfully fabricated by magnetron co-sputtering. Three different depositions were conducted by varying the substrate temperature and time interval of power variation. The XRD results showed epitaxial structures for all three films. The epitaxial quality improved by increasing the deposition temperature and the deposition time interval of power variation. Chemical states of O *1s*, Mn *2p*, La *3d* and Sr *3d* obtained by XPS showed that a La-rich phase formed at the surface due to the formation of La oxide. The results also indicated a novel strain relaxation mechanism due to doping concentration gradient, which might also open up various new possibilities of designing new nanoscale structures with unusual cross coupled properties.

5.4 Microstructure and Composition Study on ECG LSMO Thin Film on LAO

In this section, the crystalline and epitaxy of pure epitaxial LMO and LSMO thin films, which mentioned in chapter 4, and ECG LSMO thin film, which labeled as S3 in section 5.3 were characterized and compared by symmetric θ-2θ XRD. The characterization of the tiny variation of lattice parameter due to composition gradient in ECG thin film, which is normally in the scale of angstrom, is usually a puzzle since it is hard to visually display this small amount of variation even by using HRTEM. In this article, a set of low angle x-ray diffraction analysis with varies of incident angles were performed in order to characterize the graded structure of the ECG LSMO thin film. This approach actually offers a very easy, fast, and non-destructive way to show the graded structure directly. Moreover, EDS measured along cross-section of the film, deformed reciprocal lattice points obtained from SAED and pole figure pattern around (001) further confirmed this assumption.

5.4.1 Comparison with Pure LMO and LSMO Epitaxial Thin Films from XRD

The θ-2θ X-ray diffraction patterns in a narrow range around (001) reflection of the as-deposit samples are shown in figure 5.17. Only (001) reflections are present, indicating that all three films are cubic-on-cubic epitaxial structure in the *z* direction. The pure LMO sample contains two separated peaks. The left reflection is contributed to a fully strained LMO layer of which the out-of-plane lattice parameter *c* is 4.089 Å, while the other one corresponded to a partially relaxed LMO layer with a smaller *c* lattice parameter (4.014 Å). The reason of split reflections in pure LMO epitaxial thin film is due to the generation of

dislocations when the film thickness is larger than the critical thickness value. Many previous publications have demonstrated the effect of the critical thickness value on strain relaxation in epitaxial LSMO thin film[87-89] and Angeloni et al[87] further reported the critical thickness value of epitaxial LSMO thin film on LAO substrate which is about 300 Å. The XRD diffraction pattern of the pure LSMO sample only contains one single peak which is corresponded to fully strained LSMO layer and the out-of-plane lattice parameter *c* is calculated as 3.969 Å. This *c* value is similar to the reported results which are deposited by pulsed laser deposition (3.945 Å) and molecular-beam epitaxy (3.974 Å)[142]. Four split peaks are identified around (001) reflection and labeled as P1, P2, P3 and P4 in the XRD pattern of the ECG sample. The very broad reflection P2 almost covers both peaks in the pure LMO diffraction pattern, indicating that a continuous variation of out-of-plane lattice parameters, which are in the range of the two separated values in pure LMO sample, may be included. Distinguished from the pure LMO sample resulted by generation of dislocations, however, the broad peak P2 should be considered as a gradually increment of Sr doping concentration along the growth direction in the ECG LSMO thin film. It is also noticed that P3 is almost identical with the reflection in pure LSMO diffraction pattern suggesting a closed *c* value area as the Sr doping further increased. The value of c lattice parameter in P4 (3.907 Å) is closed to the bulk value of $La_{0.67}Sr_{0.33}MnO_3$ (3.87Å), indicating that a partially strain relaxation occurs in the ECG LSMO thin film. Since the thickness of the ECG film is thinner than the critical thickness, the mechanism of this strain relaxation

should be attributed to the graded reduced structure due to the compositional gradient. The abnormal peak P1 with a very large out-of-plane lattice parameter (4.183 Å) may be corresponded to (001) with orthorhombic structure.

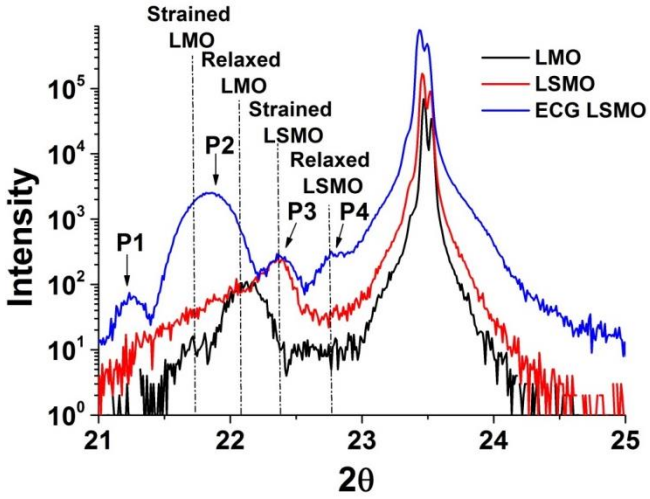

Figure 5.17 θ-2θ symmetric diffraction spectra of pure LMO, pure LSMO and the ECG LSMO film grown on LAO substrate; Arrows indicate the positions of the peaks assigned to the (001) reflection of graded LSMO film. The four different dotted lines are corresponded to the value of out-of-plane lattice parameters of strained LMO, relaxed LMO, strained LSMO and relaxed LSMO

5.4.2 Low angle XRD Characterization of ECG LSMO Thin Film

A set of low angle XRD results with the angle of incident beam raising from 10.2° to 11.5° are shown in figure 5.18. Four areas were identified, corresponding to four peaks labeled in figure 5.17. The very small increment of incident beam angle is designed for identifying subtle change of lattice parameter which is hardly find out even under HRTEM.

It is observed that different diffractions were appeared as the incident angle increased. These successive emerging peaks may be due to different d-spacing values caused by gradually increasing Sr doping. Ewald's sphere model can be used here to illustrate vividly. For an uniformed single crystal, shown in figure 5.19(a) where k_0 is the incident wave vector and k_h is the diffracted wave vector, the reciprocal lattice points are perfect dots, In this case, the scattering vector $\Delta k = k_h - k_0$ will not lie on the surface of the sphere when the incident angle changed. However, for the ECG thin film, the shape of reciprocal lattice points would be elongated due to the non-uniformed strain caused by graded structure shown in figure 5.19(b). The edge of deformed reciprocal lattice points is still tangent to the sphere when the incident beam angle varies in a small range in figure 5.19(c). Thus, different peaks appear in the diffraction pattern as the incident angle increased. It further details and confirms the gradually changing of out-of-plane lattice parameters in ECG thin film. This unique low angle XRD approach could be used in mapping out the variation of strain and lattice parameters in the ECG thin film.

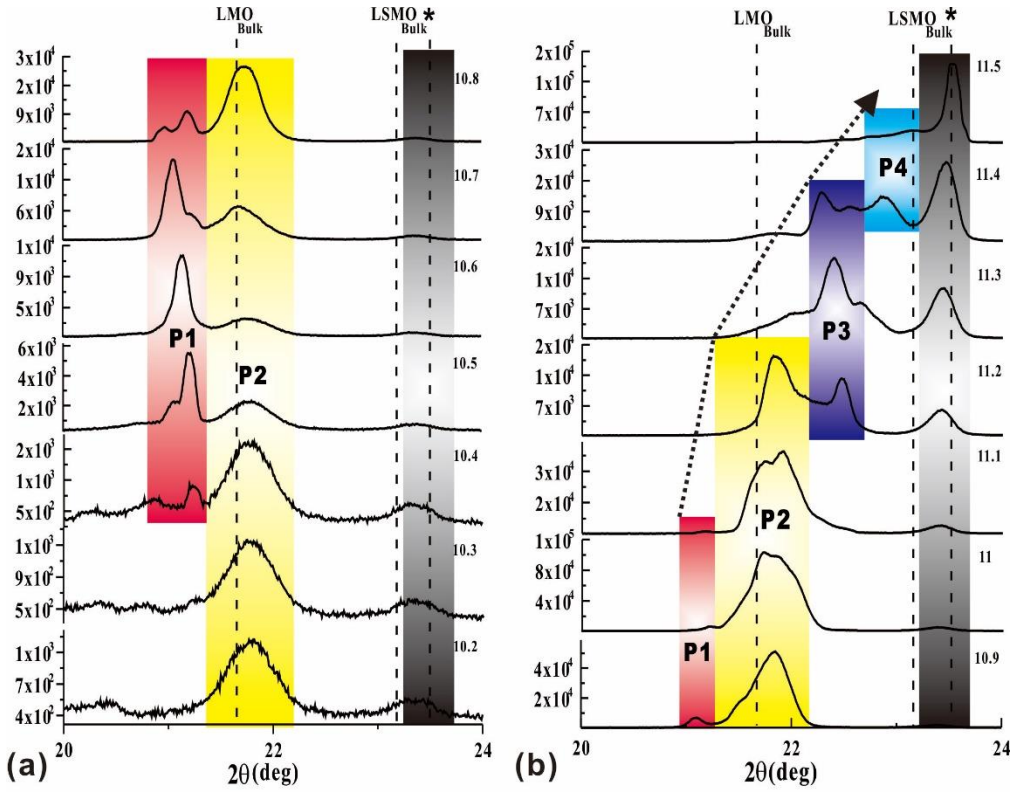

Figure 5.18 Low angle diffraction patterns of ECG LSMO thin film on LAO with different incident angles from 10.2° to 10.8° (a) and from 10.9° to 11.5° (b). Four areas correspond to four peaks in figure 3.Bulk values of lattice parameters of LMO, LSMO and substrate were labeled as dotted line. The asterisks mark the substrate peaks

5.4.3 HRTEM Analysis with EDS on ECG LSMO Thin Film

To further understand the crystalline quality of the ECG LSMO thin film, low magnification cross-section HRTEM investigations were performed, which is shown in Figure 5.20. The thickness of the film was measured from the image which is about 21.5 nm under the critical thickness. The corresponding SAED pattern along the $[001]_{LAO}$ direction taken from the area covering both the film and the substrate was shown inset.

The sharp electron diffraction spots without any satellites observed indicate pseudo-cubic single crystal structure with the orientation relationship of <100>$_{LSMO}$ // <100>$_{LAO}$.

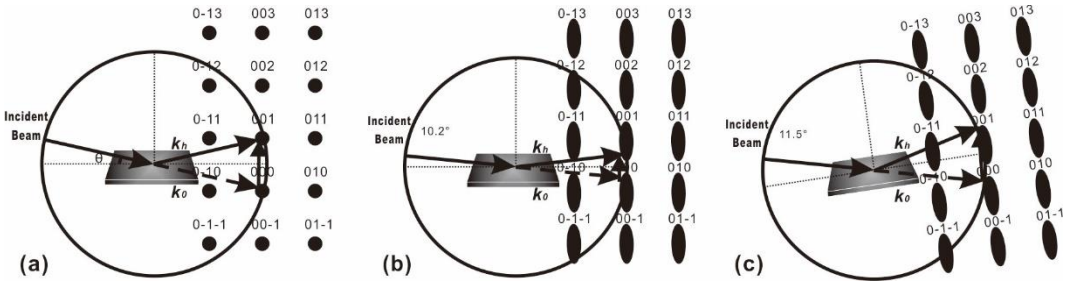

Figure 5.19 Ewald's sphere construction for (a) uniformed (001) single crystal, a non-uniformed (001) single crystal with the incident beam angles changing from (b)10.2º to (c) 11.5º

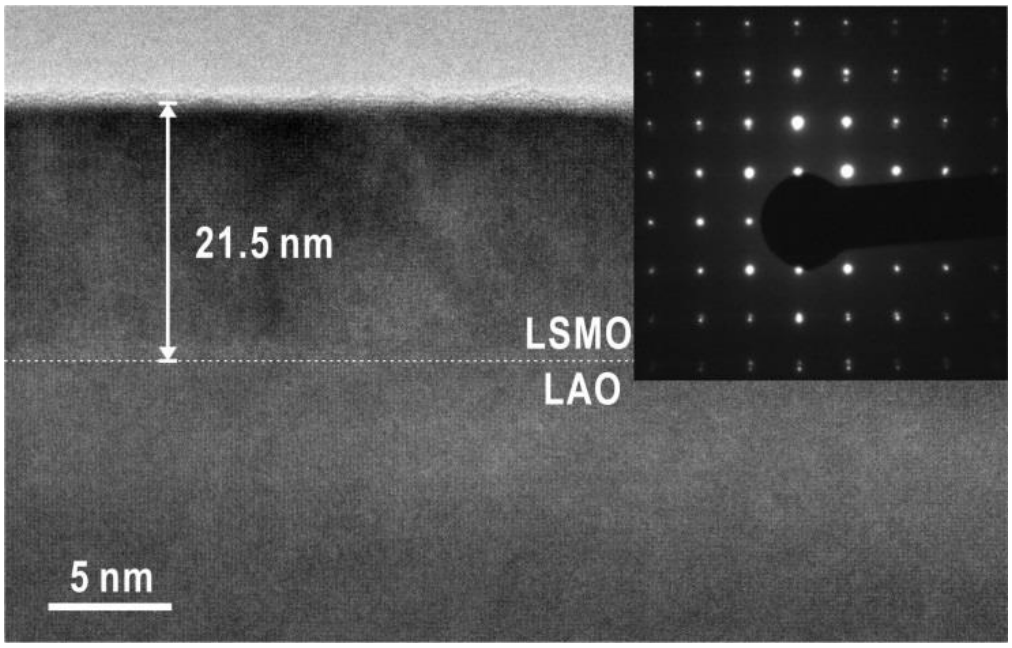

Figure 5.20 Low magnification of cross-section HRTEM image and SAED pattern covering both film and substrate

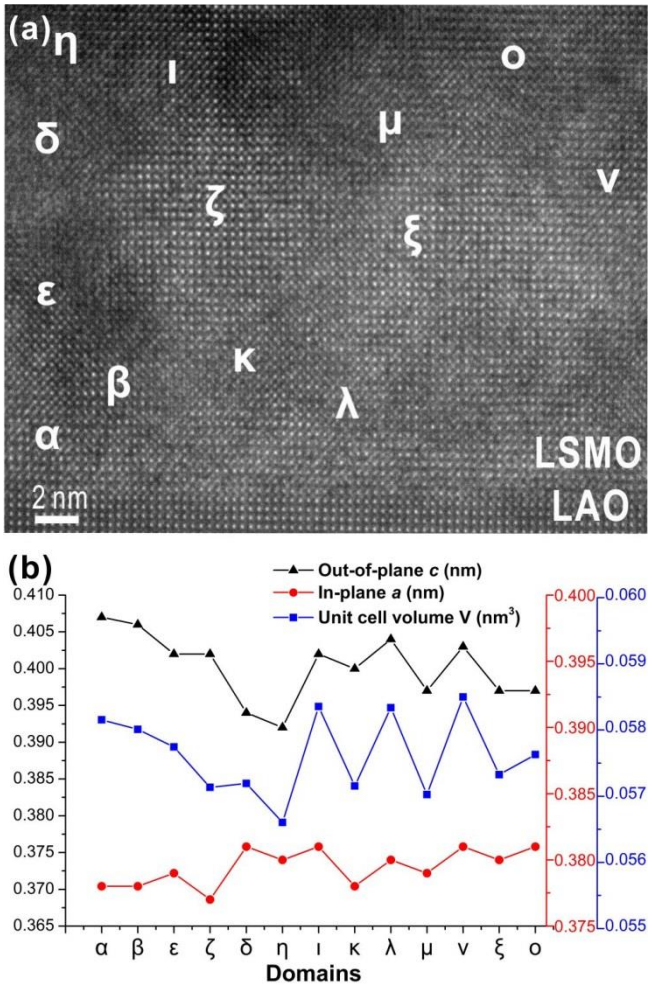

Figure 5.21 (a) high magnitude of cross-section HRTEM image of the interface between the ECG thin film and the substrate; (b) out-of-plane, in-plane lattice parameters and corresponding unit cell volume measured from the different sites in (a)

High magnification of cross-section HRTEM image at interface was also obtained shown in figure 5.21(a). A clear and flat interface with the absence of any dislocation was observed, indicating that a high quality crystalline epitaxial thin film was fabricated with coherent bonding between the film and substrate. In-plane and out-of-plane lattice parameters from different sites were measured and listed in figure 5.21(b). It is found that

the out-of-plane lattice parameters varied from interface to surface shown in the first six measurements while the in-plane lattice parameter maintains around the 3.79 Å, which is the bulk value of the substrate lattice parameter. This variation of unit cell volume reflects a composition changing in the film. It also indicates that the strain relaxation caused by ECG structure only took place along out-of-plane direction while a quiet integral coherent epitaxy was maintained at in-plane direction. Some domains with different lattice parameters were also detected, indicating that the Sr composition variation randomly distributed in the film. Each domain with different unit cell volume contains different Sr doping concentration. The Sr diffusion may be attributed to the long deposition time which could be considered as additional annealing process during deposition.

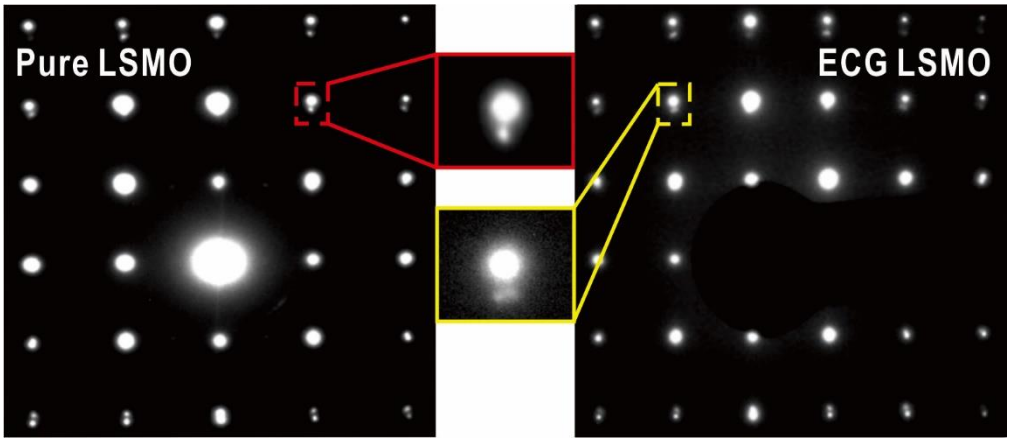

Figure 5.22 SAED patterns (a) pure LSMO and (b) ECG LSMO covering both substrate and film along $[001]_{LAO}$ direction

Compared with the SAED pattern of pure LSMO thin film on LAO shown in figure 5.22(a), it is also found that, instead of dots, the electron diffraction spots of the ECG

LSMO thin film was elongated to be a rod-like shape in figure 5.22(b). The reason should be contributed to the graded structure as the out-of-plane lattice parameter increased due to more Sr involved along the growth direction. These results are coincidence with the pole figure diffraction pattern around (001) peak shown in figure 5.15(c), where the supposed dot turns to be a rod-like region. Both SAED and pole figure results further confirm the formation of ECG structure in the LSMO thin film. EDS measurement was obtained along cross section in order to characterize the composition of the film shown in Figure 5.23. A gradient increased Sr was identified and further confirms the composition gradient structure of the thin film. However, more La content in the film compared to that of Mn indicates that La is preferentially sputtered over Mn in LMO target during deposition.

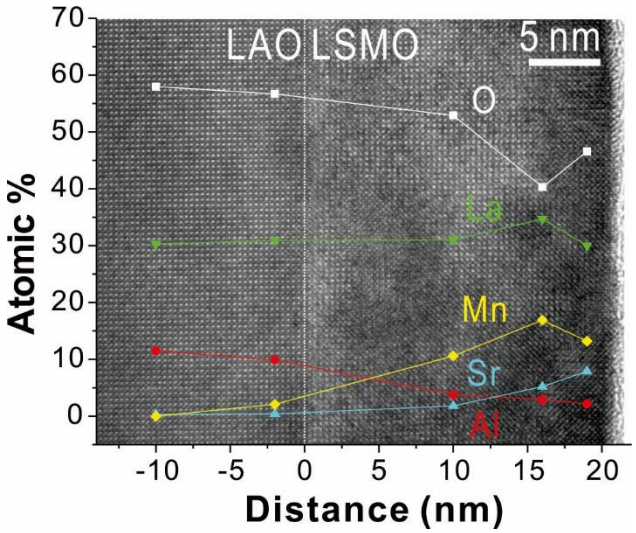

Figure 5.23 EDX results taken along the cross section from substrate to the surface of the film

5.4.4 Discussion

The out-of-plane lattice parameters of ECG thin film were calculated from the low angle XRD results and shown in figure 5.24(a). It is found that *c* values are gradually decreased and finally closed to the bulk value of $La_{0.67}Sr_{0.33}MnO_3$ lattice parameter, indicating that the strain is also gradually relived. The measured successive reduced *c* lattice parameters can be used to deduce Poisson's ratio υ for ECG LSMO thin film. In a cubic system, the measured deformation$\varepsilon_{zz} = (c_{Film} - c_{Bulk})/c_{Bulk}$, where c_{Bulk} is the bulk value of film lattice parameter, is related to the imposed in-plane strain by the expression

$$\varepsilon_{zz} = -\frac{2\vartheta}{1-\vartheta}\varepsilon_{xx} \qquad \text{Eq.5.1}$$

where $\varepsilon_{xx} = \varepsilon_{yy} = (a_{Film} - a_{Bulk})/a_{Bulk}$ is the in-plane strain. Therefore

$$\vartheta = \frac{\varepsilon_{zz}}{\varepsilon_{zz} - 2\varepsilon_{xx}} \qquad \text{Eq.5.2}$$

In this case, the bulk value of LMO lattice parameter (3.95 Å) is used in calculating the Poisson's ratio deduced from P1, while bulk $La_{0.67}Sr_{0.33}MnO_3$ lattice parameter (3.84 Å) is used in calculating P4's Poisson ratio. Due to the Sr doping increased gradually, it is reasonable to modify c_{Bulk} and a_{Bulk} as 3.91 Å in calculating the Poisson's ratio for P2 and 3.87 Å for P3. The variation of out-of-plane strain (figure 5.24(b)) and in-plane strain (figure 5.24(c)) of ECG LSMO thin film were calculated and listed below. It is obviously to found that a gradually decrease of both in-plane and out-of-plane strain, which are almost

down to zero, was achieved in ECG LSMO thin film. Different from general strain relaxation mechanism in composition uniform epitaxial thin film, which is usually due to generation of dislocations when the film is over a critical thickness, this type of strain relaxation is attributed to compositional gradient effect. As the concentration of Sr doping increased, the unit cell is shrunken. With in-plane coherency maintained, the continuous reduced in-plane lattice parameter would certainly help to relive the compressive strain. Moreover, this in-plane relaxation combined with reduction of out-of-plane lattice parameter would further lower the out-of-plane strain. Thus this continuous unit cell shrunken in ECG LSMO thin film actually could relieve biaxial strain at simultaneously.

The corresponding Poisson ratios of ECG LSMO thin film were deduced from Eq 5.2 and shown in figure 5.24(d). The distribution of Poisson ratios ranged from 0.468 to 0.231, which is closed to previous reported results of Sr doped La manganite which are in between of 0.28 for $La_{0.88}Sr_{0.12}MnO_3$ obtained by Hazama et al and 0.41 for $La0_{.835}Sr_{0.165}MnO_3$ by Darling et al[143]. The range of Poisson ratios for ECG LSMO thin film over 0.41, which is the largest Poisson ratio value reported, is due to LMO-rich phase with larger misfit with substrate than Sr doped LMO at the bottom of the film. A Poisson ratio, which is lower than 0.28, was also obtained suggesting that a more effective strain relaxation generated in ECG LSMO thin film comparing with thickness effect on strain relaxation in composition uniform epitaxial LSMO thin film. Thus, it is confirmed that the biaxial strain of epitaxial LSMO thin film could be relieved through compositional gradient

effect under the critical thickness, which could also avoid the generation of dislocations in the thin film.

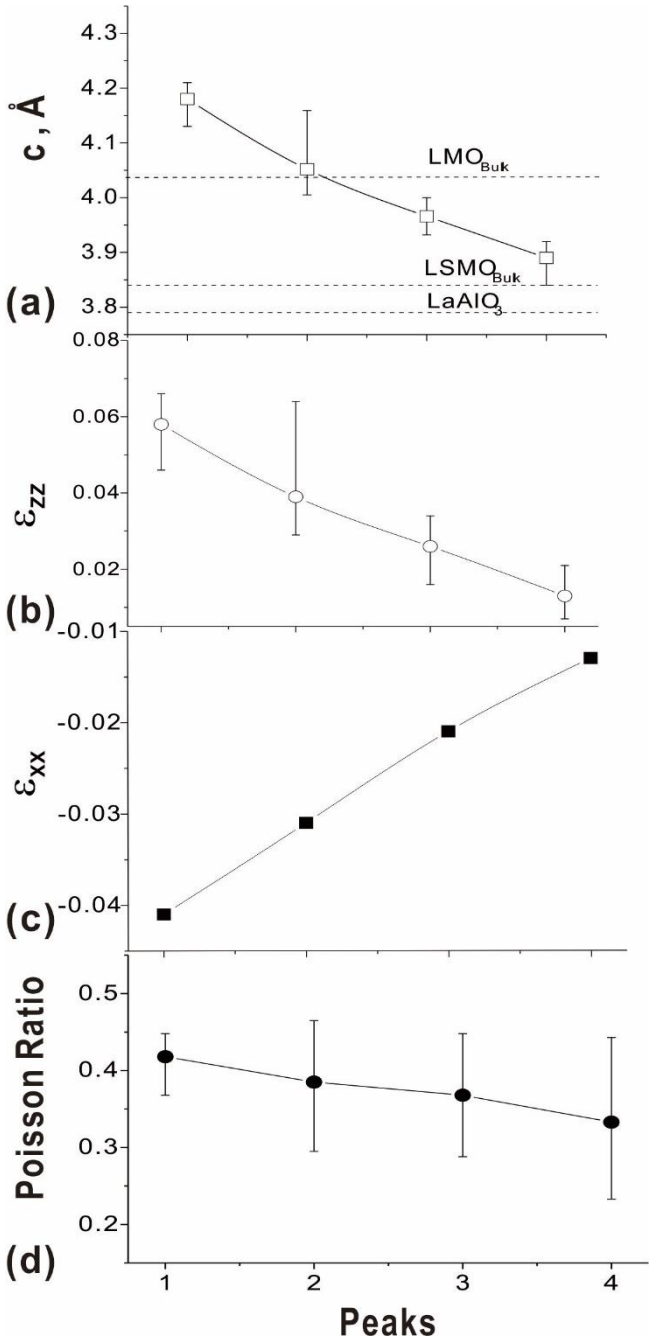

Figure 5.24 Variation of (a) *c* lattice parameters; (b) the corresponding out-of-plane strain; (c) in-plane strain and (d) Poisson ratio calculated from low angle XRD results

In summary, ECG LSMO thin film was successfully fabricated by power controlled rf magnetron co-sputtering. Pure epitaxial LMO and LSMO thin films were also deposited under similar condition for comparison. The microstructures of all three samples were examined by symmetric θ-2θ XRD. A set of low angle XRD were performed on ECG LSMO thin film to display the graded structure directly and further confirmed by HRTEM and SAED results. By compared Poisson ratios in ECG LSMO thin film with previous results, it is demonstrated that usage of ECG structure will be a powerful method to relieve biaxial strain under critical thickness in LSMO thin film, opening up various new possibilities of designing new nanoscale structures with unusual cross coupled properties.

Based on the characterizations above, it is found that the microstructure of co-sputtered LSMO thin film on MgO substrate is entirely different from that of on LAO substrate, and certainly also distinct with the microstructures of pure LMO and LSMO thin films on corresponding substrates. Several differences among these thin films reflected to the variation of growth mechanisms and sputtering techniques will be discussed in this section.

Similar thickness of co-sputtered LSMO thin films on LAO and MgO substrates were found from the characterizations above, which are around 23 nm for both films. The average deposition rate of co-sputtering deposition with LMO and LSMO targets is about 0.096 nm/min which is even lower than the lowest deposition rate of individual target, which corresponds to the one using LSMO target on LAO substrate (0.11 nm/min)

mentioned above. It is reasonable to assume that highly scattering of ad-atoms from different targets happened during sputtering when two targets were co-sputtered simultaneously. The scattering reduces the deposition rate as well as the mobility of ad-atoms reaching on the substrate surface. The deposition rate of both targets on MgO substrate drops much higher than that of on LAO substrate indicating a stronger scattering during the deposition with MgO substrate. This might be explained as the closed deposition rates between these two targets shown in table 4.2. The relative low mobility of ad-atoms could further explain the reason of formation of columnar structure which is not appeared in pure LMO and LSMO thin films. Thus, utilization of higher substrate temperature is necessary in co-sputtering deposition, which could compensate the energy loss of ad-atoms during the scattering. Another problem may be induced by this scattering is the stoichiometry differences compared to that of target especially Sr content.

However, the advantages of this scattering are mainly performed in two aspects. The low deposition rate due to scattering is actually good for growth of single crystalline thin film and improvement of surface roughness as soon as the energy loss compensated. It could be found from the XRD comparison of pure LMO, LSMO and co-sputtered LSMO thin films on LAO substrates that the highest peak intensity with the narrowest FWHM of co-sputtered LSMO thin film indicates better thin film quality. To obtain high quality single crystal thin film by sputtering deposition, many techniques have been utilized in reduction of deposition such as increasing target-substrate distance. Thus, co-sputtering deposition

could be considered alternative approach to achieving low deposition rate for fabrication of high quality single crystal thin film.

Chapter 6

Microstructure of RF Co-sputtered Strontium Doped Lanthanum Manganite Thin Films by Using $LaMnO_3$ and $SrMnO_3$ Targets

6.1 Introduction

Novel phases emerging at atomically sharp interface between dissimilar transition metal oxide compounds are possibly realized due to advanced thin film deposition techniques. The interfaces can exhibit new properties which are not present in either of the adjacent compounds, such as metallic conductivity between a band insulator ($SrTiO_3$) and a Mott insulator ($LaTiO_3$), or ferromagnetism between an antiferromagnet ($CaMnO_3$) and a paramagnet ($CaRuO_3$)[144, 145]. Due to the wide range of charge, orbital and magnetic ordering phenomena, perovskite-type manganites became excellent candidates for fabrication of interfacial phases[146]. For bulk materials, LMO is a Mott insulator (Mn^{3+}) with A-type antiferromagnetic ordering while SMO is a band insulator (Mn^{4+}) with G-type antiferromagnetic ordering. It is expected that ferromagnetic region would be formed at LMO/SMO interface due to a local mixed-valence state by the transfer of eg electrons from LMO to SMO[147].

Many investigations of $(LMO)_k/(SMO)_j$ superlattices $[0.2 \leq j/(k+j) \leq 0.5]$, where k and j are the numbers of unit cells in each layer, focus on the macroscopic magnetic and electronic transport properties[148, 149], structural and chemical profiles[150], interfacial density of states[151, 152], and the metal-insulator transition that occurs as the distance between

interfaces in last decades. It is found that the superlattices exhibit ferromagnetic metals similar to LSMO compounds in thin bilayers $(k + j \leq 8)$ and insulating phase with reduced values of the magnetization and Curie temperature (T_C) with thick bilayers $(k + j \geq 8)$. However, the issue of how sensitive the interfacial ferromagnetism is to structure properties such as roughness and interlayer diffusion has not been reported.

In this chapter, triple-layered LMO/LSMO/SMO and SMO/LSMO/LMO thin films were attempted to fabricate on LAO and MgO substrates by co-sputtered deposition with both LMO and SMO targets. With single target deposited at the top and bottom, a compositional gradient LSMO buffer layer were separated between these two layers. The aim for this design is to explore the effect of compositional graded buffer layer on modification of structure and properties around interface.

6.2 Condition for Fabrication of Triple-layer LMO/LSMO/SMO Thin Films

To increase the Sr content and further investigate on fabrication of more complicated composition graded structure, triple-layer LMO/LSMO/SMO thin films were designed and synthesized on (001) LAO and MgO substrates by co-sputtering deposition. 99.9% two inch LMO and SMO targets purchased from K. J. Lesker Co. were utilized in this set of experiments. The basic deposition procedure is quite similar as the second one; however, some modifications are put and described in the following.

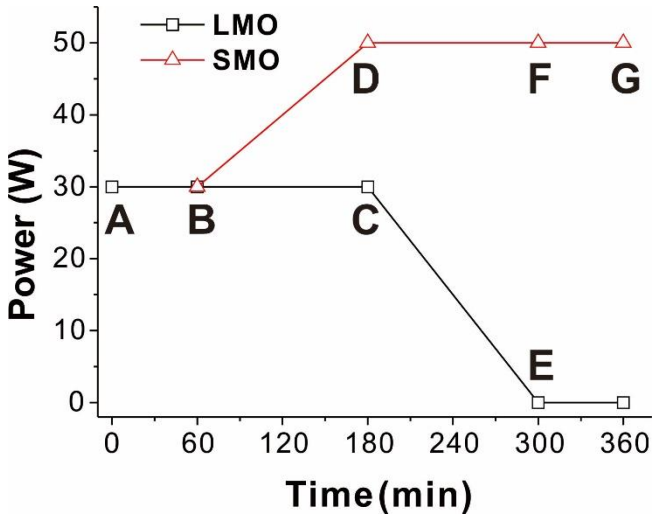

Figure 6.1 Schematic illustration of the specific deposition procedure of SMO top

In this section, the Ar flow rate and the chamber pressure were still 30 sccm and 10 mTorr and the heating temperature on the substrates were maintained at 850 ℃. Two different set of experiments were designed to obtain a triple-layer with Sr doping gradient change. The first design is related to a SMO-rich layer on the surface and a LMO-rich layer on the bottom with a composition gradient transition layer in between, which is named as S-L thin film for short. The deposition procedure for fabrication S-L thin film is shown in figure 6.1. At the beginning only LMO target was utilized with 30 W RF power for 1 hr as AB line illustrated in figure 6.1. After that, the SMO target with initial 30 W RF power was applied and gradually increased up to 50 W in 2 hr (line BD), while the power for LMO was maintained during this time (line BC). The power on LMO target was then decreased gradually after SMO power up to 50 W. As SMO power maintained at 50 W (line DF), LMO power slowly decreased down to 0 W in another 2 hrs (line CE). The whole

fabrication procedure was finished by depositing pure SMO layer on the top of the samples in 1 hr (line FG). Thus, it is expected a triple-layer structure with La-rich phase at bottom and Sr-rich phase on the surface combined with a composition graded transition layer between these two phases. The other set of experiment is using the same procedure but only with opposite targets, which is SMO target with 30 W was used at beginning and LMO target with 50 W was deposited at last. It is expected to have similar triple-layer with Sr-rich phase at bottom and La-rich phase on the top of the samples, which is named as L-S thin film.

6.3 Microstructure Study of SMO Top LMO Bottom Thin Film on LAO Substrate

6.3.1 X-ray Diffraction Study of S-L Thin Film on LAO Substrate

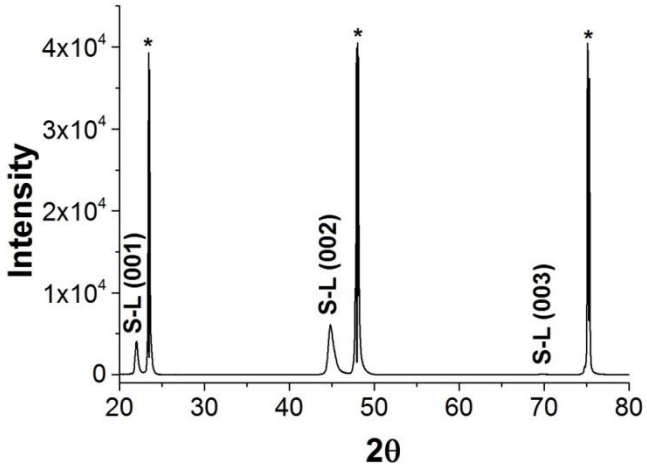

Figure 6.2 Symmetric θ-2θ XRD scan of S-L thin film deposited on LAO substrate; the asterisks mark the substrate peaks

Symmetric θ-2θ XRD pattern of S-L thin film on LAO substrate was obtained shown in figure 6.2. Only (00*l*) reflections from film and substrate were observed indicating epitaxial

structure of the film. It is found that this film possess the highest intensity compared to that of other films on LAO substrates, indicating an improved film quality. As zoomed into the area around (001) reflection and compared with same areas from other thin films on the same substrate, a clear peak shift between S-L film and ECG film was observed and shown in figure 6.3. The shift may be contributed to two possible reasons. The first reason may be due to a relative large thickness of S-L film (~60 nm) which is much larger than that of ECG film (23 nm) and over the critical thickness mentioned before. Hence, the possible misfit dislocations should be induced in S-L thin film which partially relaxed the strain and reduced the out-of-plane lattice spacing of the film. The other reason may be contributed to more Sr doping involved in the film. As utilization of $SrMnO_3$ target instead of $La_{0.67}Sr_{0.33}MnO_3$ target, it is believed that the overall Sr content should be increased, which reduced the average unit cell volume. A very broad reflection of S-L film covering almost P2, P3 and P4 of ECG LSMO film indicates formation of a continuous variation of out-of-plane lattice spacing in S-L epitaxial thin film. Instead of separated peaks shown in XRD pattern of ECG LSMO film, the S-L (001) reflection exhibits a broad peak. It may be due to longer deposition time (6 hr) and lower power rate (0.17 W/min) compared to that of ECG LSMO (4 hr and 1 W/min). This could be considered as additional annealing effect and thus induced composition diffusion which would make the composition variation gradient rather than individual layer.

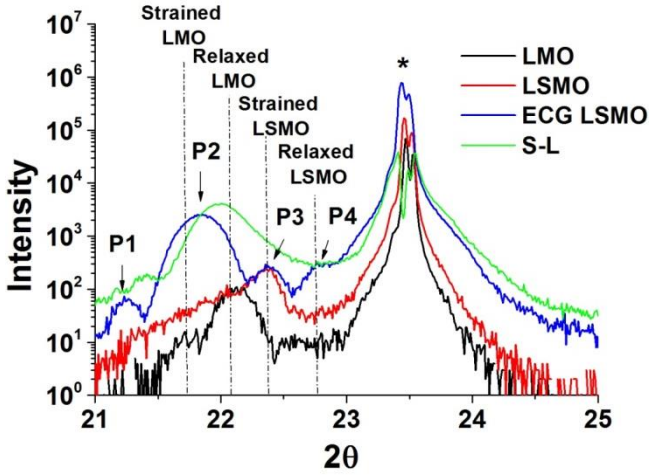

Figure 6.3 θ-2θ symmetric diffraction spectra of pure LMO, pure LSMO, the ECG LSMO and S-L thin films grown on LAO substrates; Arrows indicate the positions of the peaks assigned to the (001) reflection of graded LSMO film. The four different dotted lines are corresponded to the value of out-of-plane lattice parameters of strained LMO, relaxed LMO, strained LSMO and relaxed LSMO

A set of low angle XRD results with incident beam angle varying from 10.5° to 11.4° are shown in figure 6.4. Similar to the low angle XRD results of ECG LSMO thin film above, successive emerging peaks were observed related to different lattice-spacing values due to Sr doping variation. However, only two regions can be detected related to LMO-rich phase and SMO-rich phase respectively. In each region, there are still some sub-peaks which can be further de-convoluted from the region. This could be contributed to occurrence of diffusion to each phase. Since the bulk value of lattice parameter for SMO (0.381 nm) is closed to that of LAO (0.379 nm), the (001) reflection of SMO film is partially overlapped with the substrate peak. Further deconvoluted each reflection in the low angle

results, out-of-plane lattice spacing could be obtained with bulk values of LMO, SMO and LAO lattice parameters labeled shown in figure 6.5.

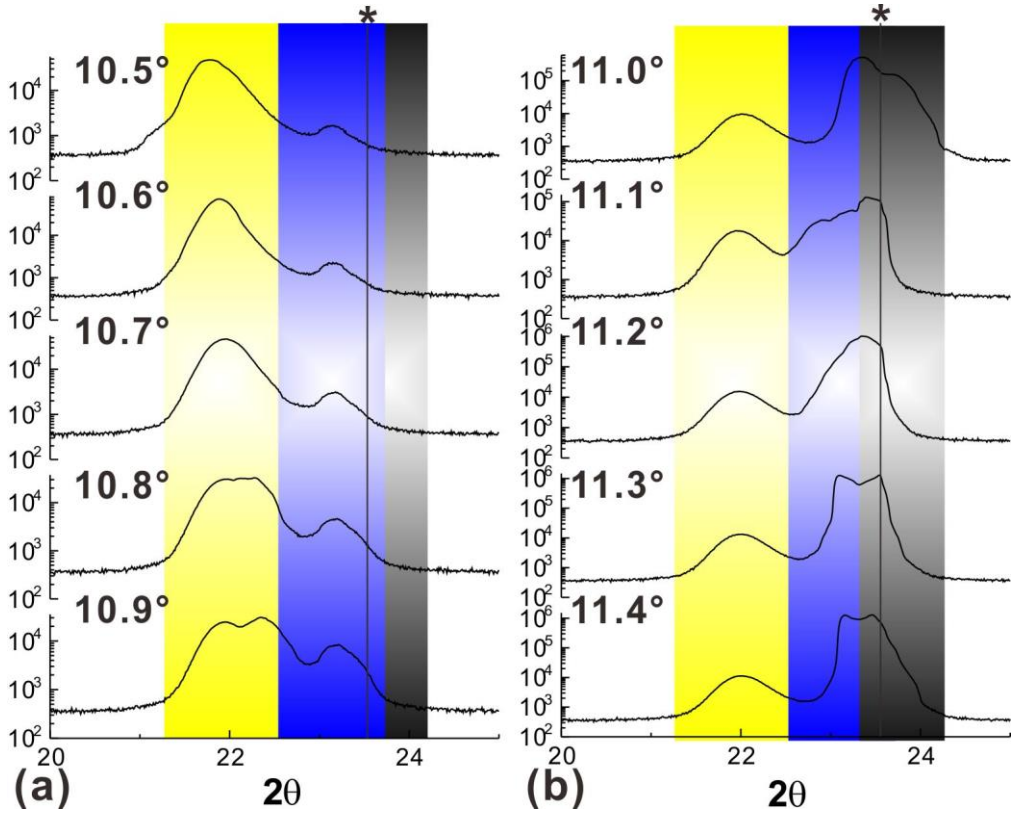

Figure 6.4 Low angle diffraction patterns of S-L thin film on LAO substrate with different incident angles from (a)10.5^{o} to 10.9^{o} and (b) 11^{o} to 11.4^{o}. The asterisks mark the position of substrate peaks

It is found that a continuous decreasing lattice spacing values which are from 4.10 Å to 3.81 Å. It indicates the as the Sr doping increased, the out-of-plane lattice spacing drops down and eventually reaches to bulk value of SMO lattice parameter. Two regions were found separated around 4 Å position. Considering the deposition rate of LMO on LAO substrate and deposition procedure mentioned above, it can be speculated that the

LMO-rich phase should be at least 23 nm. Thus the region with lattice spacing over 4 Å should be contributed to LMO-rich phase under tensile epitaxial strain along growth direction. The other region below 4 Å lattice spacing should be related to composition gradient $La_{1-x}Sr_xMnO_3$ zone and pure SMO zone, respectively.

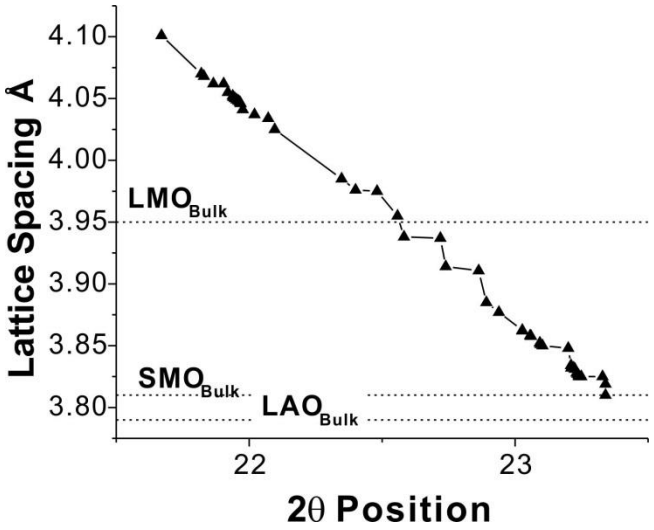

Figure 6.5 Different values of Lattice spacing calculated from low angel XRD results; the bulk values of LMO, SMO and LAO lattice parameters are labeled

6.3.2 HRTEM Analysis with EDS on LMO/SMO Thin Film on LAO Substrate

To further examine the nano structure and composition of as-deposit film, HRTEM analysis was performed. The low magnitude cross-section HRTEM image was obtained and shown in figure 6.6. Very flat surface and clear interface were observed from the image. Without the pre-cleaning process by plasma, the wavy rough interface was disappeared which further confirmed the reason is due to plasma cleaning. The thickness of the film is measured as 54.38 nm and average deposition rate for both LMO and SMO

targets is 0.15 nm/min, which is slightly higher than that of pure LSMO target and co-sputtering deposition with both LMO and LSMO targets. It is because the whole deposition processing involves 2 hr deposition with single target, where the ad-atoms scattering caused by co-sputtering deposition would be avoid during that period.

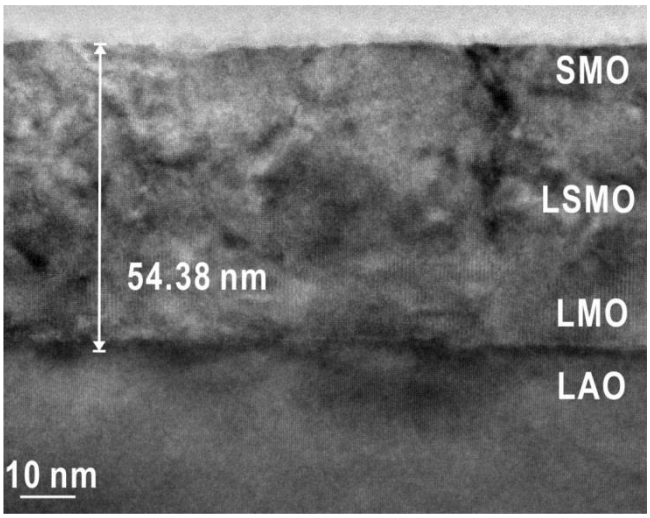

Figure 6.6 Low magnification cross-section HRTEM image of S-L epitaxial thin film deposited on LAO substrate

The SAED pattern along $[100]_{LAO}$ direction covering both film and substrate was also obtained shown in figure 6.7. Two different patterns were obtained from different site of the films which covers both film and substrate. Figure 6.7(a) shows a superposition of the LAO [100] zone and that of LSMO electron diffraction patterns. The SAED pattern confirms that a single crystal structure of cubic perovskite structure epitaxially grown on (001) LAO with an orientation relationship with respect to the substrate of $< 100 >_{film}^{c} // < 100 >_{LAO}$. The in-plane and out-of-plane lattice parameter was measured from the pattern,

where a=0.381 nm and c=0.389 nm indicating a tetragonal unit cell due to epitaxial strain. The lattice parameters in between of bulk values of LMO (0.395 nm) and SMO (0.381 nm) suggests that this area is related to $La_{1-x}Sr_xMnO_3$ gradient zone. On the other hand, the SAED pattern shown in figure 6.7(b) with same electron beam direction was taken from another area covering both film and substrate. The appearance of the weak reflections as the arrows marked clearly indicates the formation of the orthorhombic LSMO structure in this area. The lattice parameters of the orthorhombic structure were obtained: a=0.552 nm, b=0.541 nm, c=0.783 nm. The SAED pattern also indicates that the orthorhombic structure was epitaxially grown on LAO substrate with orientation relationship of $[110]^{O}_{film}//[100]_{LAO}$ and $[001]^{O}_{film}//[010]_{LAO}$.

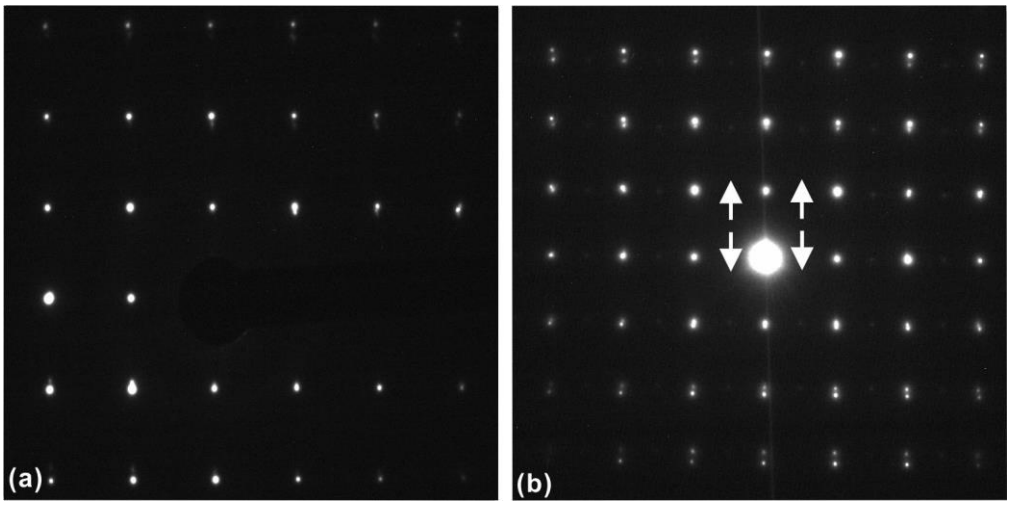

Figure 6.7 Two SAED patterns taken along $[100]_{LAO}$ direction covering both film and substrate from different site of the film indicating two different structures which are related to (a) pseudo-cubic structure and (b) orthorhombic structure, respectively

Figure 6.8 is a high magnification cross-section HRTEM image taken from the interface between the film and the substrate. A very flat and clear interface was observed in figure 6.8(a). The thickness of measured area is about 20.36 nm. The insert of Fourier transformation taken from this area indicates an orthorhombic structure region. Three different domains were observed and labeled as domain 1, 2 and 3 shown in figure 6.8(b) and (c). These three domains are all related to orthorhombic structure with different alignments. The domains were separated by amorphous like boundaries along about 90^{o}. The amorphous structure could be proved from the halo ring in Fourier transformation.

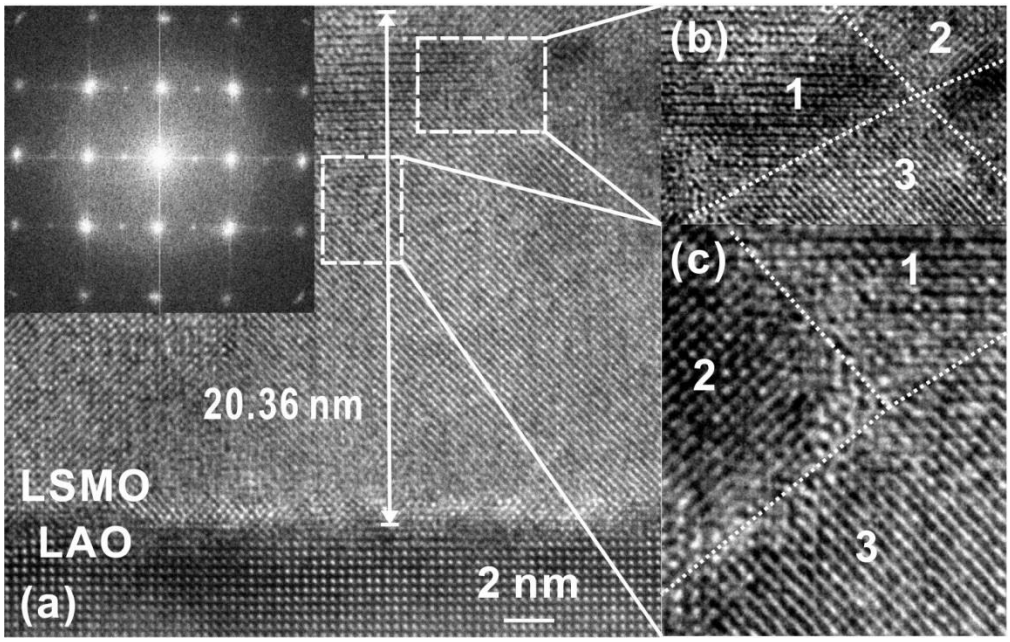

Figure 6.8 (a) High magnification cross-section HRTEM taken from the interface with an insert of Fourier transformation; (b) and (c) enlarged areas taken from square areas in (a). Domain 1, 2 and 3 indicates three orthorhombic regions with different alignments

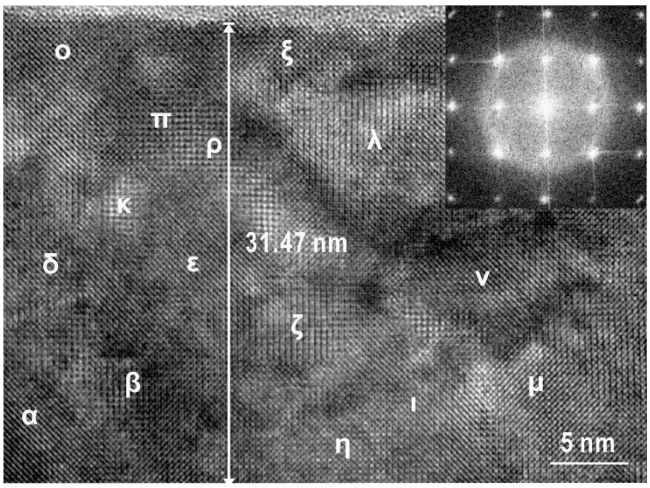

Figure 6.9 High magnification cross-section HRTEM image taken from the area closed to surface with an insert of Fourier transformation; lattice spacing values were obtained from different domains labeled in the image

Another high magnification cross-section HRTEM image taken from the area closed to film surface was shown in figure 6.9. Clear boundaries were observed, which separate the film into several domains. The thickness of this area is about 31.47 nm located closed to the surface. The Fourier transformation of this area was taken and shown in the inset. The absence of the weak reflections between two horizontal adjacent diffractions as shown figure 6.7 (b) indicates the formation of cubic structure in this area. Considering the orthorhombic structure area which is about 20 nm at the bottom of the film, it is reasonable to assume that the whole thin film is consisted of two layers, which are about 20 nm thick orthorhombic structure layer located at the bottom and cubic perovskite layer at the rest part of the film. Combining with the deposition procedure and the single LMO target deposition rate mentioned before, it is found that the pure LMO layer in S-L is about 23 nm

with 1 hr deposition. Thus, the orthorhombic layer may be contributed to LMO-rich phase and the cubic perovskite layer may be due to Sr doping gradually involved by using LMO and SMO targets simultaneously.

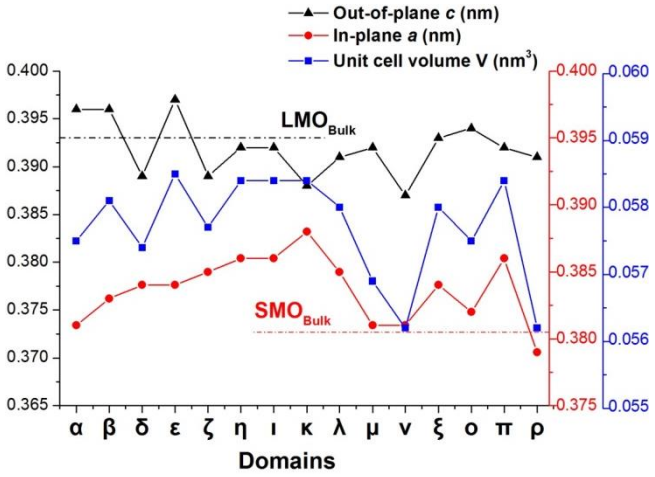

Figure 6.10 Comparisons of lattice spacing values and corresponding volumes in different domains from table 6.1

The out-of-plane and in-plane lattice spacing values as well as unit cell volumes measured from different domains in figure 6.9 were listed in table 6.1. The larger out-of-plane d-spacing compared to that in plane one is due to the formation of tensile epitaxial misfit strain in the layer, which elongated the unit cell to tetragonal structure. However, with various Sr-doping level in each domain, the unit cell volume and thus its deformation degree due to misfit strain are different, which results in a variation of lattice spacing values. It is known that the lattice parameters of bulk cubic perovskite LMO and SMO are 0.395 nm and 0.381 nm, respectively, and the unit cell volumes are 0.0616 nm^3 and 0.0553 nm^3. All the values listed in table 6.1 are in between of that of bulk LMO and

SMO indicates the cubic layer is a mixture of $La_{1-x}Sr_xMnO_3$ ($0<x<1$) domains. This composition variation should be induced by two factors; the deposition procedure and the diffusion.

Table 6-1 Lattice Spacing Taken From Different Sites from Figure 6.9

Domain	Out-of-plane lattice spacing (nm)	In-plane lattice spacing (nm)	Unit cell volume (nm^3)
α	0.396	0.381	0.0575
β	0.396	0.383	0.0581
δ	0.389	0.384	0.0574
ε	0.397	0.384	0.0585
ζ	0.389	0.385	0.0577
η	0.392	0.386	0.0584
ι	0.392	0.386	0.0584
κ	0.388	0.388	0.0584
λ	0.391	0.385	0.0580
μ	0.392	0.381	0.0569
ν	0.387	0.381	0.0562
ξ	0.393	0.384	0.0580
ο	0.394	0.382	0.0575
π	0.392	0.386	0.0584
ρ	0.391	0.379	0.0562

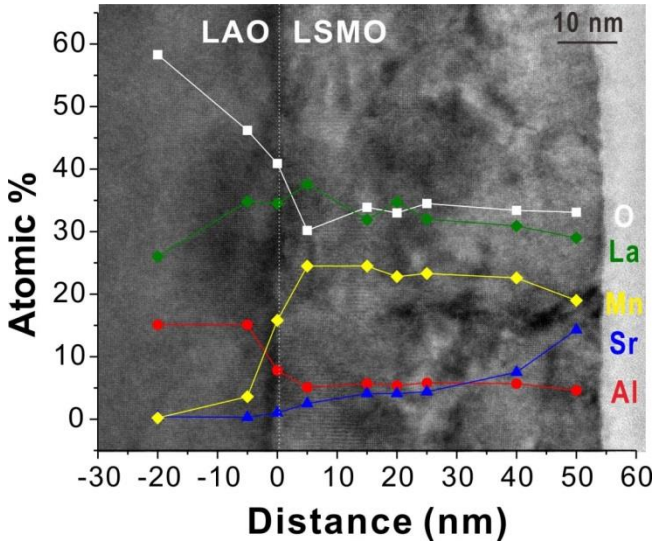

Figure 6.11 EDX results taken along the growth direction from substrate to the surface of the film

Table 6-2 Composition Distribution from EDX Results Shown in Figure 6.11

Position (nm)	O %	Al %	Sr %	Mn %	La %	La: Sr: Mn
-20	58.3	15.1	0.4	0.2	26	122: 2: 1
-5	46.2	15.1	0.3	3.6	34.8	9.7: 0.09: 1
0	40.9	7.8	1	15.8	34.5	1.97: 0.006: 1
5	30.2	5.1	2.5	24.5	37.6	1.54: 0.102: 1
15	33.9	5.7	4.1	24.5	31.9	1.3: 0.168: 1
20	33	5.4	4.1	22.8	34.7	1.52: 0.181: 1
25	34.5	5.8	4.4	23.3	32	1.37: 0.19: 1
40	33.4	5.7	7.5	22.6	30.9	1.37: 0.33: 1
50	33.1	4.6	14.3	19	29	1.53: 0.754: 1

6.4 Microstructure Study of SMO Top LMO Down (S-L) Thin Film on MgO Substrate

Several measurements performed by EDS with 20 nm spot size were obtained along cross section in order to characterize the composition of the film shown in Figure 6.11. The measurement begins from the deep site in the substrate and gradually moves the spot to the surface of the film. The specific data and atomic ratio of La: Sr: Mn obtained in different

sites is summarized in table 6.2. It is found that small amount of Sr can be detected even at the interface, which demonstrates an internal Sr diffusion from the surface to the bottom. This diffusion may be further enhanced due to long deposition time and low power rate acting as additional annealing effect. This enhanced annealing effect could help Sr diffuse to further site of the film. Along the growth direction, similar diffusion also observed on La, which even possesses much higher content than Sr at the surface. This may be contributed a much higher deposition rate of La due to sputter preference. The atomic ratio of La: Sr: Mn was calculated from each measurement shown in table 6.2. It is found that La content is always much higher than that of Mn in the whole film, indicating that there is La preferred sputtering of LMO target during the deposition.

6.4.1 X-ray Diffraction of S-L Thin Film on MgO Substrate

Co-sputtered S-L thin film deposited on MgO substrate was synthesized using the same condition as S-L thin film on LAO in order to analyze the substrate effect in microstructure modification. Symmetric θ-2θ XRD pattern of S-L thin film deposited on LAO substrate was obtained and shown in figure 6.12. Only (00*l*) reflections were observed in the pattern indicating the formation of epitaxial structure of S-L thin film on MgO substrate. As zoomed into the area around (002) reflection and compared with the same areas from pure LMO and LSMO thin films, a clear peak shift between S-L film and the other two was observed shown in figure 6.13. This shift should contribute to more Sr doping induced in S-L film which causes a reduced overall lattice parameter in the film.

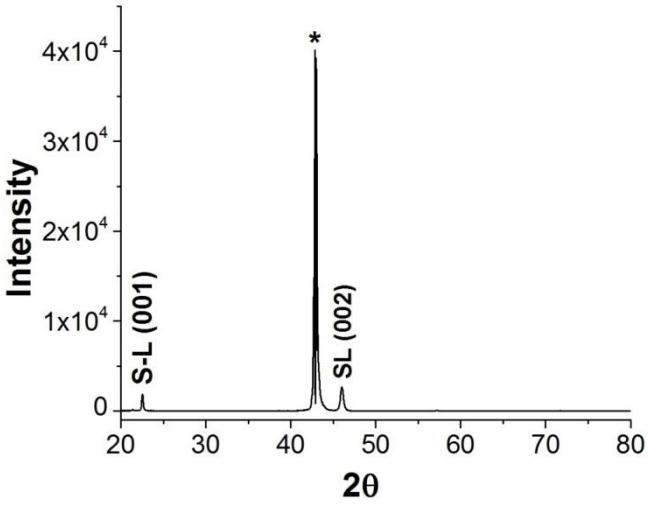

Figure 6.12 Symmetric θ-2θ XRD scan of S-L thin film deposited on MgO substrate; the asterisk is related to (002) MgO substrate peak

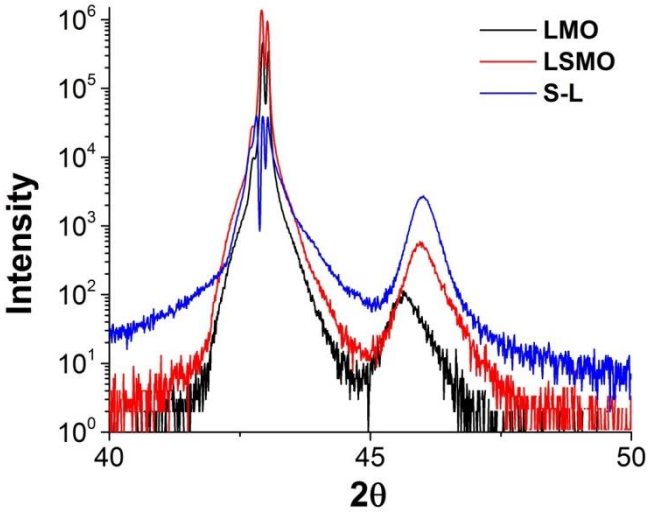

Figure 6.13 θ-2θ symmetric diffraction spectra of pure LMO, pure LSMO and S-L thin films grown on MgO substrates

6.4.2 HRTEM Study of S-L Thin Film on MgO Substrate

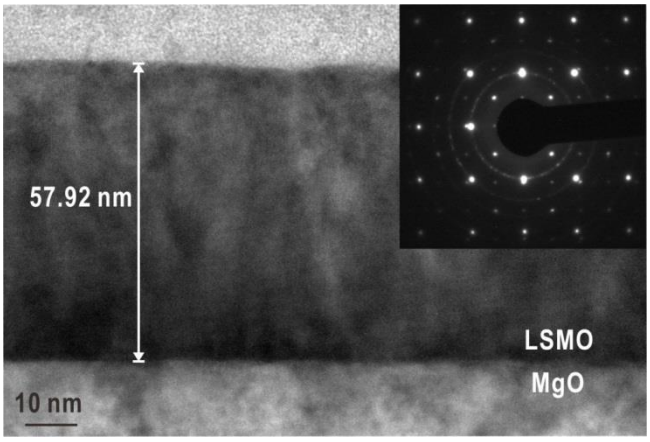

Figure 6.14 Low magnification of cross-section HRTEM image of S-L epitaxial thin film deposited on MgO substrate; SAED taken along $[100]_{MgO}$ direction covering both film and substrate is shown inset

To further examine the nano structure and composition of as-deposit film, HRTEM analysis was performed. The low magnitude cross-section HRTEM image was obtained and shown in figure 6.14. The thickness of the film is measured as 57.92 nm and average deposition rate is calculated which is 0.16 nm/min similar to that of on LAO substrate. SAED pattern taken along $[100]_{MgO}$ direction covering both film and substrate is shown inset. It is found that the pattern comprised two diffraction patterns which are single crystal epitaxial cubic structure with $<100>_{film}$ // $<100>_{MgO}$ and polycrystalline tetragonal structure. The lattice spacing were also measured from the pattern, where $a = 0.393$ nm, $c = 0.392$ nm for epitaxial phase and $d_{(116)}$=0.209 nm and $d_{(217)}$=0.148 nm for the polycrystalline phase.

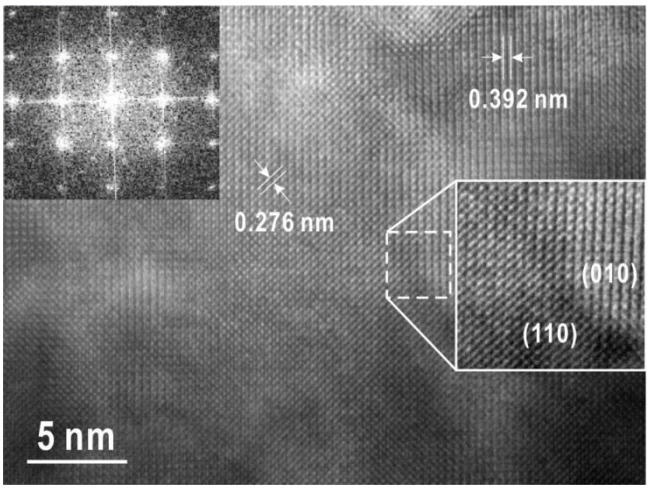

Figure 6.15 High magnification cross-section HRTEM image taken from the area closed to surface with an insert of Fourier transformation

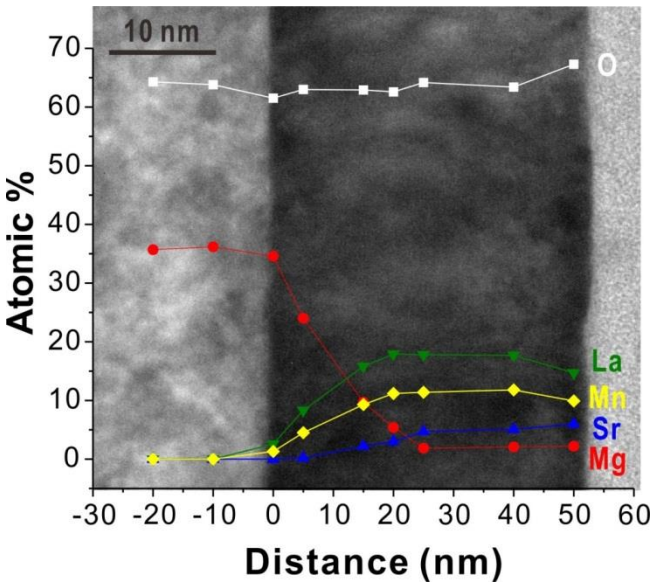

Figure 6.16 EDX results taken along the growth direction from substrate to the surface of the film

High magnification cross-section HRTEM image with Fourier transformation was shown in figure 6.15. Clear boundaries between (110) domain and (010) domain were observed and the corresponding lattice spacing values were also measured. The Fourier

transformation shown inset indicates that the film is cubic structure. No lattice spacing variation observed suggests that strain relaxed from boundaries between different domains. EDS measurement was obtained along cross section in order to characterize the composition of the film shown in figure 6.16. A gradient increased Sr was identified and further confirms the composition gradient structure of the film.

Chapter 7

Conclusion

In this body of work, the examination of three different types of Strontium doped lanthanum manganite thin films synthesized by magnetron sputtering in the SaNEL allowed for the development of a detailed understanding between the processing conditions, the nano-scale structure and strain relaxation of the as-deposited thin films. Pure Lanthanum manganite and strontium doped lanthanum manganite thin films which were epitaxially grown on (001) single crystalline LAO and MgO were fabricated by using single target deposition. The optimum deposition conditions were explored as preparation for synthesis epitaxial composition gradient strontium doped lanthanum manganite thin films by using co-sputtering deposition later. Surface morphology and microstructure of as-deposit thin films were characterized by AFM, XRD and HRTEM. Pseudo-cubic structure was identified in epitaxial lanthanum manganite thin film on LAO and strontium doped lanthanum manganite on MgO substrate, while orthorhombic structure was obtained in epitaxial strontium lanthanum manganite on LAO and lanthanum manganite on MgO substrate. Deposition rates of each target on different substrate were calculated.

ECG strontium doped lanthanum manganite thin films were prepared on the same substrates by using co-sputtering deposition with both targets deposited simultaneously. The as-deposit thin films using novel deposition procedure with different conditions were compared. The substrate temperature and power rate of each target are considered as the

key factor for controlling the quality of the films. The surface morphology, microstructure and composition ratio of each element were characterized by AFM, XRD, HRTEM and XPS. A novel low angle XRD method was involved to examine the graded structure with the nano-scaled variation. It is found that polycrystalline structure with pseudo-cubic columnar domains was formed in the film on MgO substrate while epitaxial pseudo-cubic structure was obtained in the film on LAO substrate. The composition gradient of Sr doping was confirmed by EDS analysis along growth direction. The boundaries between each column were considered as a strain relaxation source in polycrystalline thin film. The ECG thin film, which is under the critical thickness, exhibits a novel strain relaxation which is considered as composition grade structure effect. Thus, the ECG buffer layer was confirmed as an effective method in strain controlling.

To further complex the structure and develop for application, a triple-layer strontium doped lanthanum manganite thin films on LAO and MgO substrates were deposited by using co-sputtering deposition with LMO target and SMO target. The films were designed to have a LMO layer at bottom and SMO layer on surface with both La and Sr gradient layer in between. The microstructure of as-deposit films were identified as epitaxial structure. Two epitaxial layers were found in the film on LAO substrate where orthorhombic structure was obtained below about 20 nm and pseudo-cubic structure was formed on the top. Similar strain relaxation was also observed in the film. This may produce “new” materials with the properties that are not available in the individual

component phases, which might also open up various new possibilities of designing new nanoscale structures with unusual cross coupled properties.

References

1. H. Schmid, Bulletin Of Materials Science **17** (7), 1411 (1994).

2. L. E. Cross, Ferroelectrics **76** (3-4), 241 (1987).

3. J. G. Bednorz and K. A. Muller, Zeitschrift Fur Physik B-Condensed Matter **64** (2), 189 (1986).

4. C. W. Chu, P. H. Hor, R. L. Meng, L. Gao, Z. J. Huang and Y. Q. Wang, Physical Review Letters **58** (4), 405 (1987).

5. S. N. Putilin, E. V. Antipov, O. Chmaissem and M. Marezio, Nature **362** (6417), 226 (1993).

6. Y. Maeno, H. Hashimoto, K. Yoshida, S. Nishizaki, T. Fujita, J. G. Bednorz and F. Lichtenberg, Nature **372** (6506), 532 (1994).

7. M. Fiebig, Journal Of Physics D-Applied Physics **38** (8), R123 (2005).

8. S. W. Cheong and M. Mostovoy, Nature Materials **6** (1), 13 (2007).

9. M. Koizumi, Composites **Part B** (28), 1 (1997).

10. S. Mann and G. A. Ozin, Nature **382** (6589), 313 (1996).

11. D. H. Kim, D. Y. Lee, H. S. Lee, W. H. Lee, Y. H. Kim, J. I. Han and K. Cho, Advanced Materials **19** (5), 678 (2007).

12. E. Muller, C. Drasar, J. Schilz and W. A. Kaysser, Materials Science And Engineering a-Structural Materials Properties Microstructure And Processing **362** (1-2), 17 (2003).

13. F. F. Liu, X. Y. Li, Q. D. Zhao, Y. Hou, X. Quan and G. H. Chen, Acta Materialia **57** (9), 2684 (2009).

14. D. Placencia, W. N. Wang, R. C. Shallcross, K. W. Nebesny, M. Brumbach and N. R. Armstrong, Advanced Functional Materials **19** (12), 1913 (2009).

15. F. Watari, A. Yokoyama, F. Saso, M. Uo and T. Kawasaki, Composites Part B-Engineering **28** (1-2), 5 (1997).

16. A. J. Ruys, E. B. Popov, D. Sun, J. J. Russell and C. C. J. Murray, Journal Of the European Ceramic Society **21** (10-11), 2025 (2001).

17. J. Sakai, C. Autret-Lambert, T. Sauvage, B. Courtois, J. Wolfman and F. Gervais, Journal of Crystal Growth **380**, 106 (2013).

18. Y. J. Mii, Y. H. Xie, E. A. Fitzgerald, D. Monroe, F. A. Thiel, B. E. Weir and L. C. Feldman, Applied Physics Letters **59** (13), 1611 (1991).

19. Y. Sato, M. Moriyama, M. Hanayama, H. Naito and S. Tamura, Ieee Transactions on Pattern Analysis And Machine Intelligence **19** (3), 253 (1997).

20. Y. Konishi, Z. Fang, M. Izumi, T. Manako, M. Kasai, H. Kuwahara, M. Kawasaki, K. Terakura and Y. Tokura, Journal Of the Physical Society Of Japan **68** (12), 3790 (1999).

21. M. Paranjape, A. K. Raychaudhuri, N. D. Mathur and M. G. Blamire, Physical Review B **67** (21), 214415 (2003).

22. J. Z. Sun, D. W. Abraham, R. A. Rao and C. B. Eom, Applied Physics Letters **74** (20), 3017 (1999).

23. M. Ziese, H. C. Semmelhack and K. H. Han, Physical Review B **68** (13), 134444 (2003).

24. K. H. Ahn and A. J. Millis, Phys. Rev. B. **64** (11), 115103 (2001).

25. J. C. Jiang, E. I. Meletis and K. I. Gnanasekar, Appl. Phys. Lett. **80** (25), 4831 (2002).

26. J. C. Jiang, E. I. Meletis and K. I. Gnanasekar, J. Mater. Res. **18** (11), 2556 (2003).

27. J. C. Jiang, L. L. Henry, K. I. Gnanasekar, C. L. Chen and E. I. Meletis, Nano Lett. **4** (4), 741 (2004).

28. Y. Fang, V. R. Sakhalkar, J. He, H. Q. Jiang, J. C. Jiang and E. I. Meletis, Journal Of Nano Research **14**, 83 (2011).

29. M. Opel, M. Journal Of Physics D-Applied Physics **45** (3), 033001 (2012).

30. Y. M. Chiang, D. P. Birnie and W. D. Kingery, Physical Ceramics: Principles for Ceramic Science and Engineering, John Wiley & Sons, Inc. (1997).

31. K. C. Kao, Dielectric Phenomena in Solids, Elsevier Academic Press (2004).

32. M. Johnsson and P. Lemmens, Crystallography and Chemistry of Perovskites, Handbook of Magnetism and Advanced Magnetic Materials, John Wiley & Sons, Ltd (2007).

33. A. F. Wells, Structural Inorganic Chemistry, Oxford Science Publications (1995).

34. U. Müller, Inorganic Structural Chemistry, Wiley & Sons Ltd (1993).

35. A. Manthiram and J. B. Goodenough, Journal Of Solid State Chemistry **92** (1), 231 (1991).

36. J. B. Goodenough, Magnetism and the Chemical Bond, Wiley and Sons New York (1963).

37. J. Mathon, Contemporary Physics 32, 143 (1991).

38. D. B. Teresa, K. A. Neves, C. B. Neto, P. A. G. Fregonezi, M. R. B. de Oliveira, J. A. S. Zuanon, E. A. Donadi, C. T. Mendes and C. P. Soares, Acta Histochemica **109** (5), 377 (2007).

39. R. Vonhelmolt, J. Wecker, B. Holzapfel, L. Schultz and K. Samwer, Physical Review Letters **71** (14), 2331 (1993).

40. A. Barnabe, M. Hervieu, C. Martin, A. Maignan and B. Raveau, Journal Of Materials Chemistry **8** (6), 1405 (1998).

41. R. Meservey and P. M. Tedrow, Physics Reports-Review Section Of Physics Letters **238** (4), 173 (1994).

42. D. J. Monsma and S. S. P. Parkin, Applied Physics Letters **77** (5), 720 (2000).

43. C. Kaiser, S. van Dijken, S. H. Yang, H. S. Yang and S. S. P. Parkin, Physical Review Letters **94** (24), 247203 (2005).

44. L. Ranno, A. Llobet, M. B. Hunt and J. Pierre, Applied Surface Science **138**, 228 (1999).

45. T. Hashimoto, N. Ishizawa, N. Mizutani and M. Kato, Journal Of Crystal Growth **84** (2), 207 (1987).

46. A. Hammouche, E. Siebert and A. Hammou, Materials Research Bulletin **24** (3), 367 (1989).

47. R. Millini and M. F. Gagliardi, Journal Of Materials Science **29** (17), 4629 (1994).

48. A. Chakraborty, P. S. Devi and H. S. Maiti, Materials Letters **20** (1-2), 63 (1994).

49. P. Shuk, L. Tichonova and U. Guth, Solid State Ionics **68** (3-4), 177 (1994).

50. K. Heimdal, T. I. Andersen, M. Skrede, S. D. Fossa, K. Berg and A. L. Borresen, Cancer Epidemiology Biomarkers & Prevention **4** (2), 123 (1995).

51. A. Benabad, A. Daoudi, R. Salmon and G. Leflem, Journal Of Solid State Chemistry **22** (2), 121 (1977).

52. H. Fujishiro, T. Fukase and M. Ikebe, Journal Of the Physical Society Of Japan **67** (8), 2582 (1998).

53. E. Dagotto, T. Hotta and A. Moreo, Physics Reports-Review Section Of Physics Letters **344** (1-3), 1 (2001).

54. C. Zener, Physical Review **82** (3), 403 (1951).

55. G. H. Jonker and J. H. Vansanten, Physica **16** (3), 337 (1950).

56. P. W. Anderson and H. Hasegawa, Physical Review **100** (2), 675 (1955).

57. A. P. Ramirez, Journal Of Physics-Condensed Matter **9** (39), 8171 (1997).

58. A. J. Millis, P. B. Littlewood and B. I. Shraiman, Physical Review Letters **74** (25), 5144 (1995).

59. A. J. Millis, B. I. Shraiman and R. Mueller, Physical Review Letters **77** (1), 175 (1996).

60. A. J. Millis, Nature **392** (6672), 147 (1998).

61. J. H. Vansanten and G. H. Jonker, Physica **16** (7-8), 599 (1950).

62. G. H. Jonker and J. H. Vansanten, Physica **19** (1), 120 (1953).

63. J. Volger, Physica **20** (1), 49 (1954).

64. E. O. Wollan and W. C. Koehler, Physical Review **100** (2), 545 (1955).

65. Z. Jirak, S. Vratislav and J. Zajicek, Physica Status Solidi a-Applied Research **52** (1), K39 (1979).

66. E. Pollert, S. Krupicka and E. Kuzmicova, Journal Of Physics And Chemistry Of Solids **43** (12), 1137 (1982).

67. R. M. Kusters, J. Singleton, D. A. Keen, R. Mcgreevy and W. Hayes, Physica B **155** (1-3), 362 (1989).

68. K. Chahara, T. Ohno, M. Kasai, Y. Kanke and Y. Kozono, Applied Physics Letters **62** (7), 780 (1993).

69. H. L. Ju, C. Kwon, Q. Li, R. L. Greene and T. Venkatesan, Applied Physics Letters **65** (16), 2108 (1994).

70. S. Jin, T. H. Tiefel, M. Mccormack, R. A. Fastnacht, R. Ramesh and L. H. Chen, Science **264** (5157), 413 (1994).

71. G. C. Xiong, Q. Li, H. L. Ju, S. M. Bhagat, S. E. Lofland, R. L. Greene and T. Venkatesan, Applied Physics Letters **67** (20), 3031 (1995).

72. P. Dey and T. K. Nath, Applied Physics Letters **87** (16), 162501 (2005).

73. J. Z. Sun and A. Gupta, Annual Review Of Materials Science **28**, 45 (1998).

74. P. K. Muduli, G. Singh, R. Sharma and R. C. Budhani, Journal Of Applied Physics **105** (11), 113910 (2009).

75. A. Urushibara, Y. Moritomo, T. Arima, A. Asamitsu, G. Kido and Y. Tokura, Physical Review B **51** (20), 14103 (1995).

76. J. Li, C. K. Ong, J. M. Liu, Q. Huang and S. J. Wang, Applied Physics Letters **76** (8), 1051 (2000).

77. M. Rajeswari, R. Shreekala, A. Goyal, S. E. Lofland, S. M. Bhagat, K. Ghosh, R. P. Sharma, R. L. Greene, R. Ramesh, T. Venkatesan and T. Boettcher, Applied Physics Letters **73** (18), 2672 (1998).

78. J. A. Sulpizio, S. Ilani, P. Irvin and J. Levy, Annual Review Of Materials Research, Vol **44**, 117 (2014).

79. J. Heidler, C. Piamonteze, R. V. Chopdekar, M. A. Uribe-Laverde, A. Alberca, M. Buzzi, A. Uldry, B. Delley, C. Bernhard and F. Nolting, Physical Review B **91** (2), 24406 (2015).

80. A. Alberca, C. Munuera, J. Tornos, F. J. Mompean, N. Biskup, A. Ruiz, N. M. Nemes, A. de Andres, C. Leon, J. Santamaria and M. Garcia-Hernandez, Physical Review B **86** (14), 144416 (2012).

81. A. Alberca, N. M. Nemes, F. J. Mompean, T. Feher, F. Simon, J. Tornos, C. Leon, C. Munuera, B. J. Kirby, M. R. Fitzsimmons, A. Hernando, J. Santamaria and M. Garcia-Hernandez, Physical Review B **88** (13), 134410 (2013).

82. C. Adamo, X. Ke, H. Q. Wang, H. L. Xin, T. Heeg, M. E. Hawley, W. Zander, J. Schubert, P. Schiffer, D. A. Muller, L. Maritato and D. G. Schlom, Applied Physics Letters **95** (11), 112504 (2009).

83. A. M. Haghiri-Gosnet and J. P. Renard, Journal Of Physics D-Applied Physics **36** (8), R127 (2003).

84. T. K. Nath, R. A. Rao, D. Lavric, C. B. Eom, L. Wu and F. Tsui, Applied Physics Letters **74** (11), 1615 (1999).

85. R. A. Rao, D. Lavric, T. K. Nath, C. B. Eom, L. Wu and F. Tsui, Applied Physics Letters **73** (22), 3294 (1998).

86. A. Barman and G. Koren, Applied Physics Letters **77** (11), 1674 (2000).

87. M. Angeloni, G. Balestrino, N. G. Boggio, P. G. Medaglia, P. Orgiani and A. Tebano, Journal of Applied Physics **96** (11), 6387 (2004).

88. J. L. Maurice, F. Pailloux, A. Barthelemy, O. Durand, D. Imhoff, R. Lyonnet, A. Rocher and J. P. Contour, Philosophical Magazine **83** (28), 3201 (2003).

89. L. Ranno, A. Llobet, R. Tiron and E. Favre-Nicolin, Applied Surface Science **188** (1-2), 170 (2002).

90. J. C. Jiang, L. L. Henry, K. I. Gnanasekar, C. L. Chen and E. I. Meletis, Nano Letters **4** (4), 741 (2004).

91. J. C. Jiang, E. I. Meletis and K. I. Gnanasekar, Journal Of Materials Research **18** (11), 2556 (2003).

92. J. C. Jiang, E. I. Meletis and K. I. Gnanasekar, Applied Physics Letters **80** (25), 4831 (2002).

93. K. Steenbeck, R. Hiergeist, A. Revcolevschi and L. Pinsard-Gaudart, Polycrystalline Metal And Magnetic Thin Films **562**, 57 (1999).

94. Y. Suzuki, H. Y. Hwang, S. W. Cheong and R. B. vanDover, Applied Physics Letters **71** (1), 140 (1997).

95. B. D. Cullity, Ieee Transactions on Magnetics **Mag8** (3), 354 (1972).

96. F. Tsui, M. C. Smoak, T. K. Nath and C. B. Eom, Applied Physics Letters **76** (17), 2421 (2000).

97. A. M. Haghiri-Gosnet, J. Wolfman, B. Mercey, C. Simon, P. Lecoeur, M. Korzenski, M. Hervieu, R. Desfeux and G. Baldinozzi, Journal Of Applied Physics **88** (7), 4257 (2000).

98. M. Strikovski and J. H. Miller, Applied Physics Letters **73** (12), 1733 (1998).

99. R. Desfeux, S. Bailleul, A. Da Costa, W. Prellier and A. M. Haghiri-Gosnet, Applied Physics Letters **78** (23), 3681 (2001).

100. M. Izumi, Y. Konishi, T. Nishihara, S. Hayashi, M. Shinohara, M. Kawasaki and Y. Tokura, Applied Physics Letters **73** (17), 2497 (1998).

101. B. Vengalis, A. Maneikis, F. Anisimovas, R. Butkute, L. Dapkus and A. Kindurys, Journal Of Magnetism And Magnetic Materials **211** (1-3), 35 (2000).

102. F. Pailloux, D. Imhoff, T. Sikora, A. Barthelemy, J. L. Maurice, J. P. Contour, C. Colliex and A. Fert, Physical Review B **66** (1), 14417 (2002).

103. D. L. Harame, K. Schonenberg, M. Gilbert, D. Nguyenngoc, J. Malinowski, S. J. Jeng, B. Meyerson, J. D. Cressler, R. Groves, G. Berg, K. Tallman, K. Stein, G. Hueckel, C. Kermarrec, T. Tice, G. Fitzgibbons, K. Walter, D. Colavito, T. Houghton, N. Greco, T. Kebede, B. Cunningham, S. Subbanna, J. H. Comfort and E. F. Crabbe, International Electron Devices Meeting 1994 - Iedm Technical Digest, 437 (1994).

104. G. Freeman, K. Schonenberg, D. Ahlgren, S. J. Jeng, D. Nguyen-Ngoc, K. Stein, D. Colavito, S. Subbanna, D. Harame and B. Meyerson, Epitaxy And Applications Of Si-Based Heterostructures **533**, 19 (1998).

105. B. S. Meyerson, Proceedings Of the Ieee **80** (10), 1592 (1992).

106. F. K. Legoues, B. S. Meyerson and J. F. Morar, Physical Review Letters **66** (22), 2903 (1991).

107. B. M. Henry, A. G. Erlat, A. McGuigan, C. R. M. Grovenor, G. A. D. Briggs, Y. Tsukahara, T. Miyamoto, N. Noguchi and T. Niijima, Thin Solid Films **382** (1-2), 194 (2001).

108. P. Mandlik, J. Gartside, L. Han, I. C. Cheng, S. Wagner, J. A. Silvernail, R. Q. Ma, M. Hack and J. J. Brown, Applied Physics Letters **92** (10), 103309 (2008).

109. P. F. Carcia, R. S. McLean, M. H. Reilly, M. D. Groner and S. M. George, Applied Physics Letters **89** (3), 31915 (2006).

110. D. A. Muller, N. Nakagawa, A. Ohtomo, J. L. Grazul and H. Y. Hwang, Nature **430** (7000), 657 (2004).

111. S. Kwak, J. Jun and E. S. Jung, Langmuir **25** (14), 8051 (2009).

112. B. W. Hussey and A. Gupta, Journal Of Applied Physics **72** (1), 287 (1992).

113. T. Kawakubo, S. Komatsu, K. Abe, K. Sano, N. Yanase and N. Fukushima, Japanese Journal Of Applied Physics Part 1-Regular Papers Short Notes & Review Papers **37** (9B), 5108 (1998).

114. F. Pailloux, R. Lyonnet, J. L. Maurice and J. P. Contour, Applied Surface Science **177** (4), 263 (2001).

115. A. P. Chen, Z. X. Bi, C. F. Tsai, L. Chen, Q. Su, X. H. Zhang and H. Y. Wang, Crystal Growth & Design **11** (12), 5405 (2011).

116. I. Markov and R. Kaischew, Thin Solid Films **32** (1), 163 (1976).

117. H. A. Jehn, Advanced Techniques for Surface Engineering **1**, 5 (1992).

118. M. Paranjape, A. K. Raychaudhuri, N. D. Mathur and M. G. Blamire, Phys. Rev. B. **67** (21), 214415 (2003).

119. J. Z. Sun, D. W. Abraham, R. A. Rao and C. B. Eom, Appl. Phys. Lett. **74** (20), 3017 (1999).

120. M. Ziese, H. C. Semmelhack and K. H. Han, Phys. Rev. B. **68** (13), 134444 (2003).

121. D. Liu, N. Wang, G. Wang, Z. Shao, X. Zhu, C. Zhang and H. Cheng, Journal of Alloys and Compounds **580**, 354 (2013).

122. D. Liu, N. Wang, G. Wang, Z. Shao, X. Zhu, C. Zhang and H. Cheng, Applied Physics Letters **102** (13), 134105 (2013).

123. D. Liu, H. Cheng, X. Zhu, G. Wang and N. Wang, ACS Appl Mater Interfaces **5** (21), 11258 (2013).

124. Y. F. Lu, J. Klein, C. Hofener, B. Wiedenhorst, J. B. Philipp, F. Herbstritt, A. Marx, L. Alff and R. Gross, Phys. Rev. B. **62** (23), 15806 (2000).

125. J. L. Maurice, F. Pailloux, A. Barthelemy, O. Durand, D. Imhoff, R. Lyonnet, A. Rocher and J. P. Contour, Philos. Mag. **83** (28), 3201 (2003).

126. L. Ranno, A. Llobet, R. Tiron and E. Favre-Nicolin, Appl. Surf. Sci. **188** (1-2), 170 (2002).

127. A. Malachias, S. Kycia, G. Medeiros-Ribeiro, R. Magalhaes-Paniago, T. I. Kamins and R. S. Williams, Phys. Rev. Lett. **91** (17), 176101 (2003).

128. L. Wang and J. Gao, J. Appl. Phys. **105** (7), 07E514 (2009).

129. A. N. Chaika, A. M. Ionov, N. A. Tulina, D. A. Shulyatev and Y. M. Mukovskii, J. Electron. Spectrosc. Relat. Phenom. **148** (2), 101 (2005).

130. J. W. Liu, G. Chen, Z. H. Li, W. W. An and Z. G. Zhang, J. Alloys Compd. **431** (1-2), 1 (2007).

131. J. J. Liang and H. S. Weng, Ind. Eng. Chem. Res. **32** (11), 2563 (1993).

132. Q. H. Wu, M. L. Liu and W. Jaegermann, Mater. Lett. **59** (16), 1980 (2005).

133. E. Beyreuther, S. Grafstrom, L. M. Eng, C. Thiele and K. Dorr, Phys. Rev. B. **73** (15), 155425 (2006).

134. J. W. Murray, J. G. Dillard, R. Giovanoli, H. Moers and W. Stumm, Geochim. Cosmochim. Acta **49** (2), 463 (1985).

135. Y. Uwamino, T. Ishizuka and H. Yamatera, J. Electron. Spectrosc. Relat. Phenom. **34** (1), 67 (1984).

136. K. Tabata, I. Matsumoto and S. Kohiki, J. Mater. Sci. **22** (5), 1882 (1987).

137. N. Gunasekaran, N. Bakshi, C. B. Alcock and J. J. Carberry, Solid State Ionics **83** (1-2), 145 (1996).

138. D. A. Pawlak, M. Ito, M. Oku, K. Shimamura and T. Fukuda, Journal of Physical Chemistry B **106** (2), 504 (2002).

139. A. A. Adjaottor, E. Ma and E. I. Meletis, Surf. Coat. Technol. **89** (3), 197 (1997).

140. E. I. Meletis, Surf. Coat. Technol. **149** (2-3), 95 (2002).

141. Y. Fang, V. R. Sakhalkar, J. He, H. Q. Jiang, J. C. Jiang and E. I. Meletis, JNanoR. **14**, 83 (2011).

142. C. Adamo, X. Ke, H. Q. Wang, H. L. Xin, T. Heeg, M. E. Hawley, W. Zander, J. Schubert, P. Schiffer, D. A. Muller, L. Maritato and D. G. Schlom, Applied Physics Letters **95** (11), 112504 (2009).

143. T. W. Darling, A. Migliori, E. G. Moshopoulou, S. A. Trugman, J. J. Neumeier, J. L. Sarrao, A. R. Bishop and J. D. Thompson, Physical Review B **57** (9), 5093 (1998).

144. A. Ohtomo, D. A. Muller, J. L. Grazul and H. Y. Hwang, Nature **419** (6905), 378 (2002).

145. K. S. Takahashi, M. Kawasaki and Y. Tokura, Applied Physics Letters **79** (9), 1324 (2001).

146. M. B. Salamon and M. Jaime, Reviews Of Modern Physics **73** (3), 583 (2001).

147. C. W. Lin, S. Okamoto and A. J. Millis, Physical Review B **73** (4), 41104 (2006).

148. P. A. Salvador, A. M. Haghiri-Gosnet, B. Mercey, M. Hervieu and B. Raveau, Applied Physics Letters **75** (17), 2638 (1999).

149. T. Koida, M. Lippmaa, T. Fukumura, K. Itaka, Y. Matsumoto, M. Kawasaki and H. Koinuma, Physical Review B **66** (14), 144418 (2002).

150. J. Verbeeck, O. I. Lebedev, G. Van Tendeloo and B. Mercey, Physical Review B **66** (18), 184426 (2002).

151. T. Satoh, K. Miyano, Y. Ogimoto, H. Tamaru and S. Ishihara, Physical Review B **72** (22), 224403 (2005).

152. S. Smadici, P. Abbamonte, A. Bhattacharya, X. F. Zhai, B. Jiang, A. Rusydi, J. N. Eckstein, S. D. Bader and J. M. Zuo, Physical Review Letters **99** (19), 196404 (2007).

Biographical Information

Yishu Wang was in Liaoning, China. He received his bachelor degree in Materials Science and Engineering from Dalian University of Technology in 2007. After that, he continued his master degree in Materials Science and Engineering in University of Science & Technology in Beijing until 2010. In 2015, he received his Ph. D degree in Materials Science and Engineering from University of Texas at Arlington. During his graduated study in University of Science & Technology in Beijing, he focused on the preparation of one dimensional ZnO nanowire by using chemical vapor deposition method and investigation of its piezoelectric property. During his study in University of Texas at Arlington, his studies focused on fabrication of compositional gradient epitaxial strontium doped lanthanum manganite thin film by using co-sputtering deposition method and characterization by using x-ray diffraction (XRD), atomic force microscopy (AFM), x-ray photoelectron spectroscopy (XPS) and high resolution transmission electron microscopy (HRTEM). Three journal papers and one conference paper have been published from his work during his graduate study. He also got Graduate Student Seminar Award twice.